University of Nebraska - Lincoln

DigitalCommons@University of Nebraska - Lincoln

Department of Electrical and Computer Engineering: Dissertations, Theses, and Student Research

Electrical & Computer Engineering, Department of

Fall 12-2023

Amorphous Boron Carbide-Amorphous Silicon Heterojunction Devices

Vojislav Medic
University of Nebraska-Lincoln, vmedic2@unl.edu

Follow this and additional works at: https://digitalcommons.unl.edu/elecengtheses

Part of the Computer Engineering Commons, Electronic Devices and Semiconductor Manufacturing Commons, Nanotechnology Fabrication Commons, and the Other Electrical and Computer Engineering Commons

Medic, Vojislav, "Amorphous Boron Carbide-Amorphous Silicon Heterojunction Devices" (2023). *Department of Electrical and Computer Engineering: Dissertations, Theses, and Student Research*. 145.
https://digitalcommons.unl.edu/elecengtheses/145

This Article is brought to you for free and open access by the Electrical & Computer Engineering, Department of at DigitalCommons@University of Nebraska - Lincoln. It has been accepted for inclusion in Department of Electrical and Computer Engineering: Dissertations, Theses, and Student Research by an authorized administrator of DigitalCommons@University of Nebraska - Lincoln.

AMORPHOUS BORON CARBIDE-AMORPHOUS SILICON HETEROJUNCTION DEVICES

by

Vojislav Medic

A DISSERTATION

Presented to the Faculty of

The Graduate College at the University of Nebraska

In Partial Fulfillment of Requirements

For the Degree of Doctor of Philosophy

Major: Electrical Engineering

Under the Supervision of Professor Natale Ianno

Lincoln, Nebraska

December 2023

AMORPHOUS BORON CARBIDE-AMORPHOUS SILICON HETEROJUNCTION DEVICES

Vojislav Medic, Ph.D.

University of Nebraska, 2023

Advisor: Natale Ianno

This dissertation will show successful development and characterization of amorphous boron carbide-amorphous silicon heterojunction device with potential for neutron detection.

The amorphous hydrogenated boron carbide (a-BC:H) has been extensively researched as a semiconductor for neutron voltaic device fabrication. Naturally occurring boron contains 19.8% of boron isotope B^{10} that has a high absorption cross section of thermal neutrons at lower energies, and boron carbide contains 14.7% of that B^{10} isotope. Therefore, as a semiconductor compound of boron a-BC:H has the ability to absorb radiation, generate charge carriers, and collect those carriers.

Previous work on a-BC:H devices investigated the fabrication of homojunction, heterojunction and heteroisomeric devices from the polymeric precursors ortho-carborane (p-type) and meta-carborane (n-type) using plasma enhanced chemical vapor deposition (PECVD). However, the metal contact formation with a-BC:H has not been previously studied with respect to its possible effects on device performance. The metal/a-BC:H contact investigation was performed, producing contact resistance for an Ohmic contact formation of Ti on n-type a-BC:H. The resistivity of the n-type a-BC:H in the direction of the device current flow was also investigated. However, a metal that forms an Ohmic contact the p-type a-BC:H has not been identified.

The p-type a-BC:H made from ortho-carborane has high resistivity and doping limitations, so p-type single crystal silicon with n-type a-BC:H grown from meta-carborane has been previously studied and shown to produce the most optimal device performance compared to different a-BC:H device structures. As single crystal silicon has well known electrical and material properties, with X-Ray Photoelectron Spectroscopy (XPS) and Spectroscopic Ellipsometry measurements, electronic properties at the heterojunction interface of a-BC:H/c-Si is obtained by calculating valence band offset.

However, as single crystal silicon degrades over time due to radiation induced damage to its crystalline structure, p^+-type hydrogenated amorphous silicon (a-Si:H) is investigated as a potential layer in the formation of the a-BC:H heterojunction device. From the characterization of a-BC:H/c-Si and a-BC:H/a-Si:H devices, the a-BC:H/a-Si:H device shows potential in fabricating a novel neutron voltaic device.

Acknowledgements

I would like to express my immense gratitude and appreciation for Dr Natale Ianno without whom I would not be in this position. His guidance, insight, and enthusiasm for research (and life) throughout the years have made my time in graduate school the best years of my life.

I would like to thank my committee, Dr Craig Zuhlke, Dr Christos Argyropoulos, Dr Jeffrey Shield that have provided valuable guidance and exceptional coursework over the years.

Thank you to my colleagues, Dr Matthew Hilfiker, Dr Ufuk Kilic, Graham Kauffman, Mirzojamshed Mirzokarimov and Aaron Ediger for your collaborations, conversations, insights, and friendship.

I would like to thank the Office of Naval Research for partially supporting this work, National Renewable Energy Laboratory for providing the hydrogenated amorphous silicon substrates, as well as the Department of Electrical and Computer Engineering at University of Nebraska-Lincoln. This material is based upon research supported by, or in part by, the Office of Naval Research under Award Number N00014-20-1-2025.

Acronyms/Abbreviations

BC	Boron carbide
a-BC:H	Hydrogenated amorphous boron carbide
ocarb	Ortho-carborane
mcarb	Meta-carborane
OC	Ortho-carborane
MC	Meta-carborane
a-Si	Amorphous silicon
a-Si:H	Hydrogenated amorphous silicon
c-Si	Crystalline silicon
HF	Hydrofluoric acid
CVD	Chemical vapor deposition
PECVD	Plasma enhanced chemical vapor deposition
DC	Direct current
AC	Alternating current
HOMO	Highest occupied molecular orbital
LUMO	Lowest unoccupied molecular orbital
R_s	Semiconductor resistance
R	Resistance
R_c	Contact resistance
ρ	Resistivity
b	Film thickness
a	Radius of metal contact
XPS	X-ray photoelectron spectroscopy
eV	electron volt – unit of energy

K	Boltzmann's constant
E_c	Conduction energy level
E_i	Intrinsic energy level
E_v	Valence energy level
E_f	Fermi energy level
E_0	Vacuum energy level
ε_s	Dielectric permittivity
ϕ_M	Work function of a metal
ϕ_S	Work function of a semiconductor
χ	Electron affinity
ΔE_c	Difference in conduction band energy (heterojunctions)
ΔE_v	Difference in valence band energy (heterojunctions)

Table of Contents

Chapter 1 - Introduction 1

1.1 Neutron interactions with matter and energy ranges 4

1.2 Neutron absorber materials 7

1.3 Boron as a neutron absorber 8

1.4 Boron carbide for neutron detection 10

1.5 References 13

Chapter 2 - Background and Experimental Procedures 22

2.1 Boron Carbide Thin-Film Growth 22

2.1.1 Molecular precursors 22

2.1.2 Plasma enhanced chemical vapor deposition (PECVD) 25

2.1.3 Boron carbide thin-film growth via PECVD 34

2.2 Metallization via physical vapor deposition (PVD) 43

2.3 Boron carbide devices and fabrication 46

2.3.1 Thin-film coated devices and solid-form (bulk) devices 47

2.3.2 Boron carbide homojunction devices and doping 51

2.3.3 Boron carbide heterojunction devices 55

2.3.4 Single crystal Si/a-BC:H device fabrication 59

2.3.5 Heteroisomeric a-BC:H/a-BC:H device 62

2.3.6 Amorphous hydrogenated Si/a-BC:H device and fabrication 64

2.4 Metal/a-BC:H contact resistance 66

2.4.1 Ohmic and Schottky contacts 67

2.4.2 Contact resistance measurement – transfer length method 70

2.4.3 Contact resistance measurement – spreading resistance model 73

2.4.4 Fabrication of metal/a-BC:H spreading resistance structures 77

2.5 Device characterization 79

2.5.1 V-I characterization 79

2.5.2 X-Ray Photoelectron Spectroscopy (XPS) 82

2.5.3 Spectroscopic Ellipsometry 88

2.6 Summary 91

2.7 References 92

Chapter 3 – Investigation of Metal/a-BC:H Contacts 102

3.1 Titanium as the metal contact 108

3.2 Chromium as the metal contact 112

3.3 Summary of metal contacts 120

3.4 References 125

Chapter 4 – Investigation of Boron Carbide (a-BC:H) Devices 129

4.1 Single crystal silicon-boron carbide device 132

4.2 Amorphous silicon-boron carbide device 141

4.3 Discussion of the a-BC:H/a-Si:H (c-Si) band diagrams 151

4.4 Summary 155

4.5 References 157

Chapter 5 – Summary and Conclusion 160

List of Figures:

Figure 1 Structure of boron carbide icosahedra unit 11

Figure 2 Ortho-carborane (left) and meta-carboran (right) icosahedra units 22

Figure 3 ortho-carborane (left) ad meta-carborane (right) with bonded hydrogen 22

Figure 4 Calculated ground state molecular orbitals and their level ordering for ortho-carborane (left) and meta-carborane (right) 23

Figure 5 Capacitive coupled (left) and inductive coupled (right) plasma 25

Figure 6 High vacuum deposition system 26

Figure 7 High vacuum system schematic 27

Figure 8 Plasma for grounded substrate (left) and driven substrate (right) 27

Figure 9 Grounded substrate plasma system schematic 28

Figure 10 Driven substrate plasma system schematic 29

Figure 11 Driven substrate voltage waveform 30

Figure 12 Leybold 450 series turbomolecular pump 31

Figure 13 Deposited a-BC:H with the grounded substrate (left) and driven substrate (right) 34

Figure 14 a-BC:H evaporation manifold 37

Figure 15 a-BC:H evaporation manifold schematic 38

Figure 16 Delaminated a-BC:H films on a Chromium substrate 39

Figure 17 M2000 J.A. Woollam ellipsometer mounted on the system chamber 40

Figure 18 a-BC:H 140nm film 41

Figure 19 a-BC:H 172nm film 41

Figure 20 a-BC:H 190nm film 41

Figure 21 a-BC:H 348nm film 41

Figure 22 a-BC:H deposition without rotation (left) and with rotation (right) of sample stage 42

Figure 23 DC magnetron sputtering process schematic 43

Figure 24 Titanium (left) and copper (right) dc magnetron sputtered targets with the "racetrack" 44

Figure 25 Simple thin-film-coated neutron detector 47

Figure 26 Reverse biased p-n junction band diagram 48

Figure 27 Simple bulk semiconductor neutron detector diode 49

Figure 28 Homojunction band diagram in equilibrium 51

Figure 29 p-n junction depletion region 51

Figure 30 a-BC:H doped film structure with dopants (black circles) bonded throughout the film 52

Figure 31 Possible molecular schematic of a-BC:H icosahedra and dopant bonding B (green), C (grey), H (white), dopant (red) 52

Figure 32 Structure and V-I characteristic of a-BC:H homojunction device via Co doping 53

Figure 33 Structure and V-I characteristic of a-BC:H homojunction device via Ni doping 53

Figure 34 Types of heterojunction band structures: type I (top), type II (middle), type III (bottom) 55

Figure 35 Boron/ a-BC:H heterojunction device V-I characteristics 56

Figure 36 V-I characteristic of a-BC:H heterojunction device made from 1,2-$PCB_{10}H_{11}$ and ortho-carborane precursors 57

Figure 37 V-I characteristics of a-BC:H (p)/SiC(n) heterojunction device with Au metal contacts at varying temperatures 57

Figure 38 Al-Si(p)-Al V-I characteristic (Al on rough then shinny side deposition post-HF acid process 60

Figure 39 V-I characteristic of Al contact on smooth side (left) and rough side (right) of single crystal Si(p) post-HF acid processing 60

Figure 40 Procedure for single crystal Si/a-BC:H device fabrication 61

Figure 41 V-I characteristic of a-BC:H heteroisomeric device 63

Figure 42 Crystaline silicon (a), amorphous silicon (b), hydrogenated amorphous silicon (c) 65

Figure 43 a-Si:H/ a-BC:H heterojunction device fabrication procedure 65

Figure 44 Schottky vs Ohmic contact V-I characteristics 67

Figure 45 Energy band diagrams for metal-semiconductor contact an instant after the contact is formed (a) and (b) and under equilibrium conditions (c) and (d) 69

Figure 46 Metal contact bars with varying separation length on a semiconductor 70

Figure 47 Total resistance (R) as a function of separation length (L) 71

Figure 48 Metal-semiconductor contact structure for spreading resistance model, top view (left), cross section view (right) 73

Figure 49 Metal-semiconductor structure for spreading resistance model 74

Figure 50 Total resistance as a function of semiconductor film thickness 74

Figure 51 Procedure for metal/a-BC:H/metal structure fabrication 77

Figure 52 Top view of the metal/a-BC:H/metal structure 78

Figure 53 Keithley 2400 series source meter.. 79

Figure 54 4-Wire connections on the Keithley 2400 source meter 79

Figure 55 Internal circuitry schematic of the 4-wire connection 80

Figure 56 4-Wire measreument probe station.. 80

Figure 57 The V-I characteristic of a commercially available silicon diode 81

Figure 58 An XPS system schematic 83

Figure 59 The Thermo-Scientific XPS/UPS system 84

Figure 60 Example XPS survey, and boron, carbon and oxygen scan 85

Figure 61 Example depth profile XPS survey 86

Figure 62 Example XPS valence band scan with depth profile 86

Figure 63 M2000 ellipsometer.. 89

Figure 64 J.A. Woollam RC2 ellipsometer... 89

Figure 65 Reported doping investigation that used three different metal contact combinations in device fabrication 103

Figure 66 Fabricated device without specified contacts 104

Figure 67 c-Si/a-BC:H optical model fit of the RC2 data 106

Figure 68 Optical constants for a-BC:H film... 107

Figure 69 Ti contact spreading resistance structure... 108

Figure 70 V-I characteristics of Ti/a-BC:H/Ti structures with varying thicknesses 109

Figure 71 Total resistance vs a-BC:H thickness for Ti contact spreading resistance structure.. 110

Figure 72 V-I characteristics of Cr/a-BC:H(p)/Cr structure 112

Figure 73 XPS spectra of oxygen, boron, and chromium in the p-type a-BC:H/Cr structure 113

Figure 74 V-I characteristics of Cr/a-BC:H(n)/Cr structure 114

Figure 75 Procedure for metal/thin metal film in-vacuo/BC/metal structure fabrication 115

Figure 76 XPS oxygen spectra comparison of the a-BC:H/thin Cr/Cr structure and the a-BC:H/Cr structure fabricated by previously established procedure 116

Figure 77 XPS oxygen spectra comparison of the a-BC:H/thin Cr/Cr structure and the a-BC:H/Cr structure fabricated in-situ 117

Figure 78 V-I characteristics of Cr/thin Cr/a-BC:H(n)/Cr structure 118

Figure 79 V-I characteristics of Ni/a-BC:H(p)/Ni structure 121

Figure 80 V-I characteristics of Ni/a-BC:H(n)/Ni structure 121

Figure 81 V-I characteristics of Cr/a-BC:H(p)/Ni structure 122

Figure 82 V-I characteristics of Al/a-BC:H(n)/Al structure 122

Figure 83 V-I characteristics of Cu/a-BC:H(n)/Al structure 123

Figure 84 V-I characteristics of Al/a-BC:H(p)/Al structure 123

Figure 85 V-I characteristics of Hf/a-BC:H(p)/Hf structure 124

Figure 86 The a-BC:H Tauc plot for obtaining the bandgap 130

Figure 87 V-I characteristics of n-type single crystal Si and p-type BC heterojunction device 132

Figure 88 V-I characteristics of a 500nm n-type a-BC:H on single crystal silicon device 133

Figure 89 V-I characteristics of a 350nm n-type a-BC:H on single crystal silicon device 133

Figure 90 Comparison between two c-Si/a-BC:H devices with different a-BC:H thicknesses 134

Figure 91 XPS spectra of Si in the bulk and at the interface with a-BC:H........ 135

Figure 92 XPS spectra of B (a-BC:H) in the bulk and at the interface with c-Si 136

Figure 93 Valence band maximum of a-BC:H from XPS spectra from the bulk 137

Figure 94 Valence band maximum of c-Si from XPS spectra from the bulk 137

Figure 95 The a-BC:H(n)/c-Si(p) heterojunction band diagram at the interface 139

Figure 96 The a-BC:H(n)/c-Si(p) heterojunction band diagram........ 139

Figure 97 V-I characteristic of a-Si:H(p)/a-BC:H(n) device 141

Figure 98 V-I characteristic of a-Si:H(p)/a-BC:H(n) device with HF pre-deposition process........ 142

Figure 99 V-I characteristics of a-Si:H/a-BC:H devices with HF processed a-Si:H layer and unprocessed a-Si:H layer on the same scale (left) and unprocessed device on a secondary vertical axis (right)........ 143

Figure 100 V-I characterstics of a-Si;H(p)/a-BC:H(n) (left vertical axis) and c-Si(p)/a-BC:H(n) (right vertical axis) devices 144

Figure 101 XPS oxygen spectra comparison of the a-BC:H/a-Si:H device with no HF (left vertical axis) and HF acid pre-deposition processing of a-Si:H (right vertical axis) 145

Figure 102 XPS spectra of B (a-BC:H) in the bulk and at the interface with a-Si:H 147

Figure 103 XPS spectra of Si (a-Si:H) in the bulk and at the interface with a-BC:H 147

Figure 104 Valence band maximum of a-BC:H from XPS spectra from the bulk 148

Figure 105 Valence band maximum of a-Si:H from XPS spectra from the bulk 148

Figure 106 The a-BC:H(n)/a-Si:H(p) heterojunction band diagram at the interface...... 149

Figure 107 The a-BC:H(n)/a-Si:H(p) heterojunction band diagram.............................. 150

Figure 108 Band diagrams of a-BC:H/c-Si (left) and a-BC:H/a-Si:H (right) heterojunctions.. 151

List of Tables:

Table 1 Neutron energy ranges 5

Table 2 Neutron absorber isotopes and thermal cross sections 7

Table 3 Boron carbide deposition parameters 36

Table 4 DC sputtering deposition parameters 45

Table 5 Electrical nature of metal-semiconductor contacts 69

Table 6 XPS survey parameters 84

Table 7 Metal contacts on a-BC:H reported in literature 102

Table 8 Work functions of various metals 105

Table 9 Total resistance vs thickness, for Ti spreading resistance structures 109

Table 10 Resistivity of n-type a-BC:H from each set of spreading resistance structures111

Table 11 Various metal contact formation with a-BC:H(n,p) 120

Table 12 Core level peaks and valence band maxima for a-BC:H and c-Si 136

Table 13 Core level peaks and valence band maxima for a-BC:H and a-Si:H 149

List of Equations:

Equation 1: $Ag107 + n \rightarrow\ Ag108\ \rightarrow\ Cd108 + e-$ 9

Equation 2: $Ag109 + n \rightarrow\ Ag110\ \rightarrow\ Cd110 + e-$ 9

Equation 3: $In115 + n \rightarrow\ In116\ \rightarrow\ Sn116 + e-$ 9

Equation 4: $Cd113 + n \rightarrow\ Cd114$ 9

Equation 5: $B10 + n \rightarrow Li7(0.84MeV) + He4(1.47MeV) + \gamma(0.4MeV)$ 9

Equation 6: $\phi s = \chi + EC - EF$ 68

Equation 7: $RT = Rsemi + 2RcA = \rho SLtW + 2RcA$ 71

Equation 8: $\rho S = tWRT - 2RcAL$ 71

Equation 9: $RT = 106\Omega cm \times 1 \times 10 - 4cm3 \times 10 - 5cm \times 2cm + 2RcA =$

$\mathbf{1.67} \times \mathbf{106}\Omega + 2RcA$ 72

Equation 10: $RS = \rho Sb\pi a2$ 73

Equation 11: $RT = RS + 2RcA = \rho Sb\pi a2 + 2RcA$ 74

Equation 12: $\rho S = \pi a2RT - 2RcAb$ 75

Equation 13: $RT = 106\Omega cm \times 300 \times 10 - 7cm\pi \times (0.1cm)2 + 2RcA = \mathbf{955.41}\ \Omega +$

$2RcA$ 76

Equation 14: $Ee = \hbar\omega - EB$ 82

Equation 15: $RT = RS + 2RcA = \rho Sb\pi a2 + 2RcA$ 110

Equation 16: $Rc = 18.913\Omega \cdot \pi(0.1cm)22 = 0.297\Omega cm2$ 110

Equation 17: $\rho s = RT - 2RcA \cdot \pi a2b$ 111

Equation 18: $VBO = \Delta Ev = (CL - VBM)Si - CL - VBMBC + CLBC - CLSiint$ 129

Equation 19: $y = hv\alpha = hv4\pi k\lambda$ 130

Equation 20: $VBO = \Delta Ev = (CL - VBM)Si - CL - VBMBC + CLBC - CLSiint$ 135

Equation 21: $VBO = \Delta Ev = 98.98 - 187.65 + 89 = 0.33eV$ 138

Equation 22 $ECi = CL - VBM + EG - CLint$ 138

Equation 23 $EVi = CLint - (CL - VBM)$ 138

Equation 24: $EF - EV = kT \cdot lnNVp = 0.026eV \cdot ln1.04 \cdot 10191.5 \cdot 1015 = 0.2299eV$ 140

Equation 25: $VBO = \Delta Ev = 98.9 - 187.35 + 89.2 = 0.55eV$ 149

Equation 26: $EF - EV = kT \cdot lnNVp = 0.026eV \cdot ln2 \cdot 10201 \cdot 1019 = 0.078eV$ ... 150

Equation 27: $\Delta Ec = q\chi Si - q\chi BC$ 152

Chapter 1 - Introduction

Neutron detection is an increasingly important research topic due to its applications in nuclear physics, reactor instrumentation, radiation safety, chemical, medical and materials analysis research [1] as well as applications in space exploration [2].

Previous research has been performed developing various types of neutron detectors. Plastic, liquid, and glass scintillators are used for fast-neutron detection due to their response and low cost [3-5]. Proportional counters filled with BF_3 and He^3 work on the principle of measuring incident energy of radiation by producing an output proportional to the energy of radiation absorbed by the detector. As the nuclear reaction that takes place in these gases is exothermic and releases energetic particles into the gas, the ionization produced by these particles initiates the multiplication process that leads to detection [3,6]. Similarly, fission chambers are a variation of the proportional counters as they detect neutron radiation in fissionable materials coated on the inner walls of the chamber [3,7], such as boron (B^{10}) lined fission chambers that can detect neutron radiation based on the reaction of boron with thermal neutrons [3,8,9]. As gas counters and fission chambers become more cumbersome to produce with reduction and shortage of resources, primarily helium [10], and operation of these detectors being encumbered by high voltage operation (~1000V), large device footprint, high pressure, sensitivity to microphonics [11], semiconductors could provide the cornerstone of the next generation neutron detectors.

There are two main types of semiconductor neutron detectors: electronic devices coated with neutron reactive material (e.g., common pn-junction or Schottky devices coated with

B^{10}, LiF^{6} or Gd [12,13]), and detectors made from semiconductors composed of neutron reactive materials such as: silicon carbide, cadmium zinc telluride, boron carbide, or the combination of lithium indium phosphorus and selenium [11, 14-17] that have been reported as the next generation materials in semiconductor neutron detectors. The main difference between the two types of neutron detectors is the internal process of "detecting" incident radiation.

The thin film coating absorbs neutrons and emits reaction products with specific energies. Those products can then reach the semiconductor device surface and produce electron-hole pairs i.e., induced current charge carriers that correspond to a voltage output of the device [18]. As neutrons may interact anywhere within the reactive film and reaction products lose energy as they move throughout the reactive film coating, some of the energy transferred to the semiconductor device surface will be inherently lost. This limits the thickness of the reactive film coating (thicker the coating, larger the area of the reaction products to interact with), which in turn limits the neutron absorption area [19] and decreases detector efficiency.

However, neutron detectors made from semiconductors composed from neutron reactive materials can absorb neutrons and generate the same reaction products as coated device detectors, but also have the ability to generate electron-hole pairs within the same material. This eliminates the losses within the coating materials as was the case with coated neutron detectors and provides the potential for higher efficiency detectors. Additionally, this provides the option of developing and structuring semiconductor detectors. Because of the semiconductor detector's ability to both absorb neutron radiation and generate charge carriers, as well as the material resource availability, there

are possibilities of developing cost-effective, high efficiency, scalable in size, passive or active neutron detectors [11,12, 20].

The main difference between passive and active detectors is the ability to process information in real time. In long range monitoring efforts such as neutron radiation monitoring of the spacecraft LEO in 2001 [21] or low radiation monitoring of research equipment operation [22], processing information after a certain period of time is acceptable. However, when discussing day to day operation of nuclear reactors, unknown exposure to various forms of radiation in low-Earth orbit or deep space, as well as combat zones, active detectors with capabilities of processing information in real time are necessary. Various semiconductor materials have been used for development of thermal neutron detectors like CdZnTe and SiC [14,15, 23, 24], but due to the limited availability and higher cost of materials [25-27], developing detectors using these materials is expensive.

However, semiconducting hydrogenated amorphous boron carbide (a-BC:H) has been widely researched as a low-cost alternative to these materials in the development of neutron detectors. Naturally occurring boron contains 19.8% of boron isotope B^{10} that has a high absorption cross section of thermal neutrons at lower energies, and boron carbide contains 14.7% of that B^{10} isotope. Additionally, due to its amorphous structure and the presence of hydrogen, a-BC:H has high resistance to radiation damage with immense potential for developing low-cost thermal neutron detectors with high absorption of thermal neutron radiation [27-31]. The following sections will discuss in detail neutron interaction with matter, how materials absorb neutrons and why a-BC:H is an attractive material for development of neutron detector devices.

1.1 Neutron interactions with matter and energy ranges

When interacting with matter, neutrons differ from electrons, protons, and ions, as they only interact with atomic nuclei. Because they are neutral, unlike other particles that interact primarily with atomic electrons, neutrons do not interact with electrons (or nuclei) electromagnetically [32]. In vacuum without any interactions half-life of neutrons is $\tau_{1/2}$ = 613.9s, however in air or solids it can be milliseconds as neutrons can be absorbed by various nuclei. There are numerous interactions of neutrons with other nuclei depending on the neutron energy.

In elastic scattering, the neutron bounces off the nucleus elastically and the nucleus recoils without getting internally excited to a different state, carrying off some energy in the process and reducing the neutron energy. Inelastic scattering occurs when the nuclei have internal excited states from few eV to MeV, so when incident neutrons with energies in the keV range interact with those nuclei, the probability of excitation of the nuclei to a different state increases. As the inelastic interaction occurs, neutrons put the nuclei in an excited state [32].

The third common process, the one that is of most interest when discussing neutron absorber materials and neutron absorption, is the process of capturing neutrons by the nucleus into an excited state of the compound nucleus. In turn, that excited state decays by emitting gamma radiation in less than nanoseconds, which is commonly called radiative capture [32]. The absorption cross section defines the probability of the neutron being absorbed by the nucleus, measured in barns (metric unit of area equal to 10^{-28} m^2) and is most noted as σ_γ because of the capture with only gamma energy in the final state [32,33].

Neutron energy is commonly defined based on the neutron reactions and its consequences in that energy range, more than the characteristics of the energy range itself. Table 1 shows the common naming standard of the neutron energy ranges.

Table 1 Neutron energy ranges

Energy Range	Name
0-0.025 eV	Cold
0.025 eV	Thermal
0.025-0.4 eV	Epithermal
0.4-0.6 eV	Cadmium
0.4-1.0 eV	Epicadmium
1-10 eV	Slow
10-300 eV	Resonance
300 eV-1 MeV	Intermediate
1-20 MeV	Fast
>20 MeV	Relativistic

Neutrons at thermal equilibrium with their environment have a Maxwell-Boltzmann distribution of energy with mean energy kT. At room temperature that energy is 0.025eV, and so neutrons at this energy are called thermal neutrons. Cold neutrons have energies lower than thermal neutrons, while epithermal are more energetic than thermal. However, energies from 0.4eV-0.6eV are defined by neutron capture reaction in cadmium isotope Cd^{113}. Because cadmium has a large cross section below 0.5eV with a sharp decrease as energies increase, 0.5eV is referred to as the “cadmium cutoff”. Cadmium is chosen here for nomenclature as it is a commonly used as a selective absorber because of its large absorption cross section at low energies that peaks at 55000 barn at 0.17eV, but at 0.5eV is at 1150 barn which is between B^{10} and He^3. Additionally,

because of its sharp drop off and absence of resonance (until 18eV), cadmium is very useful in separating low energies neutrons below 0.5eV and higher energy neutrons [32]. In addition to cadmium, B^{10} isotope of boron, He^{3}, Gd^{157} are also considered good absorbers that can be utilized in neutron detection of low energy neutrons.

1.2 Neutron absorber materials

Neutron absorber materials are very important as a safety measure in potentially fatal or hazardous neutron rich environments. If enough neutrons escape a nuclear reactor, they can be hazardous (or fatal) to humans or destructive to electronic equipment [32,34,35]. However, due to the interactions with surrounding material, neutrons are most often scattered enough to have an energy spectrum of a moderated neutron gas, i.e., the low energy range [32]. In case that neutrons have not been moderated to low energies by the surrounding materials, they can be passed through polyethylene, water, or moist concrete which are all low-Z materials effective in moderating neutron radiation [32].

To further remove neutrons, they can be passed through good neutron absorber materials that have a high absorption cross section at low energies. Table 2 shows some of the favored neutron absorbers used to remove low-energy neutrons due to their large thermal cross section.

Table 2 Neutron absorber isotopes and thermal cross sections

Target Isotope	Target isotope abundance (%)	Thermal cross section (barn)
Gd^{157}	15.7	254000
Cd^{113}	12.22	20600
He^{3}	1.38E-4	5333
B^{10}	19.9	3838
Li^{6}	7.5	941

The potential of boron for high quality detectors stems from its naturally occurring isotope B^{10}. It is one of the few elements along with He^{3} and Li^{6} that is employed in development of neutron detectors because one or more charged particles are the output of the neutron capture reaction. Those charged particles are relatively easy to detect with common means [32,34].

1.3 Boron as a neutron absorber

Even though cadmium and gadolinium isotopes have larger absorption cross section at lower energies than B^{10} (Table 2), and both Gd^{157} and B^{10} produce charged particles in their final state, there is higher potential for B^{10} in developing low-cost neutron detectors [32].

Primarily, boron is abundant and relatively inexpensive as a material, as it is occurring in approximately 19.9% of natural boron [32,34,35]. There is a 10% difference in mass between the B^{10} isotope and natural boron, making it relatively easy to separate the two, which is why there are tons of B^{10} produced annually for use in the nuclear industry [32,34].

As B^{10} has high absorption cross section (~3840 barns) at lower neutron energy range (~0.025eV) [32,34,35], the neutron absorption of natural boron is sufficiently high at approximately 760 barns at lower energies, as 19.9% of B^{10} is responsible for neutron absorption of natural boron [32,34,35]. As previously discussed, cadmium and materials like silver and indium have an abrupt decrease in absorption cross section as neutron energy increases [32,34-36]. However, in boron, absorption cross section decreases monotonically with increasing neutron energies, but remains sufficiently high at 1 barn for 1MeV neutrons [34,35]. Additionally, absolute values of the absorption cross section throughout the entire energy spectrum are of sufficient magnitudes to make boron an effective neutron absorber in both the intermediate and fast energy range (Table 1) [32,34,35].

When a neutron absorber material proceeds through a neutron capture process, a reaction occurs. Silver produces cadmium isotopes; indium produces tin isotopes and cadmium its own isotopes (Equation 1-4) [37].

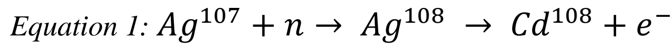
Equation 1: $Ag^{107} + n \rightarrow Ag^{108} \rightarrow Cd^{108} + e^{-}$

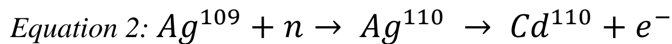
Equation 2: $Ag^{109} + n \rightarrow Ag^{110} \rightarrow Cd^{110} + e^{-}$

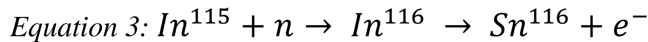
Equation 3: $In^{115} + n \rightarrow In^{116} \rightarrow Sn^{116} + e^{-}$

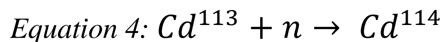
Equation 4: $Cd^{113} + n \rightarrow Cd^{114}$

These reactions can be unstable and their products radioactive, however boron has the advantage of producing stable non-radioactive isotopes of helium and lithium as its reaction products (Equation 5) [32,34].

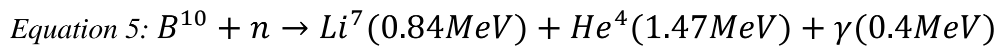
Equation 5: $B^{10} + n \rightarrow Li^{7}(0.84MeV) + He^{4}(1.47MeV) + \gamma(0.4MeV)$

The combination of large cross section required for effective neutron capture, stable reaction products that eliminate emission of nuclear radiation, thermal conductivity that prevent reaching excessive temperatures as well as high melting point [34,36,37], give boron and its compounds high potential for various application. Boric acid is used as a chemical shim that produces a spatially uniform neutron absorption when dissolved in the water coolant. It is used in the moderator/coolant of research reactors as well as being mixed with concrete in the construction of reactor buildings. Boral (BC in aluminum matrix), bocasil (BC in silicon rubber), and polyboron (boric acid in polyethylene) can be used as neutron shields in reactors, material storage and instrumentation [34]. Natural and B^{10} enriched boron, as well as boron carbide can be used in developing neutron detectors [34].

1.4 Boron carbide for neutron detection

As a compound of boron, boron carbide has a combination of attractive properties: high melting point, extreme abrasive resistance, chemical inertness, thermal stability, and radiation resistance. With that combination of properties boron carbide can be used as a thermal semiconductor in hostile environments with high levels of radiation [34,37-40].

Materials whose prime constituent is boron are called boron-rich solids and of the atoms in boron carbides, boron comprises 81-91 atomic percent. As previously discussed, the abundance of B^{10} isotope in natural boron facilitates neutron absorption in these materials. There is a commercially available B^{10} isotope with over 90% isotropic purity and utilizing boron compounds that are enriched with B^{10} maximizes neutron absorption in boron-rich solids like boron carbide [34,38-40].

There are wide ranges of stable compositions of boron carbides with wide distributions of boron and carbon atoms (~8-20 at. % C). Particularly, BC grown from icosahedral hydrogenated molecular precursors via plasma enhanced chemical vapor deposition (discussed in detail in the following chapter) have been shown to produce amorphous hydrogenated structures of B_5C (a-BC:H) boron carbides. Amorphous hydrogenated boron carbide as a boron-rich solid has a building block of icosahedral structure that is based on the ability of elemental boron to form caged structures in varying sizes [41-43]. The icosahedra of boron carbide are effectively two pentagonal pyramids bonded together on a 12-atom unit where atoms are positioned at the vertices of an icosahedron (Figure 1) [38,41,42].

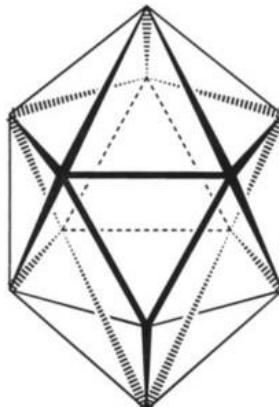

Figure 1 Structure of boron carbide icosahedra unit

Because of unconventional bonding in this material, each cluster is bonded together through metallic bonding. While metallic bonding is electron-deficient internal bonding, each of the atoms also bonds covalently to an atom outside of its cluster to a hydrogen atom [41,44,45]. Additionally, boron clusters have the affinity to often add electrons in their internal states, so in solids this means that these clusters can accept electrons, atoms, or larger structural units as donors [45]. Even though their metallic bonding differentiates these boron clusters from their environment, their covalent bonding is even stronger than their internal bonding resulting in a tough material with high melting temperatures above 2000ºC [33,34,45].

One of the most important features of boron carbides, both crystalline and a-BC:H is their tendency to resist radiation. When a crystalline material is exposed to heavy doses of ionizing radiation, it is expected that a material will exhibit condensation of defects and amorphization that is expected from large densities of point defects [45,46]. Neither amorphization nor amalgamation of defects was found in nitrogen ion bombarded, large lithium-ion bombarded boron carbides, nor boron carbides irradiated with high doses of 1MeV electrons in an electron microscope [45]. Additionally, no expected changes occur

with electron bombardment of boron carbides at low temperatures, suggesting that the self-healing that seemingly occurs with recombination of vacancies is not thermally activated. This means that when fission fragments moving through the lattice knock host atoms from their equilibrium position and create vacancies, those vacancies tend to spontaneously recombine [38,45], resulting in minimized degradation due to radiation damage. As radiation tolerance is not present in borides with conventional bonding, like boron nitride [47], and is not dependent on temperature activation, the self-healing property of boron carbides, i.e., recombination of vacancies created by irradiation, could be attributed to the unusual icosahedral structure of the semiconducting boron carbides [45].

Combining the self-healing property of a-BC:H, strong covalent bonding, amorphous structure, and presence of hydrogen that improves electronic properties in the amorphous structure, development of thin film a-BC:H devices for neutron detection is widely researched. There are disagreements in literature whether all-boron carbide devices can be developed as neutron detectors due to confusion between dielectric and semiconducting BC polytypes [8,17]. However, previous research proposes that all a-BC:H neutron detectors can be developed from semiconducting polytypes of BC [38-40,49-54].

1.5 References

[1] Klett, A. (2012). Neutron Detection. In: Grupen, C., Buvat, I. (eds) Handbook of Particle Detection and Imaging. Springer, Berlin, Heidelberg https://doi.org/10.1007/978-3-642-13271-1_31

[2] S Yamaguchi, A Uritani, H Sakai, C Mori, T Iguchi, H Toyokawa, N Takeda, K Kudo, Spherical neutron detector for space neutron measurement, Nuclear Instruments and Methods in Physics Research Section A: Accelerators, Spectrometers, Detectors and Associated Equipment, Volume 422, Issues 1–3, 1999, Pages 600-605, ISSN 0168-9002, https://doi.org/10.1016/S0168-9002(98)00946-2

[3] T.W. Crane and M.P. Baker. "Neutron Detectors." Micro-Pattern Gaseous Detectors (2020), page 379-406

[4] N. Kawaguchi, T. Yanagida, Y. Yokota, K. Watanabe, K. Kamada, K. Fukunuda, T. Suyama, A. Yoshikawa, Study of crystal growth and scintillation properties as a neutron detector of 2-inch diameter eu doped LiCaAlF6 single crystal, 2009 IEEE Nuclear Science Symposium Conference Record (NSS/MIC), Orlando, FL, USA, 2009, pp. 1493-1495, https://doi.org/10.1109/NSSMIC.2009.5402299.

[5] L.M. Bollinger, G.E. Thomas, R.J. Ginther, Neutron detection with glass scintillators, Nuclear Instruments and Methods, Volume 17, Issue 1, 1962, Pages 97-116, ISSN 0029-554X, https://doi.org/10.1016/0029-554X(62)90178-7

[6] A.Buchtela, Handbook of Radioactivity Analysis (Second Edition), Academic Press, 2003, ISBN 9780124366039, https://doi.org/10.1016/B978-012436603-9/50007-7

[7] Z. Lyric, A review on the modeling of fission chambers, Kansas State University, 2017

[8] P.M. Dighe, D.N. Prasad, K.R. Prasad, S.K. Kataria, S.N. Athavale, A.L. Pappachan, A.K. Grover, Boron-lined proportional counters with improved neutron sensitivity, Nuclear Instruments and Methods in Physics Research Section A: Accelerators, Spectrometers, Detectors and Associated Equipment, Volume 496, Issue 1, 2003, Pages 154-161, ISSN 0168-9002, https://doi.org/10.1016/S0168-9002(02)01635-2

[9] Amaro, F., Monteiro, C., dos Santos, J. *et al.* Novel concept for neutron detection: proportional counter filled with ^{10}B nanoparticle aerosol. *Sci Rep* **7**, 41699 (2017). https://doi.org/10.1038/srep41699

[10] Richard T. Kouzes, James H. Ely, Luke E. Erikson, Warnick J. Kernan, Azaree T. Lintereur, Edward R. Siciliano, Daniel L. Stephens, David C. Stromswold, Renee M. Van Ginhoven, Mitchell L. Woodring, Neutron detection alternatives to ^{3}He for national security applications, Nuclear Instruments and Methods in Physics Research Section A: Accelerators, Spectrometers, Detectors and Associated Equipment, Volume 623, Issue 3, 2010, Pages 1035-1045, ISSN 0168-9002, https://doi.org/10.1016/j.nima.2010.08.021

[11] Nikolic, R J, Cheung, C L, Reinhardt, C E, and Wang, T F, Future of Semiconductor Based Thermal Neutron Detectors, 2006, United States, https://www.osti.gov/servlets/purl/893992

[12] A.N. Caruso, The physics of solid-state neutron detector materials and geometries, J. Phys.: Condens. Matter 22 443201 (2010), https://doi.org/10.1088/0953-8984/22/44/443201

[13] S. L. Bellinger, R. G. Fronk, W. J. McNeil, J. K. Shultis, T. J. Sobering, and D.S. McGregor, Characteristics of the stacked microstructured solid state neutron detector, Proc. SPIE 7805, Hard X-Ray, Gamma-Ray, and Neutron Detector Physics XII, 78050N (20 September 2010); https://doi.org/10.1117/12.863603

[14] D.S. McGregor, J.T. Lindsay, R.W. Olsen, Thermal neutron detection with $cadmium_{1-x}$ $zinc_x$ telluride semiconductor detectors, Nuclear Instruments and Methods in Physics Research A 381 (1996) 498-501

[15] J. Coutinho et al, Silicon carbide diodes for neutron detection, Nuclear Inst. and Methods in Physics Research, A 986 (2021) 164793, https://doi.org/10.1016/j.nima.2020.164793

[16] A. Rose, Sputtered boron films on silicon surface barrier detectors, Nuclear Instruments and Methods, Volume 52, Issue 1, 1967, Pages 166-170, ISSN 0029-554X, https://doi.org/10.1016/0029-554X(67)90576-9

[17] Daniel G. Chica, Yihui He, Kyle M. McCall, Duck Young Chung, Rahmi O. Pak, Giancarlo Trimarchi, Zhifu Liu, Patrick M. De Lurgio, Bruce W. Wessels & Mercouri G. Kanatzidis, Direct thermal neutron detection by the 2D semiconductor $^6LiInP_2Se_6$. *Nature* **577**, 346–349 (2020). https://doi.org/10.1038/s41586-019-1886-8

[18] J. K. Shultis and D. S. McGregor, Efficiencies of coated and perforated semiconductor neutron detectors, IEEE Symposium Conference Record Nuclear

Science 2004., Rome, Italy, 2004, pp. 4569-4574 Vol. 7, https://doi.org/10.1109/NSSMIC.2004.1466900

[19] D. S. McGregor, S. M. Vernon, H. K. Gersch, S. M. Markham, S. J. Wojtczuk and D. K. Wehe, Self-biased boron-10 coated high-purity epitaxial GaAs thermal neutron detectors, in IEEE Transactions on Nuclear Science, vol. 47, no. 4, pp. 1364-1370, Aug. 2000, https://doi.org/10.1109/23.872979

[20] Miller, G. L., W. M. Gidson, and P. F. Donovan, Semiconductor particle detectors, Annual Review of Nuclear Science 12.1 (1962): 189-220

[21] E.R Benton, E.V Benton, A.L Frank, Neutron dosimetry in low-earth orbit using passive detectors, Radiation Measurements, Volume 33, Issue 3, 2001, Pages 255-263, ISSN 1350-4487, https://doi.org/10.1016/S1350-4487(01)00047-6

[22] Landauer, Dosimetry badges, https://www.landauer.com/dosimeter-badges

[23] T. Takahashi and S. Watanabe, Recent progress in CdTe and CdZnTe detectors, in IEEE Transactions on Nuclear Science, vol. 48, no. 4, pp. 950-959, Aug. 2001, https://doi.org/10.1109/23.958705

[24] F. Nava et al, Silicon carbide and its use as a radiation detector material, Meas. Sci. Technol. 19 102001, (2008), https://doi.org/10.1088/0957-0233/19/10/102001

[25] Kromek, About CdZnTe, https://www.kromek.com/cadmium-zinc-telluride-czt/

[26] Bejoy N. Pushpakaran, Anitha Sarah Subburaj, Stephen B. Bayne, John Mookken, Impact of silicon carbide semiconductor technology in Photovoltaic Energy System, Renewable and Sustainable Energy Reviews, Volume 55, 2016, Pages 971-989, ISSN 1364-0321, https://doi.org/10.1016/j.rser.2015.10.161

[27] Massoud T. Simnad, Nuclear Reactor Materials and Fuels, Editor(s): Robert A. Meyers, Encyclopedia of Physical Science and Technology (Third Edition), Academic Press, 2003, Pages 775-815, ISBN 9780122274107, https://doi.org/10.1016/B0-12-227410-5/00498-1

[28] Milbrath, B., Peurrung, A., Bliss, M., & Weber, W. (2008). Radiation detector materials: An overview. *Journal of Materials Research, 23*(10), 2561-2581. https://doi.org/10.1557/JMR.2008.0319

[29] Carron, N.J. (2006). An Introduction to the Passage of Energetic Particles through Matter (1st ed.). CRC Press. https://doi.org/10.1201/9781420012378

[30] J. Marshall, Stupid Science Word of the Month: Barn, Discover Magazine, 2008, https://www.discovermagazine.com/the-sciences/stupid-science-word-of-the-month-barn

[31] C.Subramanian, A.K.Suri and T.S.R.Ch.Murthy, Development of Boron-based materials for nuclear applications, BARC Newsletter, issue no. 14, p. 14-23, Mar-Apr 2010

[32] Suri, A.K. & Subramanian, C & Sonber, J.K. & Murthy, Tammana S R Ch. (2010). Synthesis and Consolidation of Boron Carbide: A Review. International Materials Reviews. 55. 4-40. https://doi.org/10.1179/095066009X12506721665211

[33] M. Barrachin, 7.17 - Silver-Indium-Cadmium Absorber Material Properties, Editor(s): Rudy J.M. Konings, Roger E. Stoller, Comprehensive Nuclear Materials (Second Edition), Elsevier, 2020, Pages 520-538, ISBN 9780081028667, https://doi.org/10.1016/B978-0-12-803581-8.11637-6

[34] T. Donomae, K. Maeda, 3.18 - Fast Spectrum Control Rod Materials, Editor(s): Rudy J.M. Konings, Comprehensive Nuclear Materials, Elsevier, 2012, Pages 509-534, ISBN 9780080560335, https://doi.org/10.1016/B978-0-08-056033-5.00078-1

[35] David Emin and T. L. Aselage, A proposed boron-carbide-based solid-state neutron detector, J. Appl. Phys. 97, 013529 (2005); https://doi.org/10.1063/1.1823579

[36] A.N. Caruso, P.A. Dowben, S. Balkir, Nathan Schemm, Kevin Osberg, R.W. Fairchild, Oscar Barrios Flores, Snjezana Balaz, A.D. Harken, B.W. Robertson, J.I. Brand, The all-boron carbide diode neutron detector: Comparison with theory, Materials Science and Engineering: B. 135. 129-133, 2006, http://doi.org/10.1016/j.mseb.2006.08.049

[37] K. Osberg, N. Schemm, S. Balkir, J.I. Brand, M.S. Hallbeck, P.A. Dowben, M.W. Hoffman, A Handheld Neutron-Detection Sensor System Utilizing a New Class of Boron Carbide Diode, in IEEE Sensors Journal, vol. 6, no. 6, pp. 1531-1538, Dec. 2006, https://doi.org/10.1109/JSEN.2006.883905

[38] Domnich,, V., Reynaud,, S., Haber,, R.A. and Chhowalla, M, Boron Carbide: Structure, Properties, and Stability under Stress, J. Am. Ceram. Soc., 94: 3605-3628. (2011), https://doi.org/10.1111/j.1551-2916.2011.04865.x

[39] Jemmis, E.D., Balakrishnarajan, M.M. The ubiquitous icosahedral B_{12} in boron chemistry. *Bull Mater Sci* **22**, 863–867 (1999). https://doi.org/10.1007/BF02745545

[40] D. R. Tallant, T. L. Aselage, A. N. Campbell, and D. Emin, Boron carbide structure by Raman spectroscopy, Phys. Rev. B 40, 5649 – Published 15 September 1989, https://doi.org/10.1103/PhysRevB.40.5649

[41] T. L. Aselage, D. Emin, S. S. McCready, and R. V. Duncan, Large Enhancement of Boron Carbides' Seebeck Coefficients through Vibrational Softening, Phys. Rev. Lett. 81, 2316 – Published 14 September 1998, https://doi.org/10.1103/PhysRevLett.81.2316

[42] M. Carrard, D. Emin, and L. Zuppiroli, Defect clustering and self-healing of electron-irradiated boron-rich solids, Phys. Rev. B 51, 11270 – Published 1 May 1995, http://doi.org/10.1103/PhysRevB.51.11270

[43] Steven J. Zinkle, Hiroyasu Tanigawa, Brian D. Wirth, Chapter 5 - Radiation and Thermomechanical Degradation Effects in Reactor Structural Alloys, Editor(s): G. Robert Odette, Steven J. Zinkle, Structural Alloys for Nuclear Energy Applications, Elsevier, 2019, Pages 163-210, ISBN 9780123970466, https://doi.org/10.1016/B978-0-12-397046-6.00005-8

[44] Zunger, A. and Katzir, A., Point defects in hexagonal boron nitride. II. Theoretical studies, Phys. Rev. B vol. 11, issue 6, p. 2378-2390, 1975, American Physical Society, https://doi.org/10.1103/PhysRevB.11.2378

[45] Douglas S. McGregor, J. Kenneth Shultis, Spectral identification of thin-film-coated and solid-form semiconductor neutron detectors, Nuclear Instruments and Methods in Physics Research Section A: Accelerators, Spectrometers, Detectors and Associated Equipment, Volume 517, Issues 1–3, 2004, Pages 180-188, ISSN 0168-9002, https://doi.org/10.1016/j.nima.2003.09.037

[46] Sunwoo Lee, John Mazurowski, G. Ramseyer, P. A. Dowben; Characterization of boron carbide thin films fabricated by plasma enhanced chemical vapor deposition from boranes. *Journal of Applied Physics* 15 November 1992; 72 (10): 4925–4933. https://doi.org/10.1063/1.352060

[47] Ali O. Sezer, J.I. Brand, Chemical vapor deposition of boron carbide, Materials Science and Engineering: B, Volume 79, Issue 3, 2001, Pages 191-202, ISSN 0921-5107, https://doi.org/10.1016/S0921-5107(00)00538-9

[48] Mirzokarimov, Mirzojamshed. Boron carbide hetero-isomeric device fabrication by PECVD from isomeric precursor ortho-carborane and meta-carborane. MS Thesis. University of Nebraska, 2019

[49] Seong-Don Hwang, Dongjin Byun, N. J. Ianno, P. A. Dowben, H. R. Kim; Fabrication of boron-carbide/boron heterojunction devices. Appl. Phys. Lett. 11 March 1996; 68 (11): 1495–1497. https://doi.org/10.1063/1.116266

[50] Hong, Nina, "An Exploration of Neutron Detection in Semiconducting Boron Carbide" (2012). ETD collection for University of Nebraska - Lincoln. AAI3503993. https://digitalcommons.unl.edu/dissertations/AAI3503993

[51] Peterson, George Glen, Electrical Characterization of Irradiated Semiconducting Amorphous Hydrogenated Boron Carbide, (2017). Mechanical (and Materials) Engineering -- Dissertations, Theses, and Student Research. 124. http://digitalcommons.unl.edu/mechengdiss/124

[52] Caruso, A. & Billa, Ravi & Balaz, Snjezana & Brand, J. I. & Dowben, Peter, The heteroisomeric diode. Journal of Physics Condensed Matter. 16. L139-L146. (2004), https://doi.org/10.1088/0953-8984/16/10/L04.

[53] A.N. Caruso, The physics of solid-state neutron detector materials and geometries, J. *Phys.: Condens. Matter* **22** 443201, 2010, https://doi.org/10.1088/0953-8984/22/44/443201

[54] Caruso, A. & Bernard, Laetitia & Xu, Bo & Dowben, Peter. (2003). Comparison of Adsorbed Orthocarborane and Metacarborane on Metal Surfaces. Journal of Physical Chemistry B. 107. 9620-9623. https://doi.org/10.1021/jp0354088

Chapter 2 - Background and Experimental Procedures

2.1 Boron Carbide Thin-Film Growth

2.1.1 Molecular precursors

Amorphous hydrogenated boron carbide thin films are developed by decomposition of boron carbide molecular precursors: closo-1,2-dicarbadodecaborane (ortho-carborane, $C_2B_{10}H_{12}$) and closo-1,7-dicarbadodecaborane (meta-carborane, $C_2B_{10}H_{10}$) [1-9]. Both semiconducting polytypes are compositionally similar as they are composed of the 12 atom icosahedra units previously discussed (Figure 1). The compositional difference between the two is the orientation of the carbon atoms on the icosahedra as shown in Figure 2 [2,3,10]. The icosahedra units are "surrounded" by hydrogen atoms bonded to both boron and carbon in their polymeric precursor form Figure 3 [10].

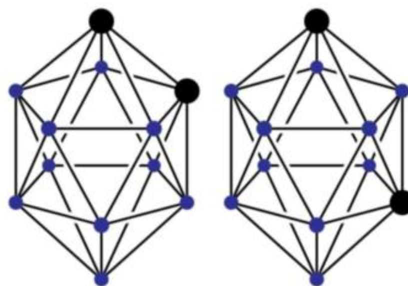

Figure 2 Ortho-carborane (left) and meta-carboran (right) icosahedra units

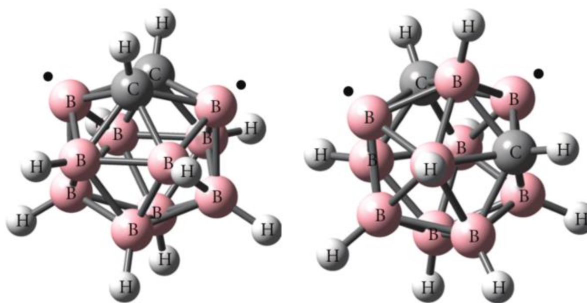

Figure 3 ortho-carborane (left) ad meta-carborane (right) with bonded hydrogen

As ortho-carborane and meta-carborane are structurally similar the electronic structure is expected to be similar as well, with calculated ground state molecular orbitals and their level ordering shown in Figure 4 [9,11].

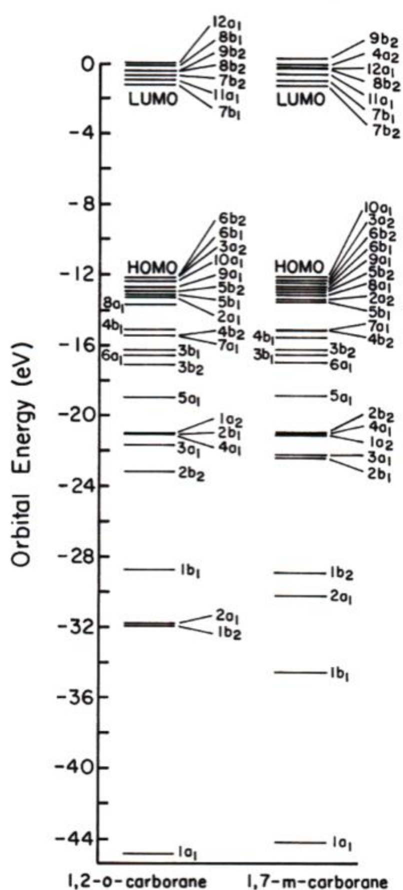

Figure 4 Calculated ground state molecular orbitals and their level ordering for ortho-carborane (left) and meta-carborane (right)

However, when photoemission and inverse photoemission studies were performed on adsorbed ortho-carborane and meta-carborane on metal surfaces, it was found that for meta-carborane the lowest unoccupied molecular orbital (LUMO) is significantly closer to the Fermi level, forming an n-type insulating thin-film [9,11]. For ortho-carborane the same studies showed the p-type characteristics of thin-film adsorbed on metals [9,11], showing that ortho-carborane and meta-carborane have intrinsic differences that are not

evident when doing the simple ground-state calculations [9,11] that could be dependent on the position of the carbon atoms in the icosahedral structure.

Ortho-carborane and meta-carborane molecular precursors come in the form of a polymeric powder produced by Sigma Aldrich company among others. As previously stated, borides like boron carbide are produced with abundant B^{10} isotope with 98% purity and molecular weight of 144g/mol. Before the process of deposition is performed, sealed glass bottles of precursors are kept in the refrigerator at 2-8ºC and handled in an inert environment when transporting it into the evaporation vials that are sealed in nitrogen or argon environments. The inert environment will significantly reduce the presence of water molecules and oxygen in the evaporation vials. The presence of oxygen and water molecules during evaporation of boron carbide precursors would significantly affect the as-deposited thin-film quality.

2.1.2 Plasma enhanced chemical vapor deposition (PECVD)

Extensive research has been completed since the early 1990s in optimizing the boron carbide thin-film deposition process. Physical vapor deposition (PVD) and chemical vapor deposition (CVD) have been used for boron carbide preparation in the laboratory. The PVD process is often expensive and difficult to control as it utilizes boron carbide targets, however CVD offers better controlled deposition of well defined, high purity single phase boron carbides [2]. Between classical CVD and plasma enhanced CVD (PECVD), the PECVD process is widely used for depositing a-BC:H films at lower temperatures and pressures than CVD processes. Plasma induced gas phases and surface interactions contribute to deposition mechanisms almost equally [2]. Therefore, the PECVD process is used to grow a-BC:H thin-films from o-carborane and m-carborane precursors in developing an a-BC:H neutron detector device.

In the PECVD process, plasma is generated from introduced gases by the electric field between two electrodes, either capacitively or inductively coupled. The difference between the two is shown on Figure 5, where in a capacitively coupled system, energy is transferred by the electric component of the RF field while in an inductively coupled system, energy is transferred by the electric field produced by the oscillating RF magnetic field [12-17].

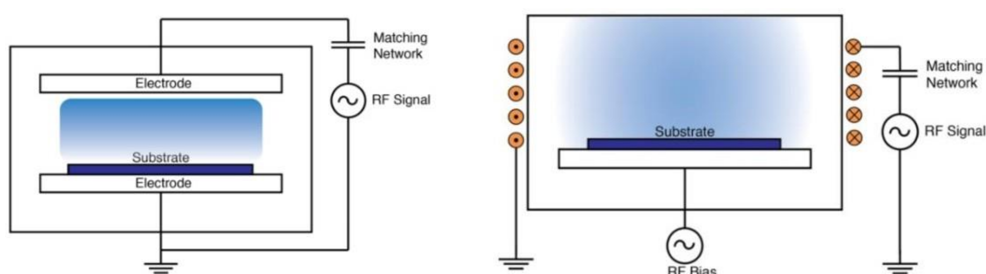

Figure 5 Capacitive coupled (left) and inductive coupled (right) plasma

Capacitively coupled plasma systems are commonly used when growing films via PECVD as there is a need to control the power deposition per unit area and the transport of gases in an out the reaction zone [13].

Reactions between neutral gas-phases of precursor components are often required for PECVD processes, so discharge pressures are much higher (0.1-1 Torr) than in the plasma etching process. This makes the mean free path small (0.003-0.3mm), and plasma densities in the range of 10^{9}-10^{11} cm^{-3} with fractional ionization in the range of 10^{-7}-10^{-4}. Deposition is limited by either gas flow rate, pressure, temperature, or discharge power. Therefore, the film properties such as composition, stress, morphology, adsorption rate of films are strong functions of these parameters, where temperature is optimized along with pressure, gas flow rate and power to produce desired film properties [13-17].

Deposition via PECVD can be done in a single chamber high vacuum system. The system used for this work is shown in Figure 6, with the schematic outline shown in Figure 7.

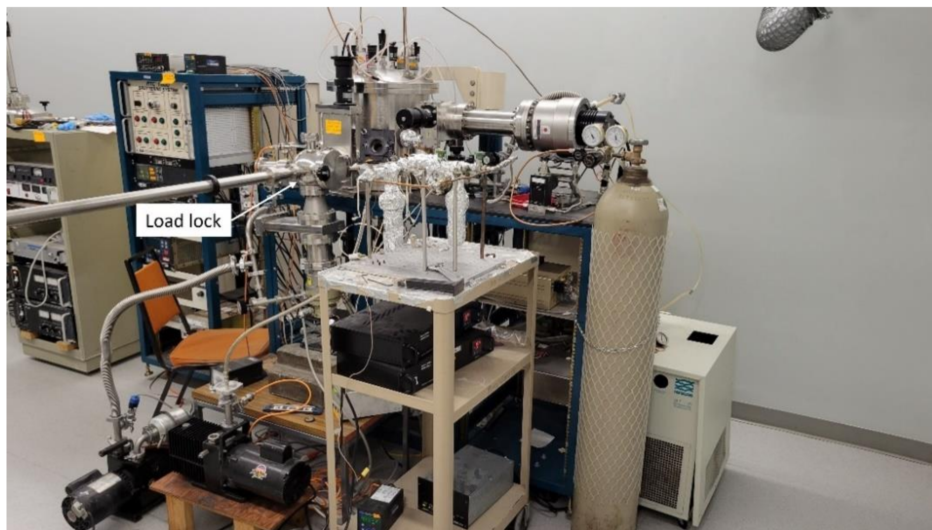

Figure 6 High vacuum deposition system

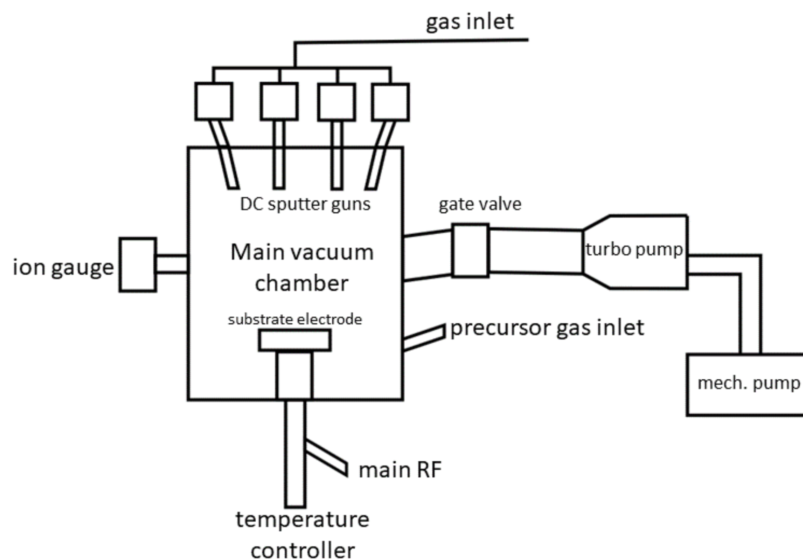

Figure 7 High vacuum system schematic

The plasma is produced by a 13.53MHz RF source driving the substrate. This specific frequency is most commonly used with RF sources because it was allotted by international communication authorities as it is the frequency which allows for radiation of a certain amount of energy without interfering with communications [15]. The substrate can be placed on either the grounded electrode or the driven electrode. The main difference between the two is the shape of the generated plasma above the substrate shown in Figure 8, and the voltage drop between the substrate and the plasma [15-17].

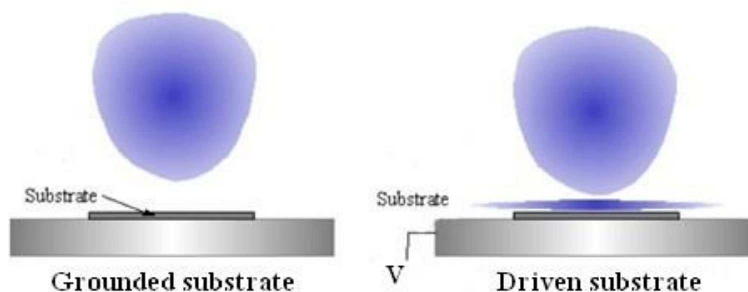

Figure 8 Plasma for grounded substrate (left) and driven substrate (right)

When a substrate is grounded, the applied RF voltage at the electrode driving the plasma is applied to the parallel plate capacitively coupled electrode above the substrate [14]. If that is the case, the plasma generated is in the shape of a “ball” between the biased electrode and grounded substrate (Figure 8 left). The region formed between the plasma and the electrodes (grounded substrate and driving electrode) is the sheath region. Because electrons are rapidly expelled from the region over which the negative potential is dropped and since that reduces the electron impact excitation reactions that lead to fluorescent emission, the sheath region does not glow as much as the plasma bulk. Therefore, the substrate is surrounded by a relative dark space, which may be a few μm to a few mm in size depending upon the plasma conditions [14-18]. When the substrate is grounded (Figure 9) the sheath potential formed between the plasma and the substrate will be equivalent to the plasma potential which is generally small [14].

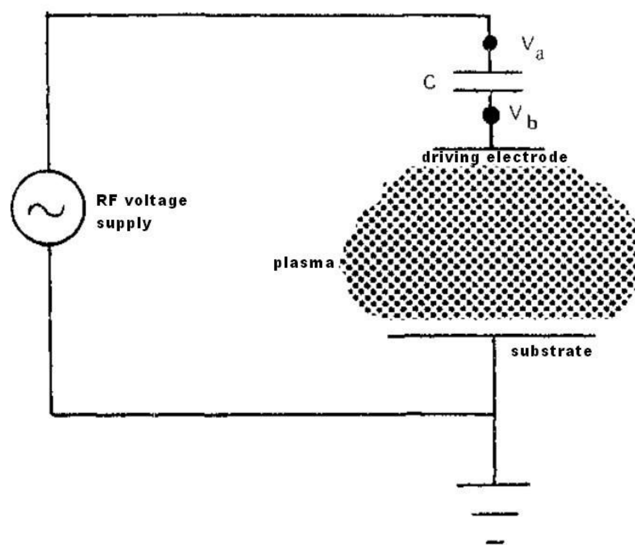

Figure 9 Grounded substrate plasma system schematic

However, if the substrate electrode is driven (Figure 10), the plasma moves closer to the substrate and the sheath (dark space) is formed around the substrate (Figure 8 right) [16].

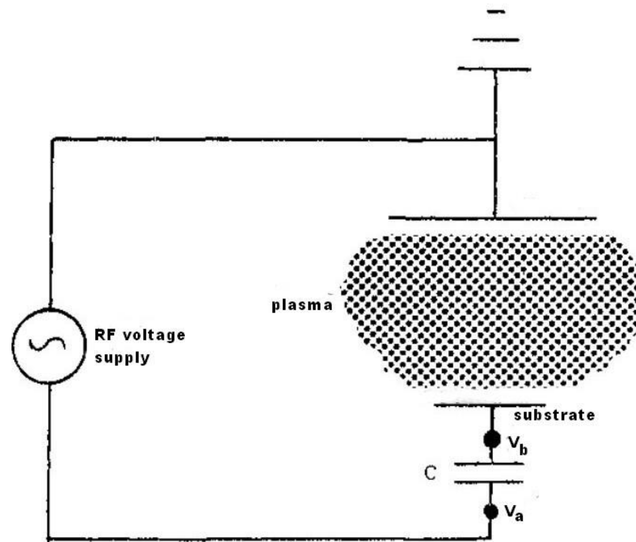

Figure 10 Driven substrate plasma system schematic

Driving the electrode with a constant RF applied voltage causes “self-biasing” of the substrate electrode. Self-biasing occurs when the electrode switches between positive and negative driving potential. As electrons require less potential to conduct a given current than positively charged ions, more electrons are drawn to the electrode during the positive cycle than positively charged ions during the negative cycle. Therefore, during the positive voltage cycle of the RF supply, voltage at the electrode will decay towards zero much faster, as opposed to during the negative cycle. At high frequencies, the cycle of higher number of electrons than positive ions being drawn to the substrate electrode will be repeated, displacing the substrate electrode towards the negative potential (Figure 11) [15].

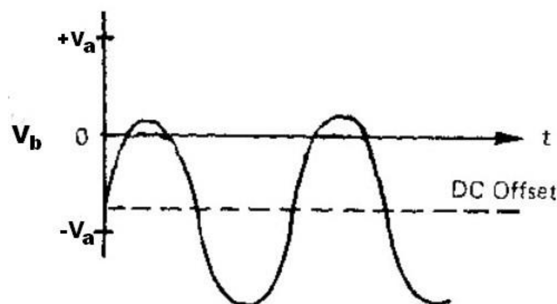

Figure 11 Driven substrate voltage waveform

The result of self-biasing is a constant negative dc-offset voltage forming at the substrate with the average approximately half the peak-to-peak magnitude of applied source voltage [15]. Unlike the grounded substrate where the sheath voltage of the substrate was equivalent to the plasma voltage, the sheath voltage of the driven substrate is the difference between V_b and the plasma voltage. As the plasma voltage is small, the voltage between the plasma and the substrate is equivalent to the negatively self-biased electrode. Therefore, the negative sheath voltage at the substrate can be a significant fraction of the peak applied RF voltage, with a small amount of time in the positive range, causing constant ion bombardment.   .

The advantage of driving the substrate electrode is concentrating the plasma reaction zone closer to the substrate, effectively decreasing the distance between where the precursor breakdown occurs and where it needs to be deposited. This improves the film's uniformity and porosity. While the same type of deposition occurs for both grounded and driven substrate case, the biased electrode drives the plasma towards the substrate increasing the area of the reaction zone of the polymeric precursors and the plasma, resulting in evenly distributed deposition reactions occurring throughout the area of the substrate.

Another advantage of the driven substrate is the minimized losses of the introduced precursor molecules. As the reaction zone is much closer to the substrate, precursor reactions tend to be closer to the desired deposition area, where in the grounded substrate case, the plasma is “spread” out between the two electrodes with reactions occurring throughout the plasma zone. This increases the probability of reaction products being lost within the system (adhesion to the chamber walls, interactions with contaminants, etc).

For PECVD, a turbomolecular or turbopump is the optimal pumping mechanism used to maintain the appropriate base pressure in the system as well as the appropriate operating pressures during depositions. Turbopumps (Figure 12) operate on the principle of multi-slotted fast spinning rotor blades at high velocities of 20000-30000 rotations per minute, that impart a preferred direction of molecular motion: they physically blow gas out of the chamber [14,19].

Figure 12 Leybold 450 series turbomolecular pump

The high velocity of the rotor blades would not be able to maintain the large pressure differential between vacuum and near atmospheric pressures, as the air on one end would create too much drag to allow for the blades to spin up to the required speed [14,19]. To avoid this, the turbo pump is backed up by a backing mechanical pump or a forepump (Figure 7) that will remove the gases pumped out by the turbopump. The back pressure of the turbopump is generally maintained in the range of 1-50 mTorr [14]. Additionally, to ensure the proper operation of the turbo pump and its ability to spin up, a secondary mechanical pump is connected to the system in order to reduce the base pressure from atmospheric 760 Torr to below 50 mTorr. Once that pressure is reached, the secondary mechanical pump is "gated off" from the system and the turbo pump is then opened to the system for high vacuum pumping through a gate valve (Figure 7).

To maintain the operating pressure higher than 1 mTorr during deposition with reduced contaminants (oxygen, water vapors, etc) in the system, the base pressure of the system before deposition needs to be in the 10^{-7} Torr range. Once the pressure in the range of 10^{-7} Torr is reached the pressure in the system can be increased for deposition conditions.

Temperature affects both pressure in the system, as well as film growth. In CVD, boron carbide film growth is thermally activated. However, in PECVD systems, plasma induced gas-phases and surface reactions contribute almost equally to the deposition process. Under the PECVD conditions of applied frequency of 13.56 MHz and pressures higher than 1 mTorr, electron and positive-ion densities are between 10^{9}-10^{12} cm^{-3} and the electron energies average 1-10 eV. This facilitates an energetic discharge environment sufficient to decompose gas molecules, reducing the temperature of the

chemical reactions compared to CVD processes [13,17]. The synthesis temperature of boron carbide reduces from 1000ºC during CVD to the range of 250-450ºC in PECVD [3].

As the driven substrate plasma enhanced chemical vapor deposition is advantageous for thin-film deposition of boron carbide, it is a preferred method of a-BC:H film growth. The effect of each parameter of the PECVD process on boron carbide thin-film growth will be further discussed in the following section.

2.1.3 Boron carbide thin-film growth via PECVD

When the substrate electrode is driven, uniform plasma is formed that covers the entire electrode surface. This results in more uniform film deposition compared to a grounded substrate deposition. The difference between two samples is shown in Figure 13. A sample deposited on a grounded substrate is shown on the left, while the sample deposited on a driven substrate is shown on the right. The effect of the driven substrate is the reduced thickness gradient.

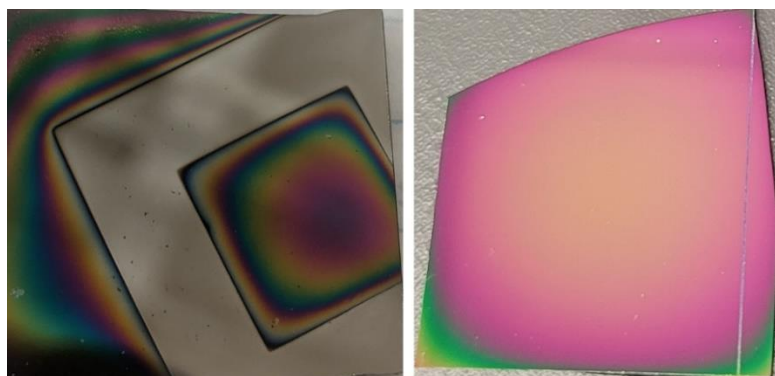

Figure 13 Deposited a-BC:H with the grounded substrate (left) and driven substrate (right)

Experiments showed that the optimal deposition substrate electrode bias for boron carbide films to be 150V. Varying the range of voltage bias produced either no deposited film or poor-quality films. The icosahedra units of the precursors need to be broken down from their hydrogen bonds in order to induce crosslinking between boron and carbon units, therefore the energy of the plasma and the reactions within need to be sufficient to induce complete crosslinking. If the voltage is too low, in the 50-100V range the deposition is not uniform since the fraction of precursor that is decomposed is low, causing porosity of the films as well as poor structural quality. If the applied voltage is too high, 200V, the argon ions in the plasma become an etching mechanism that removes

deposited film from the surface of the substrate faster than the deposition can occur. However, at 150V there is a balance between the etching mechanism and deposition rate where film is steadily deposited.

During the PECVD process for boron carbide thin-film growth with the driven substrate the operating pressures are between 180-230 mTorr. Higher operating pressure concentrates the plasma (Figure 8) around the substrate, reducing the distance between collisions, i.e., mean free path of the molecules. With higher pressure, the density of gases in the plasma is higher facilitating the breakdown of the icosahedra units in the molecular precursors for a-BC:H deposition to occur. However, there is an optimal pressure as well. Too high of an operating pressure (higher than 250 mTorr) could reduce film quality by introducing high quantity of molecular precursor resulting in deposition of unbroken precursor units, and lower pressure (below 150 mTorr) would reduce the number of collisions and reactions in the plasma, causing slow deposition of the a-BC:H film, introducing porosity into the film.

Experiments showed that the optimal deposition temperature for boron carbide films was in the range of 250ºC -350ºC. At room temperature there was no film growth on metallic, single crystal silicon or silicon dioxide substrates. The precursor does not break down at that temperature. At a temperature of 200ºC there is poor quality film growth with delamination quickly occurring in the atmosphere. At 250-350ºC the deposition of a-BC:H films is constant, repeatable, and stable, with no delamination, high abrasion resistance (scratches with a diamond tip pen only), and uniformity under an optical microscope.

The PECVD parameters for the a-BC:H thin-film deposition i.e., temperature, pressure, and RF voltage bias, used in the experiments are shown in Table 3.

Table 3 Boron carbide deposition parameters

Base pressure	1-5x10^{-7} Torr
Operating pressure	180-230 mTorr
Argon gas flow	50 sccm
Substrate temperature	350ºC (c-Si, metals substrate) 250ºC (a-Si:H substrate)
Precursor manifold temperature	100ºC (o-carborane) 75ºC (m-carborane)
Precursor gas flow	10-14 sccm
Precursor temperature	93-97ºC (ocarborane) 55-60ºC (m-carborane)
RF voltage substrate bias	150V
RF power pre-deposition	12-15W
RF power during deposition	22-25W

Different substrates can be used when growing thin-film a-BC:H. Depending on the ultimate purpose of a-BC:H films they can be single crystal silicon, sapphire, SiO_2, or various metals. Regardless of the substrate, preparation of its surface requires processing before a-BC:H deposition is performed to reduce the number of surface contaminants to facilitate effective adhesion of a-BC:H and produce an effective interface at the physical boundary. Single crystal silicon is processed by a hydrofluoric acid (HF) bath to remove the native oxide layer formed at the surface as well as other contaminants. Other substrates do not require strong processing with HF acid but are all processed by a methanol sonic bath for 15-20 min to remove any particles from the surface. The substrates are placed on the substrate stage inside the main chamber of the system via a

load locked transfer arm visible in Figure 6. The load lock is pumped by its own molecular turbo pump, which allows the low-pressure maintenance of the main system to be in the range of $7x10^{-8}$ to $5x10^{-7}$ Torr pressure. This facilitates a low-contaminant environment for deposition as well as efficient transfer of samples from atmosphere to vacuum, reducing time between depositions. Once the stable deposition conditions are met i.e., plasma, pressure and temperature inside the system, evaporation vial temperature is raised to the range for evaporating either ortho-carborane or meta-carborane precursors. The a-BC:H thin-film deposition process is performed by introducing the carborane molecular precursor in gaseous form carried by an inert gas (Ar) into the system. Ortho-carborane sublimes in the temperature range of 85-100ºC and meta-carborane in the temperature range of 45-60ºC. The precursor evaporation manifold apparatus is shown in Figure 14 and the schematic in Figure 15, and it is connected to the vacuum chamber via a valve at the position labeled in Figure 7. When not in use, the precursors are maintained at room temperature in sealed evaporation vials wrapped in temperature-controlled heating tape.

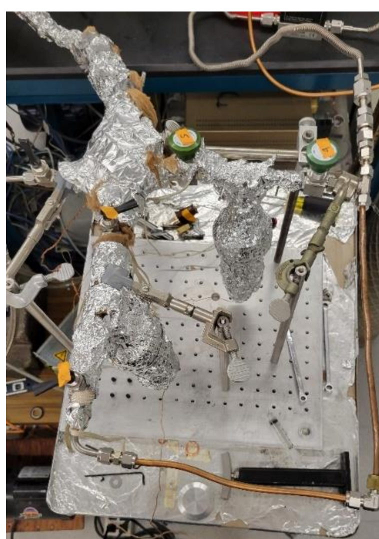

Figure 14 a-BC:H evaporation manifold

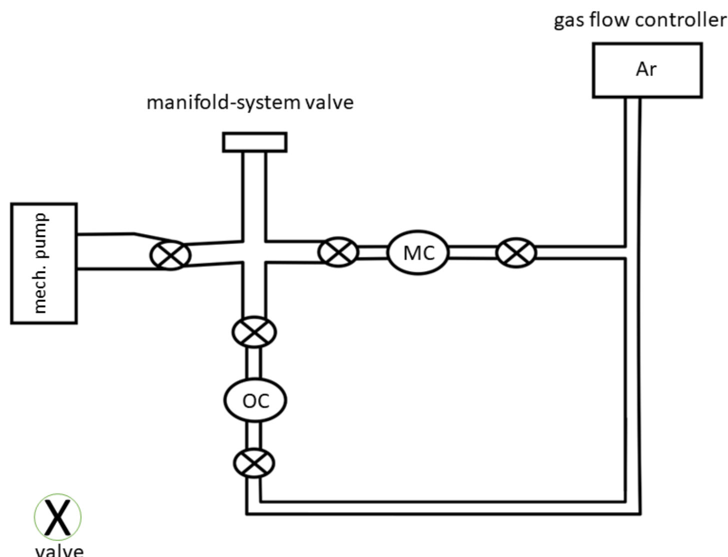

Figure 15 a-BC:H evaporation manifold schematic

When the temperature is stable, the vials are opened to the manifold that is always pumped by a mechanical pump (Figure 15). The manifold is always pumped to maintain low pressure (10^{-3}-10^{-4} Torr) before connecting it to the main chamber. When the flow of precursors with the carrier gas is stabilized within the manifold, the mechanical pump is isolated, and the manifold is opened to the system via a valve. The carrier gas (Ar in this case) carries the evaporated precursors through the manifold and into the system for deposition. As the precursors are introduced into the system, the plasma density increases (it visually becomes brighter) and the power is increased from its pre-deposition value due to the introduction of the precursors that raise the power by interacting with the formed plasma (Table 3). With the introduction of the gaseous precursor into the plasma reaction zone, steady deposition occurs on the substrate, with icosahedra molecules being broken down and crosslinked to produce a-BC:H thin films.

The operating pressure is achieved by partially gating off the turbopump valve, and that pressure is stable before the precursors are introduced into the system. The

chamber pressure will gradually increase as the gaseous precursors are steadily introduced into the system over time, requiring continuous monitoring of the deposition process. Additionally, the growth rate of the a-BC:H films depends on the evaporation mechanism and transport of the molecular precursor. With the quantity of the precursor present in the evaporation vials and the inherent temperature gradients in the transportation system, the introduction of the precursors into the system can vary between depositions. Therefore, both the pressure and the RF power need to be monitored during the deposition process in order to control the growth rate of the a-BC:H films. Introducing a high partial pressure of precursors into the chamber results in deposition on chamber walls, and poor deposition on the substrate. The resulting film tends to be porous and delaminates from the film substrate. Electronically, these films have shown higher resistivity and inconsistent results at different locations on the film, while structurally they are not as scratch resistant as properly deposited films. Samples shown in Figure 16 are the extreme end of a failed deposition with high delamination rate over time.

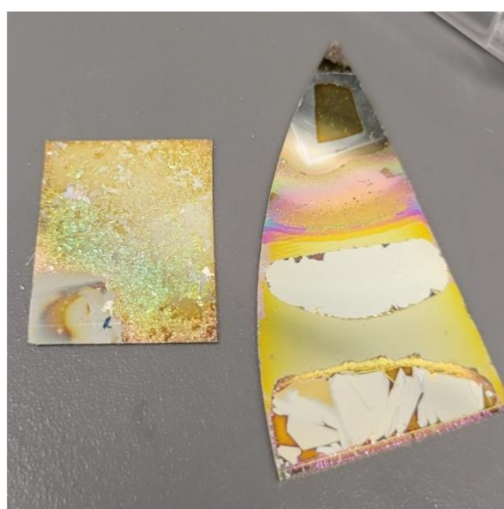

Figure 16 Delaminated a-BC:H films on a Chromium substrate

Additionally, if the partial pressure of precursor molecules introduced in the system is low, the deposition of a-BC:H is effectively "too slow" as the plasma etches the surface of the substrate faster than the films can be deposited.

The optimal deposition process is achieved through the balance of the parameters previously discussed, with the values of each parameter listed in Table 3. To monitor the film growth and understand the growth rate, in-situ ellipsometric measurements were performed using an M2000 J.A. Woollam ellipsometer with fixed angle and 380-1100nm wavelength range, shown mounted on the deposition chamber of the system in Figure 17.

Figure 17 M2000 J.A. Woollam ellipsometer mounted on the system chamber

Detailed discussion about ellipsometric characterization of a-BC:H films is included in a later chapter, but for purposes of film growth it is important to understand that an ellipsometric model was used to fit measured data in real-time as deposition is occurring. Multiple depositions and real-time thickness monitoring with in-situ ellipsometry can be used to correlate deposition time with thickness, as well as correlate how thickness corresponds to color when deposited on a given substrate. The color is the

result of the dielectric or “waveguide” effect of the film deposited on a given substrate. Some examples of a-BC:H films of various thickness deposited on chromium are seen in Figures 18-21.

Figure 18 a-BC:H 140nm film

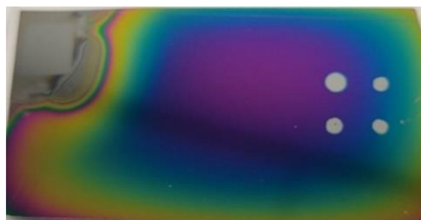

Figure 19 a-BC:H 172nm film

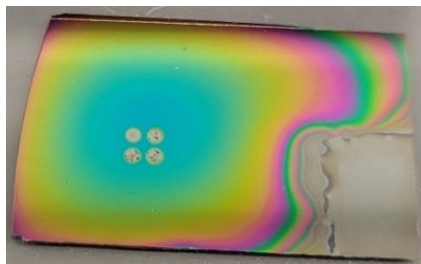

Figure 20 a-BC:H 190nm film

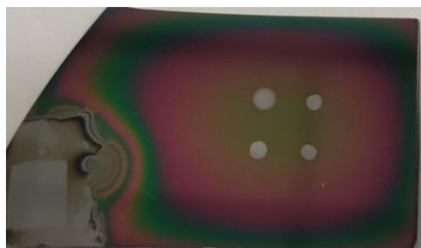

Figure 21 a-BC:H 348nm film

As much as in-situ ellipsometric collection of data is powerful, it eliminates the ability to rotate the samples on the substrate stage. Rotation of the samples during deposition affects the uniformity of the films as the flow of the gaseous precursors is at an angle on the side of the chamber (Figure 7). With rotation the a-BC:H film is deposited evenly and more uniformly on the substrate, producing a larger uniform area for characterization and metal contact deposition. The effect on the sample with and without rotation of the sample stage is shown in Figure 22

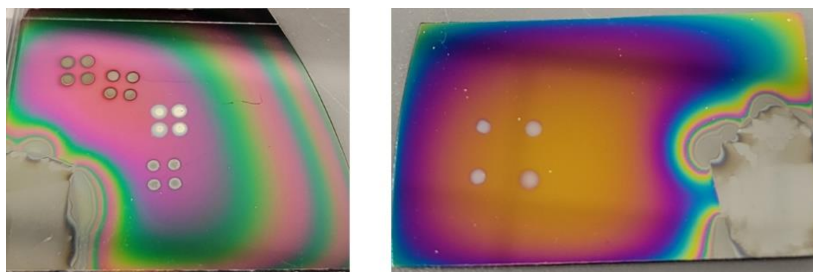

Figure 22 a-BC:H deposition without rotation (left) and with rotation (right) of sample stage

As it is extremely difficult to align the sample on the rotation stage for the ellipsometric beam to reflect off the sample and be perfectly aligned on the detector while rotating Therefore, visual recognition of sample thickness is substituted for in-situ ellipsometric data when rotating the sample during deposition. As previously stated, there is an effective color coding of a-BC:H films that provides a fairly accurate approximation of film thickness. Even though it is not a perfect method for monitoring a-BC:H film thickness, it is an optimized solution for the ability to grow uniform films.

Deposited metal dots can be seen on the samples in Figures 18-22. This will be discussed in a later chapter. It is important to note on these samples about the a-BC:H films, the color differences between samples of varying thickness and the difference in uniformity with rotation of the sample stage.

2.2 Metallization via physical vapor deposition (PVD)

Metal thin-film deposition is intended for various applications. For this work it is used primarily for electrical contacts in device fabrication. Metal films for electrical contacts are grown via sputtering, a physical vapor deposition process. During sputtering, incident ions physically remove atoms from the surface of a solid target of the desired material. Removed atoms or clusters of atoms then ballistically flow to and are deposited on a substrate [13,17]. The sputtering deposition process can be glow-discharge sputtering, ion beam sputter deposition, reactive sputter deposition, ion-assisted deposition, DC magnetron sputter deposition or RF sputter deposition [20].

DC magnetron sputtering is most commonly used for metal thin-film deposition as it is easily controlled, low cost and an efficient method to deposit metal film coatings or thin films onto a substrate. It is a process operated in a high vacuum system, in an environment without atmospheric gases, water vapors and contaminants.

The system in Figure 6, previously discussed for the PECVD process, is used for DC magnetron sputtering as well as PECVD. A simple schematic of the DC sputtering chamber is shown in Figure 23 [13].

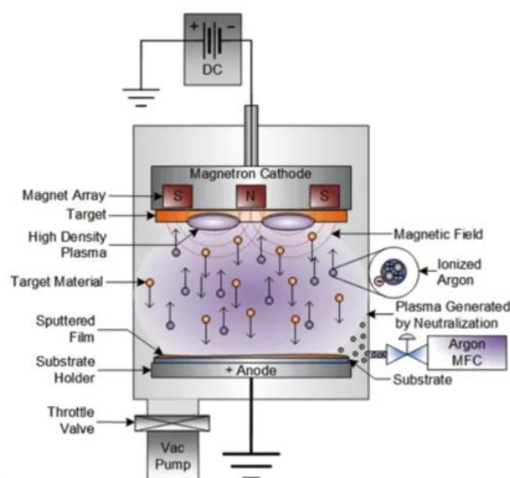

Figure 23 DC magnetron sputtering process schematic

When the system is evacuated of the contaminant gases, an inert gas (Ar) is introduced into the system, and atoms ionized by the applied DC voltage bombard the negatively charged target physically removing atoms from the target surface. The ionized Ar atoms, electrons and target atoms then flow towards the positively charged substrate and form a thin film over time.

To increase the efficiency of the deposition process by creating a dense plasma directly in front of the target surface, magnets are introduced behind the negatively charged target (Figure 23). The resulting magnetic field traps the electrons at the target surface increasing the plasma density at the target. This increases the rate at which the atoms are removed from the target surface via ion collisions, increasing the deposition rate. The dense plasma forms a doughnut shaped plasma in front of the target, resulting in non-uniform target erosion resembling a “racetrack” (Figure 24) [3,13,17,20,21].

Figure 24 Titanium (left) and copper (right) dc magnetron sputtered targets with the "racetrack"

As DC magnetron sputtering is an easily controlled, economical and repeatable process of depositing metal films, it is used for depositing electrical contacts while developing a-BC:H devices and performing contact resistance investigation at the metal/a-BC:H boundary.

Metal contacts are grown in the high vacuum AJA system shown in Figure 6. Low pressure in the deposition chamber is achieved by previously discussed evacuation

of atmospheric gases using a turbomolecular pump shown in Figure 12. For a more efficient transfer process, a load lock is utilized with a magnetic transfer arm and evacuated by a secondary turbomolecular pump. This isolates the high vacuum chamber from being exposed to atmosphere before every deposition and provides the ability to produce multiple samples in a short period of time. The system can hold four different targets at the same time as it was designed with four sputter guns. Argon is used for generating a glow discharge environment. As the guns are positioned at an angle the height of the rotation stage is calibrated to produce uniform films at the center of the substrate holder while the sample is rotating during deposition. Aluminum, silver, chromium, and titanium are the most commonly used metals for device contact fabrication. The DC sputtering deposition parameters are shown in Table 4.

Table 4 DC sputtering deposition parameters

Base pressure	1-5x10^{-7} Torr			
Operating pressure	2-4 mTorr			
Argon gas flow	40 sccm			
Substrate temperature	Room temperature			
Rotation (rpm)	20-25			
DC current (A)	Al	Ag	Cr	Ti
	0.350	0.200	0.360	0.280
Deposition time (min)	Al	Ag	Cr	Ti
	30	15	45	45

The applied current and deposition time are calibrated based on the different sputter rates of the targets, height of the stage, and operating pressure. For metal contacts it is important that the thin films are thick enough to produce a “short” i.e., film of low resistance, in the range of 0-5Ω. The parameters in Table 4 produce films approximately 200-300nm thick that exhibit the desired low resistance.

2.3 Boron carbide devices and fabrication

There has been extensive research in the development of neutron detector devices, both conversion layer devices developed by depositing a neutron reactive film on a semiconductor device, as well bulk solid-form devices made from neutron reactive semiconductors. The difference between the two will be discussed in the next section, as well as the development of all-boron carbide devices that was topic of controversy due to the confusion between the dielectric and semiconducting polytypes (ortho-carborane and meta-carborane previously discussed). However, as ortho-carborane and meta-carborane molecular precursors produce p-type and n-type a-BC:H films respectively via PECVD, it is possible to produce the boron-carbide and all-boron-carbide junction devices. Reported in literature, there are three different types of boron carbide devices that have been developed [2-7,22-28]:

1. Homojunction devices developed by transition metal doping boron carbide n-type or p-type [23,26-28].
2. Heterojunction devices from boron and boron carbide; single crystal silicon and boron carbide; as well as from two different types of boron carbide [4,23,25].
3. Heteroisomeric devices made from the decomposition of chemically similar but structurally different semiconducting boron carbides [2-7,22].

The following subsections present an overview of the conversion layer, bulk semiconductor, homojunction, heterojunction, and heteroisomeric devices. Among the various heterojunction devices there is an emphasis on single crystal/ a-BC:H devices, amorphous Si/ a-BC:H devices and their fabrication.

2.3.1 Thin-film coated devices and solid-form (bulk) devices

The distinguishable categories of neutron detectors are thin-film-coated detectors and bulk detectors [29]. As both devices release detectable ionizing radiation by utilizing neutron induced reactions, the fundamental difference between the two types is the location where those reactions occur within the detector device [29]. For thin-film-coated devices the neutron reaction occurs in the thin-film layer adjacent to the semiconducting diode, while for the bulk detector the reactions occur within the detector.

A simple thin-film-coated device is shown in Figure 25. It is fabricated by growing a boron film on a semiconductor diode.

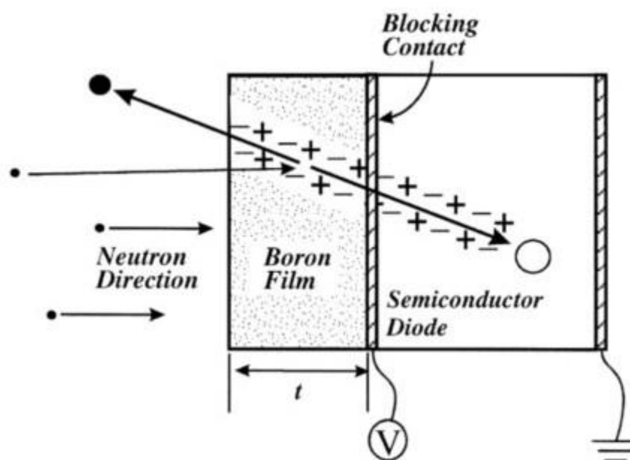

Figure 25 Simple thin-film-coated neutron detector

As neutron absorption occurs, the reaction ion must reach the depletion region of the diode. To do so, the reaction range of the reaction product ion must be greater than the distance between the interaction location and the interface between the thin-film and the semiconductor diode [29]. Once the reaction ion reaches the depletion region of the semiconductor diode, charge carries i.e., electron-hole pairs are created. As the operation of detectors is generally in reverse bias, generated electron-hole pairs will drift to their

respective electrodes: holes from n-side to p-side and electrons from p-side to n-side – shown on the band diagram in Figure 26 [29,30]. This drift of charge carriers will induce a signal within the semiconductor device that can be quantified as neutron detection.

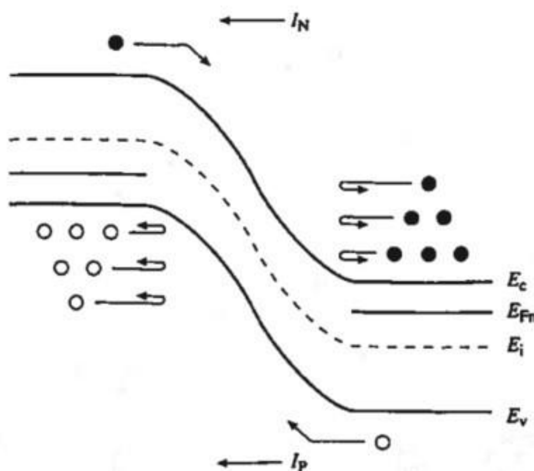

Figure 26 Reverse biased p-n junction band diagram

Even though the conversion layer detectors are efficient low-cost devices made from naturally abundant neutron reactive coatings (boron, lithium) and single crystal silicon diodes, a significant drawback of this type of neutron detector is the damaging effect of neutron radiation on single crystal structures [31,32]. Crystalline semiconductors are highly dependent on the lattice structure and high energy particle bombardment damages the lattice throughout the material by introducing defects, regions where atoms are knocked from their sites in the lattice and placed in interstitial positions [32]. The defects produce energy levels in the band gap of the semiconductor and change the electrical properties of the semiconductor [32]. Additionally, localized damage regions occur because of the high energy of primary atoms that are knocked from their sites. These localized regions are clusters of defects introduced throughout the silicon structure causing decrease in carrier mobility [31-33]. Therefore, over time nuclear radiation

induces damage to the silicon structure and its electronic properties making the conversion layer detectors not an effective long-term active detector.

Bulk semiconductor devices use neutron reactive materials i.e., boron carbide as their layers. These devices can absorb neutrons within the detector without the need for a boron (or other neutron reactive material) conversion layer. As the reaction products, ejected He and Li ions, are released directly within the detector, and electron-hole pairs are generated within a semiconductor (Figure 27) [29].

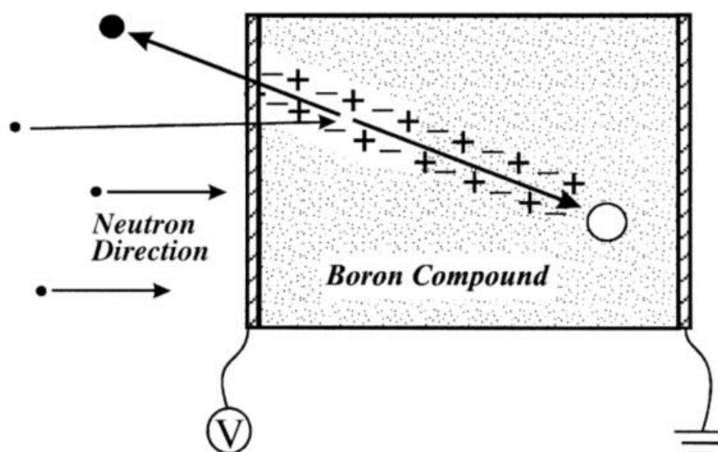

Figure 27 Simple bulk semiconductor neutron detector diode

This reduces the losses that can occur within the neutron reactive (conversion) layer, as well as losses at the interface of the conversion layer and the semiconductor diode. Additionally, as vacancies created by fission fragments in amorphous boron carbide tend to spontaneously recombine resulting in a self-healing property of the material unlike the single crystal silicon. Therefore, over time bulk semiconductor detectors developed from amorphous boron carbide have minimal degradation due to radiation damage. The charge carriers generated within the neutron reactive boron

carbide (or similar material) can then be captured by the internal electric field of the semiconductor device, resulting in a current flow proportional to the generated charges.

Similar to the conversion layer devices the semiconductor detectors are operated in reverse bias, and as charges generated drift towards their respective electrodes, the signal is induced within the detector that can be quantified as neutron detection. Therefore, the bulk semiconductor detector made from boron carbide possesses the ability to both generate and capture generated charges, and along with minimized degradation due to radiation damage over time, makes it a powerful semiconductor for producing various types of neutron detector devices.

2.3.2 Boron carbide homojunction devices and doping

Homojunction devices are formed from two layers of the same type of semiconductor, with the same band gap. However, to form a p-n junction diode the two layers of the homojunction are doped differently [30,34,35]. The p-n homojunction band diagram under equilibrium is shown on Figure 28 [30,35].

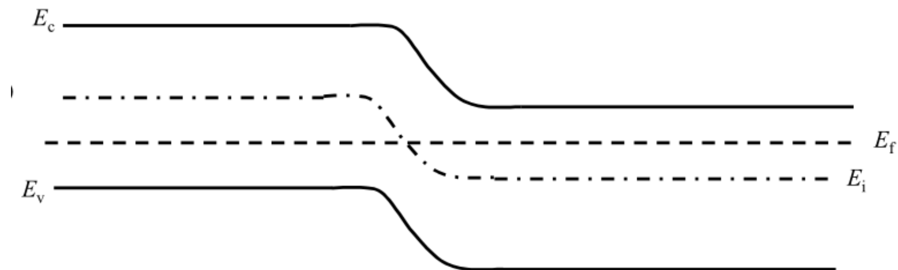

Figure 28 Homojunction band diagram in equilibrium

A depletion region is formed at the junction of p-type and n-type semiconductors [30,35]. The Fermi energy level (E_f) must remain aligned throughout the junction, so band bending shown in Figure 28 must occur. For band bending to occur, charge carriers (electrons) must transfer from n-type to p-type layer and holes from p-type to n-type layer, leaving behind ionized donors and acceptors respectively [30,35].

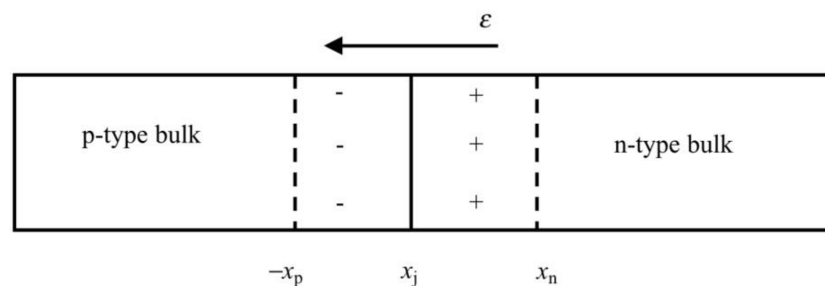

Figure 29 p-n junction depletion region

Ionized dopants produce a positive and negative space charge at the junction shown in Figure 29, resulting in a built-in electric field (ε) [30,35]. The electric field is in the direction from the n-side to p-side of the junction and serves to sweep free charge carriers across the space charge region, depleting the region from free carriers. Hence why the region is called the "depletion region" [35].

All-boron carbide homojunction devices have been fabricated by layering undoped and doped a-BC:H films deposited from one molecular precursor, ortho-carborane [23,26-28]. The film structure of a doped film is shown in Figure 30, small circles representing the evenly distributed dopants throughout the a-BC:H film [11]. The possible molecular schematic model of the icosahedra bonding with the introduced dopants is shown in Figure 31 [11]. This is not the exact representation of how each dopant will bond with the a-BC:H icosahedra, but an example of how structurally a-BC:H could be bonded when doped.

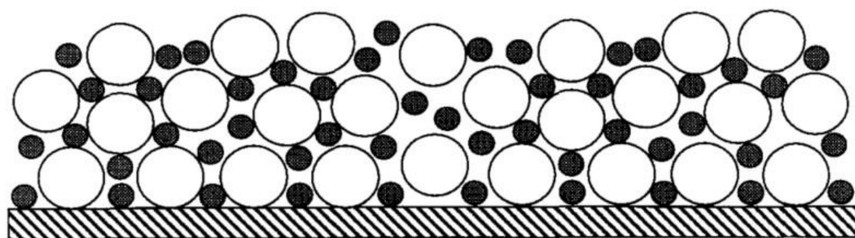

Figure 30 a-BC:H doped film structure with dopants (black circles) bonded throughout the film

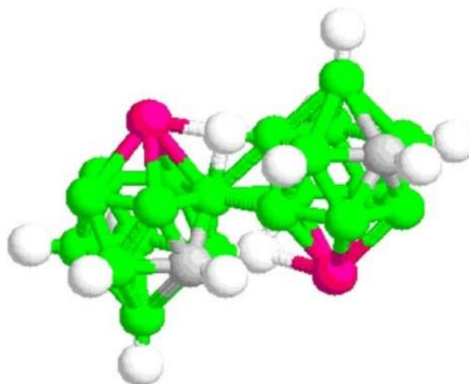

Figure 31 Possible molecular schematic of a-BC:H icosahedra and dopant bonding B (green), C (grey), H (white), dopant (red)

Dopants like transition metals are able to dope a-BC:H films [25-28]. Homojunction devices are developed in sequential process of depositing an a-BC:H film from ortho-carborane doped during deposition with either Co from cobaltocene, Ni from nickelocene or Fe from ferrocene [25-28], on a metal substrate; then depositing an undoped a-BC:H layer from ortho-carborane with metal top contacts. The structure and corresponding V-I curve for an a-BC:H homojunction device is shown in Figures 32 and 33 [27]. As discussed, a-BC:H films grown from ortho-carborane exhibit p-type behavior as deposited. In fabricating a homojunction device, ortho-carborane is the molecular precursor used to grow both a-BC:H layers.

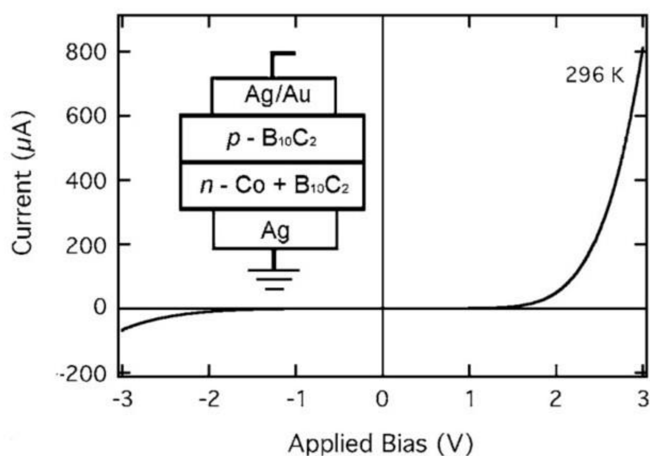

Figure 32 Structure and V-I characteristic of a-BC:H homojunction device via Co doping

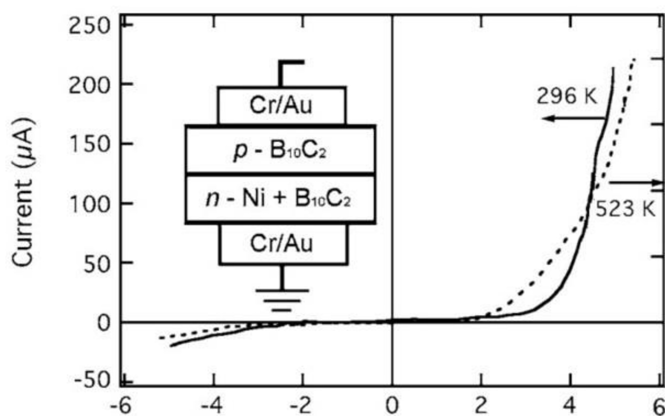

Figure 33 Structure and V-I characteristic of a-BC:H homojunction device via Ni doping

However, the resulting V-I characteristics of these devices clearly exhibit p-n junction device behavior. As previous attempts at developing a homojunction device by using meta-carborane as the precursor have failed [27], it can be deduced that the transition metals are n-type dopants for a-BC:H films. Additionally, the effect of transition metal doping of a-BC:H appears to have type converted the a-BC:H layer deposited from ortho-carborane. As a-BC:H from ortho-carborane produces as-deposited p-type a-BC:H films, doping appears to convert the a-BC:H layer from p-type to n-type during deposition [25,26], making it possible to produce an all a-BC:H p-n homojunction devices.

2.3.3 Boron carbide heterojunction devices

Heterojunction devices are formed by layering two dissimilar semiconductor materials [35-39]. Dissimilar usually means that the two semiconductor materials have different bandgap energies, doping concentrations, dielectric permittivities (ε_s), work functions ($q\phi_s$) and electron affinities ($q\chi$) [38,39]. Work function is defined as energy required to remove an electron from the Fermi level to the position just outside of the material (vacuum level), while the electron affinity is defined as the energy required to remove the electron from the bottom of the conduction band to the vacuum level [38,39].

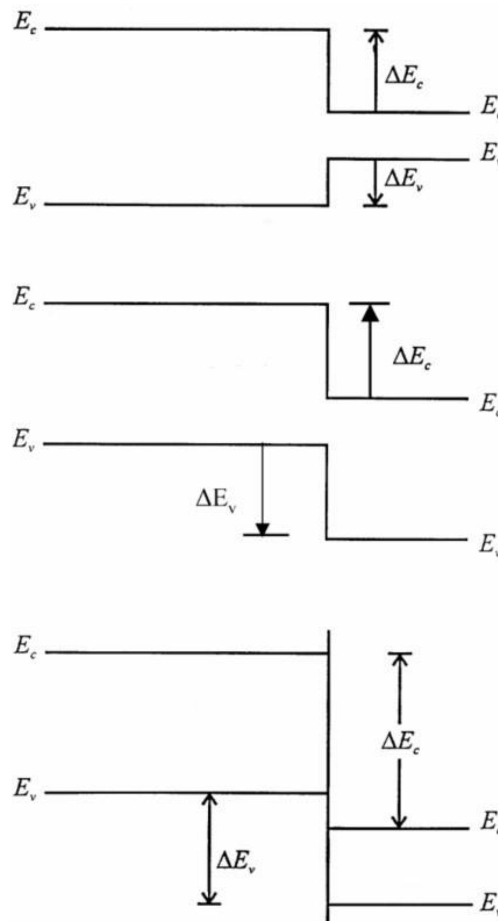

Figure 34 Types of heterojunction band structures: type I (top), type II (middle), type III (bottom)

As the material properties are different between the two layers, there is a discontinuity in the band structures depending on the differences in band energies and electron affinities. The Fermi level needs to be continuous, so there will be discontinuities at the junction boundary that are dependent on the valence and conduction band energies differences (ΔE_c, ΔE_v), electron affinities and doping. Based on these differences, the band structures formed can take form in three different types shown in Figure 34 [39]. Therefore, a large variety of heterojunctions can be formed by layering n-n, p-p, p-n, n-i (intrinsic) type materials.

There have been various heterojunction devices reported that utilize a-BC:H as one of the device layers. Initially a-BC:H was used to develop p-n junctions with single crystal n-type or p-type silicon [25,36] (discussed in the following section). Subsequently, boron (Figure 35) [4], boron carbide from icosahedra precursor closo-1-phospha-2 carbadodecaborane (1,2-$PCB_{10}H_{11}$) (Figure 36) [40] and silicon carbide (Figure 37) [41] were investigated as layers for producing an a-BC:H heterojunction device.

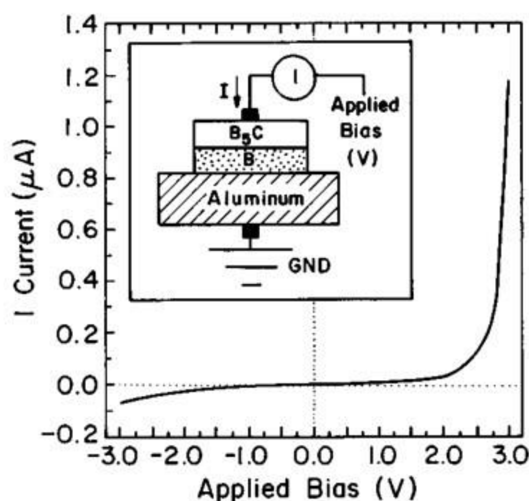

Figure 35 Boron/ a-BC:H heterojunction device V-I characteristics

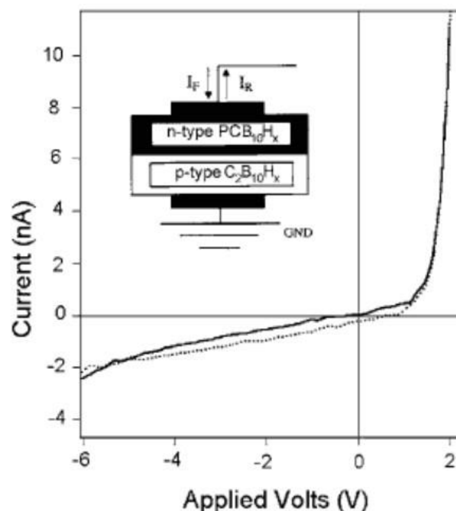

Figure 36 V-I characteristic of a-BC:H heterojunction device made from 1,2-$PCB_{10}H_{11}$ and ortho-carborane precursors

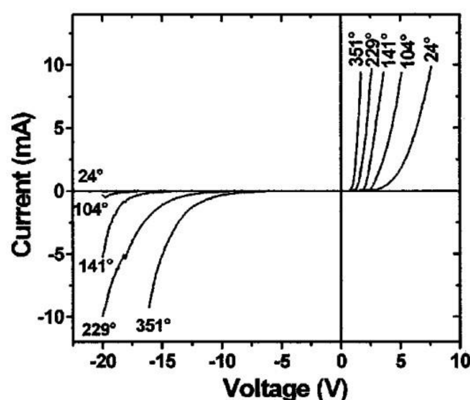

Figure 37 V-I characteristics of a-BC:H (p)/SiC(n) heterojunction device with Au metal contacts at varying temperatures

The boron/ a-BC:H device is advantageous as boron has high neutron absorption cross section and layered with a semiconducting a-BC:H as a compound of boron would have a higher neutron absorption rate than most devices. As previously discussed with boron conversion layer devices that utilize single crystal semiconductors for collecting generated charge carriers, radiation damage in single crystal structure reduces the longevity of these devices. As amorphous boron carbide has minimized degradation due to radiation damage over time, boron/ a-BC:H heterojunction devices have potential for

effective neutron absorption devices. However, amorphous boron carbide has much higher resistivity than a single crystal semiconductor like silicon, which produces a limited current output (1µA at ~2.7V) in these heterojunction devices that can be seen in Figure 35.

Both heterojunction devices made from n-type 1,2-$PCB_{10}H_{11}$ and p-type ortho-carborane precursors and devices made from a-BC:H and SiC have not been developed enough to clearly understand their behavior. As n-type 1,2-$PCB_{10}H_{11}$ has phosphorus in its structure, it should produce lower resistivity films as reported in [40], however the current output of the device is in the nA range at 3V bias (Figure 46). The a-BC:H/SiC heterojunction device reported in [41] is produced with the purpose of developing detectors that operate at higher temperatures. As gold is used as the contact, which exhibits Ohmic behavior with SiC at temperatures higher than 150ºC [41] and Schottky behavior at lower temperatures, the device V-I characteristics at lower than 150ºC would have the effect of the Schottky contact contributing to the device behavior (Figure 37).

The fabrication process of single crystal silicon/a-BC:H heterojunction device is discussed in the following section. It is developed as a foundational device for understanding a-BC:H in forming a heterojunction device and discussed in detail in the results chapter. Because single crystal Si is a well-known and understood material, starting from the c-Si-a-BC:H devices: band structure, interface, contacts, and device performance can be investigated before device fabrication of heteroisomeric or other heterojunction devices. However, as single crystal Si cannot be used in neutron detection due to its crystalline structure, the hydrogenated amorphous silicon is then examined as a substitute in producing a heterojunction neutron detector device.

2.3.4 Single crystal Si/a-BC:H device fabrication

Compared to previously discussed heterojunction devices that utilize either boron, SiC or another type of carborane precursor with a-BC:H to produce neutron detectors, single crystal silicon as a semiconductor is understood the most. It has the most optimal semiconductor features (mobility, low resistivity, bandgap, etc) for producing a higher quality (larger output and lower turn-on voltage) p-n heterojunction device with a-BC:H. Single crystal silicon-amorphous BC heterojunction devices were reported in literature [23,34] as well as experimentally developed in the laboratory by depositing n-type a-BC:H from meta-carborane on p-type single crystal silicon and p-type a-BC:H from ortho-carborane on n-type single crystal silicon. The single crystal silicon was prepared by hydrofluoric acid bath to strip oxides and organics from the surface for better contact interface with metal and a-BC:H.

It has been determined that the order of the a-BC:H deposition and the post-HF acid bath affects the interface between the silicon and metal contact and potentially the single crystal Si and a-BC:H contact interface as well. When the metal contact (e.g., Al) is deposited on the rough side of a silicon wafer first, it forms an Ohmic contact at the metal-Si interface. When the wafer is then transferred out of the system and metal deposited on the smooth side of the silicon wafer, a Schottky contact forms at the metal-Si interface.

Figure 38 shows the V-I characteristic of an Al-Si(p)-Al structure developed by depositing Al on the rough side of the p-type single crystal Si immediately after the HF acid process and Al top contact deposited on smooth side after the transfer process. In this procedure, there was no secondary HF acid processing of the smooth side of the

wafer, only deposition of Al after the rough side was metalized. This order of metallization produced a diode V-I curve characteristic of this structure, indicating the formation of a native oxide layer on the smooth side of the single crystal wafer during the transfer process.

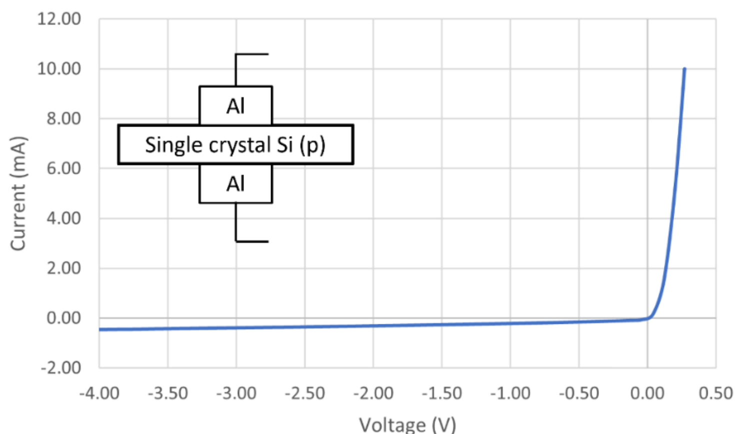

Figure 38 Al-Si(p)-Al V-I characteristic (Al on rough then shinny side deposition post-HF acid process

However, when the metal contact is deposited on the smooth side first, immediately post-HF acid processing, and then a metal contact deposited on the rough side, both metal-Si boundaries exhibit Ohmic behavior. Shown in Figure 39 are V-I characteristics of the Ohmic behavior for Al-Si(p) contact on both smooth and rough side of the Si wafer. Kapton tape was used to mask the middle of wafer to produce a gap between metal contacts for testing the V-I characteristics.

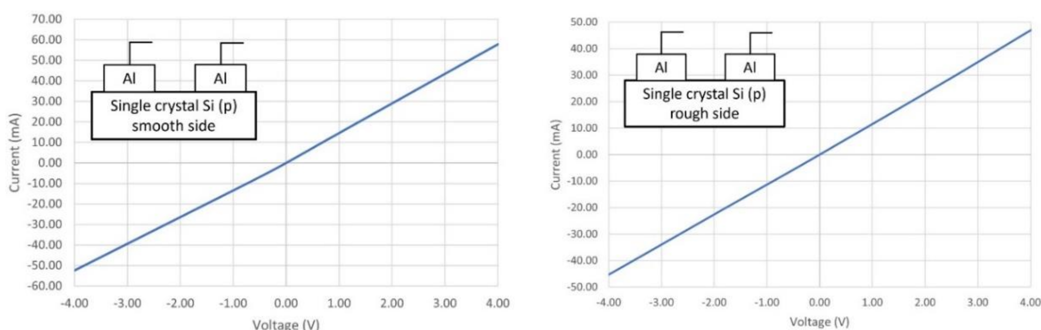

Figure 39 V-I characteristic of Al contact on smooth side (left) and rough side (right) of single crystal Si(p) post-HF acid processing

The exact reason why this occurs is unclear, aside from the assumption that the native oxide on the smooth side is formed more rapidly than on the rough side of the wafer during the transfer between the two metal depositions processes.

It is important to understand this behavior before developing Si/ a-BC:H heterojunction devices as growing a-BC:H films on single crystal Si with a native oxide layer will produce a poor interface at the boundary due to the presence of oxygen. Therefore, the device fabrication process is designed as illustrated in Figure 40. All the single crystal Si/ a-BC:H devices investigated were fabricated following this process.

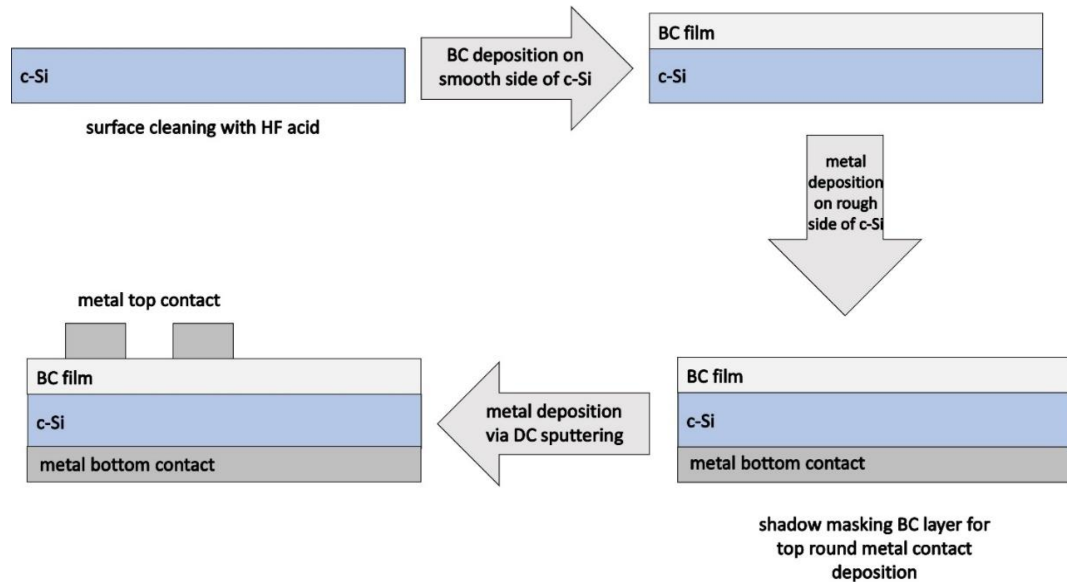

Figure 40 Procedure for single crystal Si/a-BC:H device fabrication

2.3.5 Heteroisomeric a-BC:H/a-BC:H device

Heteroisomeric devices are a different class of diode compared to previously discussed homojunction and heterojunction diodes. They are developed by layering p-type and n-type a-BC:H films, that are grown by decomposition of semiconducting boron carbide molecular precursors ortho-carborane and meta-carborane, previously discussed. Even though these semiconducting boron carbide polytypes are compositionally similar, they are electronically different, as ortho-carborane produces p-type and meta-carborane produces n-type a-BC:H films. The resulting devices do not make a conventional homojunction nor a heterojunction diode, but a heteroisomeric diode [3,7,21].

There are certain advantages to developing a-BC:H/a-BC:H heteroisomeric devices compared to previously discussed conversion layer and heterojunction devices. As both layers in the device are boron rich semiconductors consisting of B^{10} isotope that has a large neutron absorption cross-section (section 1.3), heteroisomeric devices should exhibit improved detection sensitivity as well as longevity as amorphous a-BC:H is more resistive to degradation due to radiation damage (section 1.4). Because boron carbides have been shown to exhibit wide depletion regions [1,7], increasing thickness of the a-BC:H layers should make the heteroisomeric diodes opaque to epithermal neutrons increasing sensitivities to thermal neutrons. Additionally, as the devices are fabricated by PECVD and without transition metal dopants unlike homojunction devices (section 2.3.2), absence of activatable transition metals can eliminate false positive detection readings. Furthermore, B^{10} enrichment of a-BC:H can be performed without introducing added contaminants to the films during deposition [7]. To fabricate a heteroisomeric diode, p-type and n-type a-BC:H films are grown in sequence, in-situ, on a metal

substrate. The order of p-type or n-type a-BC:H deposition is determined by the metal substrate of the specific device structure, e.g., if Ti produces an ohmic contact with n-type a-BC:H and Schottky with p-type a-BC:H, the order of a-BC:H device layer deposition would be n-type a-BC:H deposition on the Ti substrate followed by p-type a-BC:H deposition on the n-type layer forming the heteroisomeric p-n device. The V-I characteristic of a heteroisomeric device is shown in Figure 41.

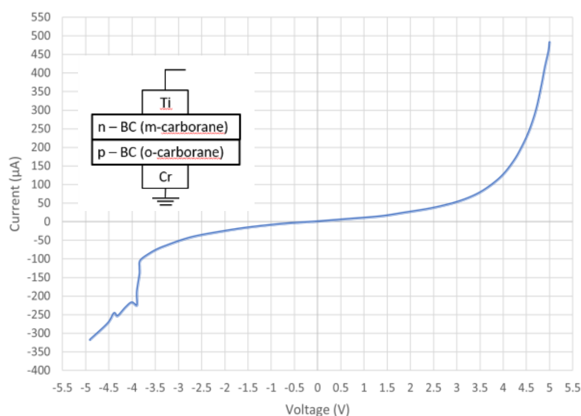

Figure 41 V-I characteristic of a-BC:H heteroisomeric device

The disadvantages of the heteroisomeric devices are rooted in high resistivity of the a-BC:H films grown from ortho-carborane and meta-carborane. Increasing the thickness of a-BC:H layers can produce opaqueness for the epithermal neutrons, but thicker a-BC:H films would be highly resistive to the flow of generated charges from the neutron absorption reactions. Doping of a-BC:H would generally solve this problem, but as it was previously discussed in section 2.3.2, a-BC:H films produced from ortho-carborane precursors type convert from p-type to n-type when doped, which is the basis for fabricating a-BC:H homojunction diodes. However, a-BC:H grown from meta-carborane can be doped by 3d transition metal dopants, which would produce less resistive a-BC:H films but would introduce the higher probability of false positive signals previously discussed.

2.3.6 Amorphous hydrogenated Si/a-BC:H device and fabrication

Hydrogenated amorphous silicon (a-Si:H) similar to single crystal silicon is a well understood material, whose properties and growth have been widely researched over the years in the photovoltaic device fabrication field [42-49]. There are certain key factors that provide higher potential for hydrogenated amorphous silicon to be incorporated into the neutronvoltaic heterojunction device structures than its single crystal counterpart.

First, a-Si has a comparable electron affinity of 3.92eV to single crystal silicon 4.0eV [42]. In theory, this should provide a similar behavior when forming a heterojunction with a-BC:H to c-Si. Unlike c-Si, due to its lack of crystal structure, a-Si:H is more resistive to radiation, which provides potential for conversion layer device fabrication as well as heterojunction diode fabrication.

However, a-Si as a semiconductor is undesirable for device fabrication as it has too many dangling bonds, i.e., unsatisfied valences in its amorphous structure that exist in the order of $10^{19}cm^{-3}$. These unsatisfied valences act as recombination centers that reduce carrier lifetimes and pin the Fermi energy level so that neither n-type nor p-type doping is possible [45]. By introducing hydrogen during a-Si growth process, the level of these defects is reduced by orders of magnitude ($10^{16}cm^{-3}$) for 10% of hydrogen incorporation during deposition [44,45,47]. The differences between c-Si, a-Si, and a-Si:H are illustrated in Figure 42 [41]. Introduced hydrogen combines with the dangling bond, reducing the defect density and improving the doping ability of a-Si [42,43]. Additionally, a-Si:H has potential for operation in environments with higher radiation than c-Si, as well as higher temperature environments due to its temperature insensitivity

[42-50]. Finally, a-Si:H is easy to produce via PECVD and it is easily doped during the growth process [45].

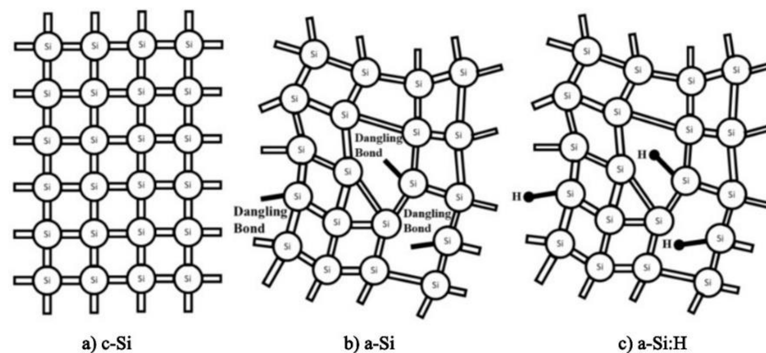

Figure 42 Crystaline silicon (a), amorphous silicon (b), hydrogenated amorphous silicon (c)

The combination of these attractive properties makes a-Si:H a low-cost, reproducible material worth investigating for fabrication of heterojunction devices with a-BC:H for neutron detection. In collaboration with National Renewable Energy Laboratory, p-type a-Si:H films were used to fabricate and investigate a-Si:H/ a-BC:H neutron detectors. The device fabrication process is illustrated in Figure 43.

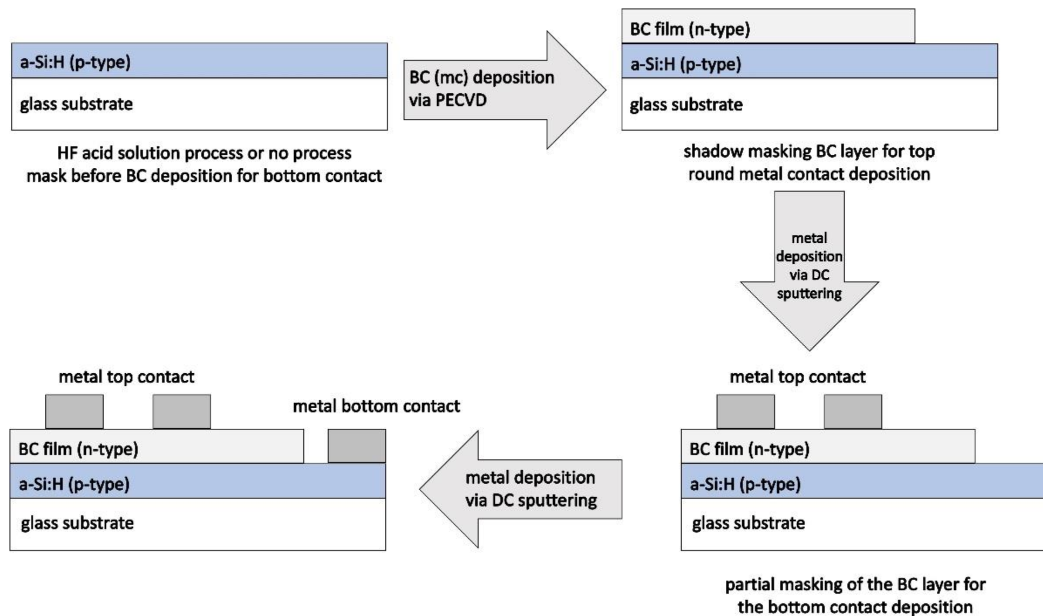

Figure 43 a-Si:H/ a-BC:H heterojunction device fabrication procedure

2.4 Metal/a-BC:H contact resistance

Metal contacts are an integral part of device fabrication, as devices require electrical contacts to be deposited on the device or used as a bottom contact substrate over which a-BC:H films are grown. Therefore, it is important to understand the metal/a-BC:H junction.

Contact resistance is defined as the additional resistance to an ideal contact formed at the metal-semiconductor interface. It can be visualized as an ideal contact in series with a resistor. This allows for either theoretical or experimental derivation of the contact resistance that provides the correction term for the actual losses at the metal-semiconductor boundary [51]. Additionally, resistivity of a semiconductor material can be mathematically obtained from the contact resistance experimental measurements based on Ohm's law and the relationship between the bulk semiconductor resistance and contact resistance. Utilizing Ohm's law therefore requires the metal-semiconductor contacts to exhibit linear (ohmic) behavior, where carriers can flow freely between the semiconductor and the metal [28,51-53].

Therefore, to optimize a-BC:H devices, it is important to differentiate metals that form Schottky contacts and Ohmic contacts with the a-BC:H and understand and quantify the effect of contact resistance on device performance.

A study of contact resistance as a function of metal and a function of a-BC:H doping has not been performed previously. The process was developed to determine contact resistance of various metals with a-BC:H and resistivity of a-BC:H.

2.4.1 Ohmic and Schottky contacts

The development of any semiconductor device requires understanding of the metal-semiconductor contact behavior, especially devices that utilize semiconductors with larger resistivity like boron carbide. In theory, metal-semiconductor contacts for device fabrication should be ideal with no resistance or losses at the boundary between metal and the semiconductor, so electrons can freely move across that contact. However, in practice, a junction exists at the contact boundary.

The metal-semiconductor devices that exhibit nonlinear V-I characteristics in the forward and reverse bias region are referred to as the Schottky barrier devices and are used as rectifying devices [28,51,52]. When the metal-semiconductor contact exhibits linear or quasilinear current-voltage characteristics they are referred to as ohmic contact devices (Figure 44).

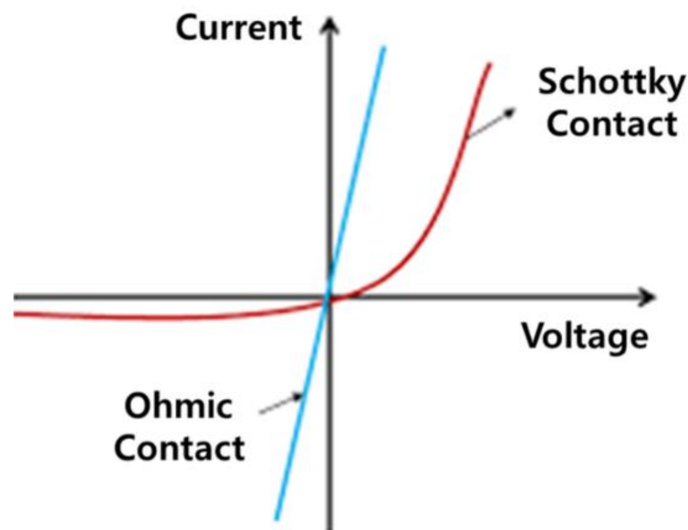

Figure 44 Schottky vs Ohmic contact V-I characteristics

The actual V-I characteristics of the ohmic contact does not have to necessarily be linear, but it must produce a voltage drop across the boundary that is much smaller than

the voltage drop in the active region. That additional resistance at the boundary can be imagined as a resistor in series with the ideal contact [51,52]. This signifies a contact that can supply required current to the device that is necessary for normal operation.

The contact between the metal and the semiconductor is dependent on the metal work function ϕ_M, semiconductor work function ϕ_S and the type of semiconductor, i.e., doping. The metal work function is a constant value of the specific metal and is the energy from the Fermi level E_F to the vacuum level E_0 (minimum energy the electron must possess to free itself from the material). The semiconductor work function is dependent on the electron affinity χ and the difference between the conduction band energy and the Fermi energy level as shown in Equation 6 [28].

Equation 6: $\phi_S = \chi + (E_C - E_F)$

When the metal and semiconductor form a contact the metal work function and electron affinity of the semiconductor are unchanged by the formation of the contact and remain constant. The Fermi energies of the metal and the semiconductor are not equal at the formation of the contact and under equilibrium Fermi level needs to be independent of the position. For the Fermi energy levels to align, transfer of electron occurs from the semiconductor to the metal or vice-versa depending on the work function differences, causing band bending and the formation of the potential energy band barrier that electrons encounter in case of the Schottky contact and no barrier in case of Ohmic contact formation. Figure 45 shows the energy alignment and formation of the barrier for the metal and n-type semiconductor contact for the case of $\phi_M > \phi_S$ and band alignment without the potential barrier when $\phi_M < \phi_S$ where the potential barrier is the difference between metal work function and the semiconductor electron affinity $\phi_B = \phi_M - \chi$ [28].

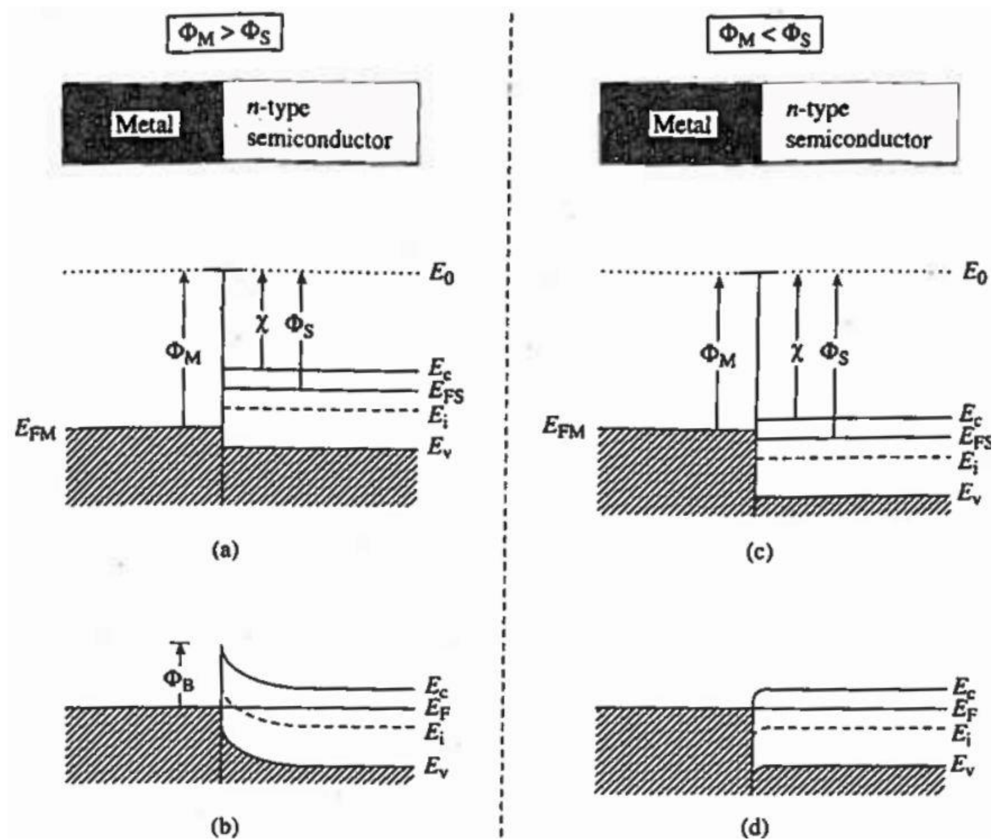

Figure 45 Energy band diagrams for metal-semiconductor contact an instant after the contact is formed (a) and (b) and under equilibrium conditions (c) and (d)

Metal-semiconductor contacts can be defined based on the difference between metal and semiconductor work functions depending on the type of semiconductor (Table 5).

Table 5 Electrical nature of metal-semiconductor contacts

Work function relationship	n-type semiconductor	p-type semiconductor
$\phi_M > \phi_S$	rectifying	ohmic
$\phi_M < \phi_S$	ohmic	rectifying

However, the first principle theoretical prediction of contact type (Table 5) is generally inaccurate as a result of interface states/defects at the metal-semiconductor boundary. Therefore, contact type/resistance is experimentally determined.

2.4.2 Contact resistance measurement – transfer length method

The transfer length method or transmission line method (TLM) is a technique used for obtaining contact resistance through experimental measurements and calculation at the metal-semiconductor boundary, as well as calculating the resistivity of the semiconductor.

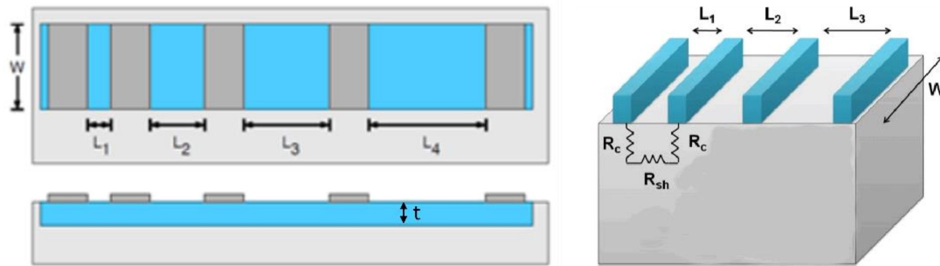

Figure 46 Metal contact bars with varying separation length on a semiconductor

The transfer length method is performed by depositing metal contact bars with varying separation lengths L in the micrometer range, on a single semiconductor film of width W and thickness t, as shown in Figure 46. The transfer length method can be utilized for the ohmic metal-semiconductor contacts as it is dependent on the linear relationship between total resistance of the metal-semiconductor-metal structure and the separation length of the contacts. The total resistance between two metal contacts can be modeled as three resistors in series, as the current flowing through the structure in Figure 46 (right) is passing through two metal-semiconductor contacts and the semiconductor between the contacts, which has a known sheet resistance. In the Equation 7 total resistance as a function of separation length L is shown, where ρ_S is the resistivity of the semiconductor, R_C is the contact resistance, and A is the area of the metal that is in contact with the semiconductor. The contact resistance is expressed in units of Ωcm^2.

Equation 7: $R_T = R_{semi} + \frac{2R_C}{A} = \rho_S \frac{L}{tW} + \frac{2R_C}{A}$

The total resistance is measured between multiple metal contacts separated by at least three different separation lengths L, in a descending or ascending order, and plotted as a function of the separation length. Extrapolating the linear approximation of the total resistance to the point where separation length approaches zero, the semiconductor resistance R_{semi} term in Equation 7 approaches zero and total resistance becomes equal to twice the contact resistance term over the area of the contact.

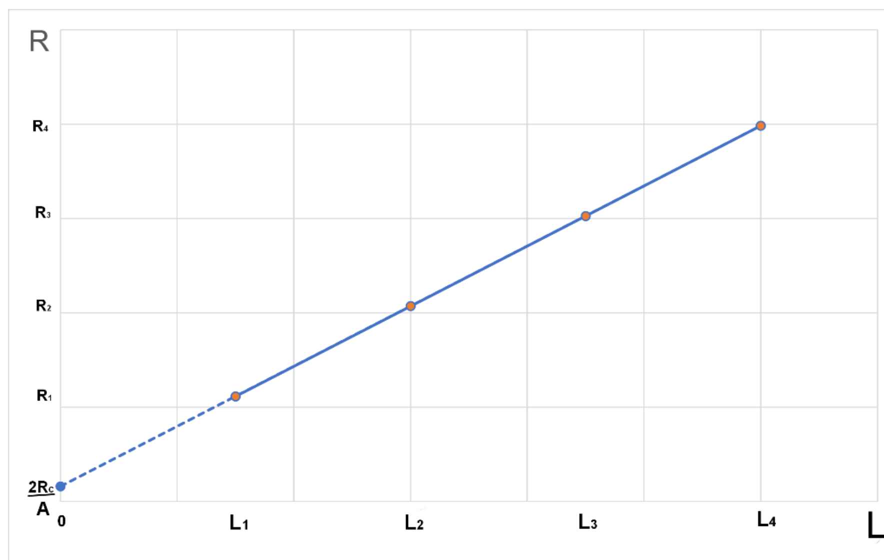

Figure 47 Example graph for total resistance (R) as a function of separation length (L)

Once the contact resistance is obtained, Equation 7 can be solved for resistivity of the semiconductor shown in Equation 8, where L can be chosen from any of the total resistance measurements. Solving for resistivity using every separation length should produce approximately identical results.

Equation 8: $\rho_S = \frac{tW\left(R_T - \frac{2R_C}{A}\right)}{L}$

The transfer length method is a very powerful technique for understanding metal-semiconductor contacts, and it has been widely used in various research to understand losses that can occur at the metal-semiconductor interface [51-53].

However, for the transfer length method to successfully obtain accurate contact resistance values, the resistivity of the semiconductor cannot be so large such that the semiconductor resistance between the contacts obscures the contact resistance (see Equation 7). For highly doped single crystal silicon with resistivity in the range of 0.01-3Ωcm, sheet resistance will be in the single digit Ohms range, allowing for the effect of contact resistance to be calculated accurately. For highly resistive materials such as a-BC:H where resistivities are in 10kΩcm range, the transfer length method is not viable, as the resistance of the a-BC:H would be much higher than the contact resistance term in Equation 7, removing any sensitivity to the contribution of the contact resistance towards the total resistance measurements.

An example of the calculation of relative resistance of the semiconductor and the contacts if it is assumed that the thickness of the semiconductor film is 300nm, width of the contact bars 2cm and resistivity of the a-BC:H film is 1×10^{6} Ωcm, with the separation length of 1μm, is shown in Equation 9.

Equation 9: $$R_T = 10^6 \Omega cm \times \frac{1\times10^{-4} cm}{3\times10^{-5} cm \times 2cm} + \frac{2R_c}{A} = \mathbf{1.67 \times 10^6} \Omega + \frac{2R_c}{A}$$

The semiconductor resistance term dominates the total resistance measured value as it is much larger than the contact resistance. This renders the transfer length method ineffective even for a-BC:H resistivities in the range of 10^{4} Ωcm.

2.4.3 Contact resistance measurement – spreading resistance model

As previously discussed, the transfer length method is ineffective for obtaining contact resistance when high resistivity semiconductors are investigated. The alternate method for contact resistance and resistivity calculation is utilizing the spreading resistance approximation model for a round metal contact on a semiconductor [54].

Figure 48 Metal-semiconductor contact structure for spreading resistance model, top view (left), cross section view (right)

When a round metal contact of radius ***a*** is deposited on semiconductor film of thickness ***b*** as shown in Figure 48, the spreading resistance can be simplified if the radius of the metal contact area is much bigger than the thickness of the semiconductor film. As the thickness of the a-BC:H films are in the range of 100-500nm and the radius of the round metal contact area from 1-2mm, the spreading resistance through the semiconductor film becomes linearly dependent on film thickness [54], shown in Equation 10.

Equation 10: $R_S = \rho_S \frac{b}{\pi a^2}$

b – film thickness, a – contact radius, ρ_s – resistivity of a-BC:H

Comparable to the transfer length method, the total resistance between two contacts of the structure in Figure 49 can be modeled as the sum of the semiconductor

resistance or spreading resistance expressed in Equation 10, and the two contact resistance terms divided by the area of the contact (Equation 11).

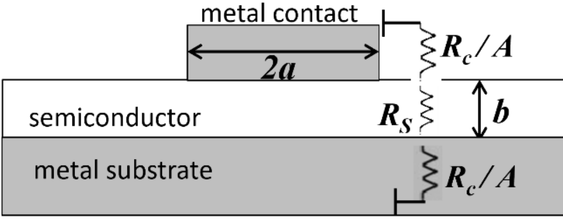

Figure 49 Metal-semiconductor structure for spreading resistance model

Equation 11: $R_T = R_S + \frac{2R_C}{A} = \rho_S \frac{b}{\pi a^2} + \frac{2R_C}{A}$

As total resistance is linearly dependent on the semiconductor film thickness ***b***, to obtain contact resistance of the metal-semiconductor contact multiple films of varying thicknesses are fabricated and total resistance calculated from the V-I characteristic measurements of each structure.

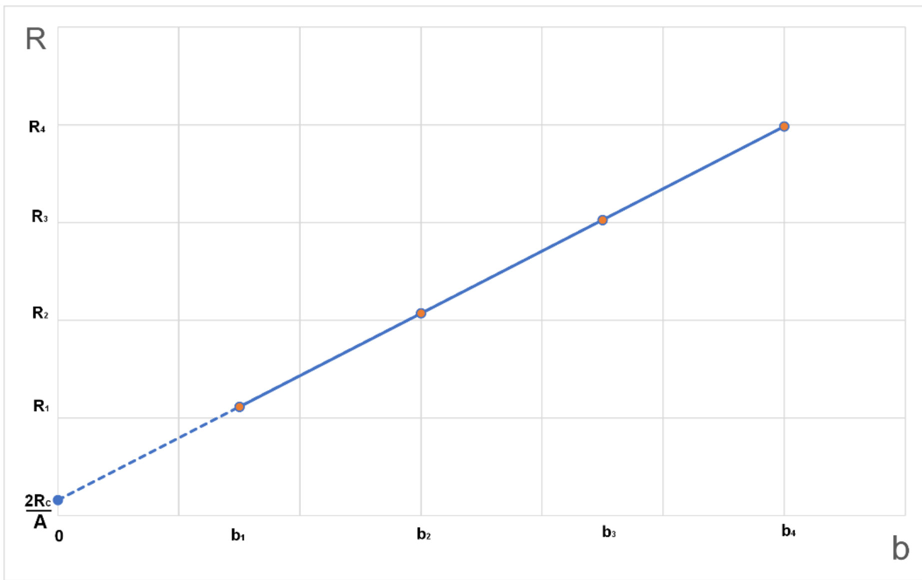

Figure 50 Example graph for total resistance as a function of semiconductor film thickness

The total resistance is plotted as the function of semiconductor film thickness and the linear approximation of the total resistance is extrapolated to the point where film thickness approaches zero, the spreading resistance R_S term in Equation 11 approaches zero and total resistance becomes equal to twice the contact resistance term over area of the contact, shown in Figure 50.

Once the contact resistance is obtained, Equation 11 can be solved for resistivity of the semiconductor as shown in Equation 12, where any film thickness $\boldsymbol{b}$ can be chosen from any of the total resistance measurements. Solving for resistivity using every film thickness should produce approximately identical results.

Equation 12: $\rho_S = \frac{\pi a^2\left(R_T - \frac{2R_C}{A}\right)}{b}$

As previously discussed, the transfer length method is limited when examining semiconductors with high resistivity. However, the spreading resistance model utilized the same approach as the transfer length method but instead of depositing contacts with varying separation lengths in the micrometer range that result in high semiconductor resistances, the total resistance is modeled as a function of film thickness that can be deposited in orders of magnitude less than the separation length in the TLM. Additionally, spreading resistance model examines contact resistance in the direction of the device current flow, which is significant in cases where there is a directional resistivity difference between horizontal and vertical current flow in the device.

To illustrate the difference between the TLM and the spreading resistance model calculations, Equation 13 shows the example for a semiconductor film with high resistivity. If thickness of the semiconductor film is 300nm, radius of the round metal

contact is 1mm and resistivity of the a-BC:H film is 1x10^6 Ωcm, the semiconductor resistance term is orders of magnitude less than the same resistance term in Equation 9.

Equation 13: $R_T = 10^6 \Omega cm \times \frac{300\times10^{-7} cm}{\pi\times(0.1cm)^2} + \frac{2R_c}{A} = \mathbf{955.41}\, \Omega + \frac{2R_c}{A}$

Compared to the TLM, the spreading resistance model is suited for investigating contact resistance and resistivity of semiconductors with high resistivity because the semiconductor resistance term that contributes to the total resistance of the metal-semiconductor-metal structure is orders of magnitude smaller than the same term in the TLM. This results in the ability of the spreading resistance model that is linearly dependent on the semiconductor film thickness to be sensitive to the contact resistance contribution. As boron carbide is considered a highly resistive semiconductor film, the spreading resistance model has been used to investigate contact resistance of metals reported in literature as device contacts by depositing a-BC:H films of various thickness forming a structure illustrated in Figure 49.

2.4.4 Fabrication of metal/a-BC:H spreading resistance structures

To investigate contact resistance at the metal/a-BC:H boundary, the previously discussed spreading resistance model [54] is used to extrapolate contact resistance and calculate resistivity of BC from V-I characteristic measurements of the structure illustrated in Figure 49.

To investigate various metal contacts, a-BC:H films from either ortho-carborane or meta-carborane were grown on metal substrates via PECVD process discussed in section 2.1.3. The bottom and top contacts were deposited via DC magnetron sputtering processes previously discussed. The deposition procedure steps for forming the metal/a-BC:H/metal structures are illustrated in Figure 51.

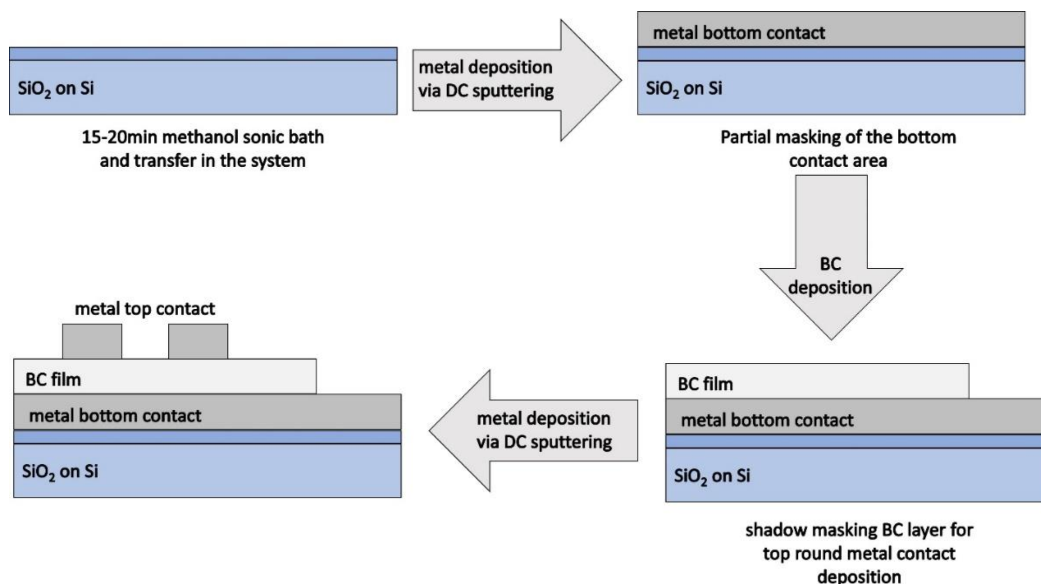

Figure 51 Procedure for metal/a-BC:H/metal structure fabrication

Although the order of the deposition is illustrated to show the procedure, the metal and a-BC:H film thicknesses relative to each other are not shown to scale. As previously discussed, the top metal contact area is much larger than the a-BC:H film thickness for the spreading resistance model to be utilized correctly. The metal top

contact is illustrated as two contacts deposited on the a-BC:H films, but as the top view illustration in Figure 52 shows, there are four such round contacts on the actual film. The shadow mask used to deposit top metal contact is made to produce four as identical as possible metal dot contacts of same diameter and same distance from each dot to test reproducibility of the metal/a-BC:H contacts as well produce multiple V-I characteristic measurements for error testing. Figure 52 shows the top view of the metal/a-BC:H/metal structure in its final form. For consistency, repeatability of measurements and data collection, metal contact dots were always numbered in a manner presented in Figure 52.

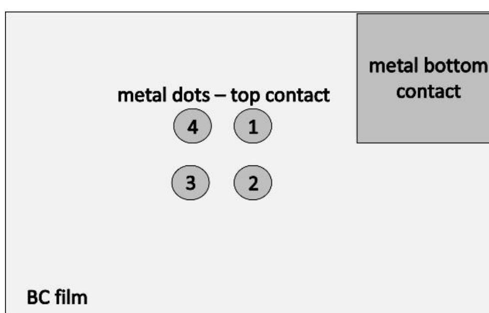

Figure 52 Top view of the metal/a-BC:H/metal structure

2.5 Device characterization

2.5.1 V-I characterization

When the completed devices are fabricated their behavior under bias is characterized by collecting the current output of the device over a voltage range. This is done by the 4-wire resistance measurement method using a Keithley series 2400 source meter (Figure 53) [55].

Figure 53 Keithley 2400 series source meter

The connections illustrations for a source voltage sweep measurement and the internal circuit schematic of the source meter are shown in Figure 54 and 55.

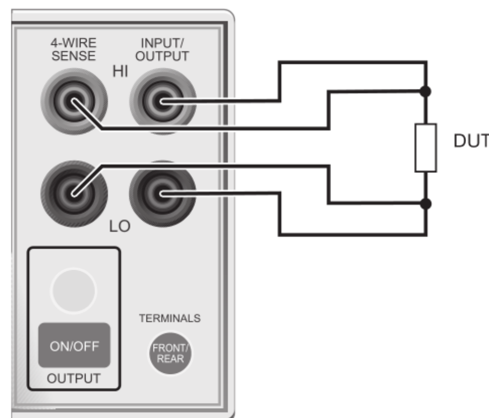

Figure 54 4-Wire connections on the Keithley 2400 source meter

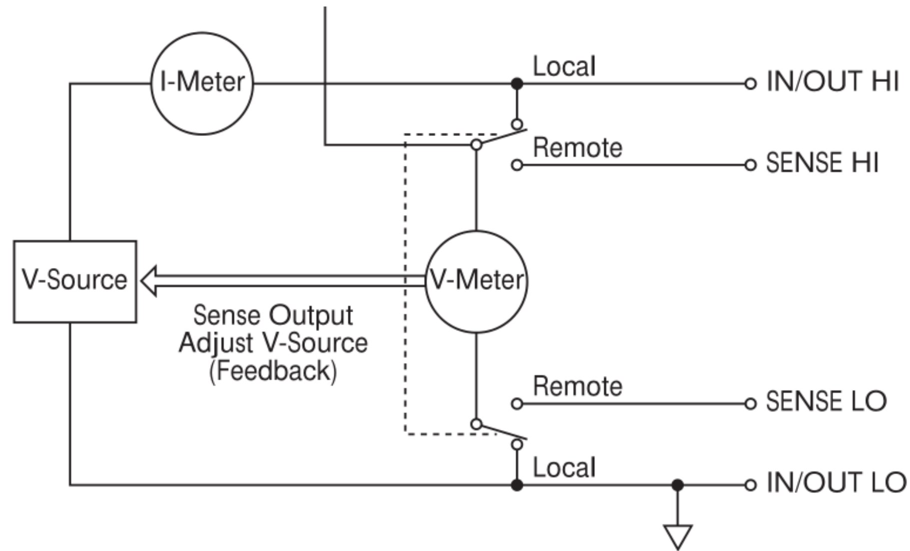

Figure 55 Internal circuitry schematic of the 4-wire connection

For device testing the HI and LO leads are connected at each end of the device as illustrated in Figure 54. For easier connection to the, device the probe station in Figure 56 is used where pins are making contact to the bottom and top metal contacts of the device illustrated in Figure 52.

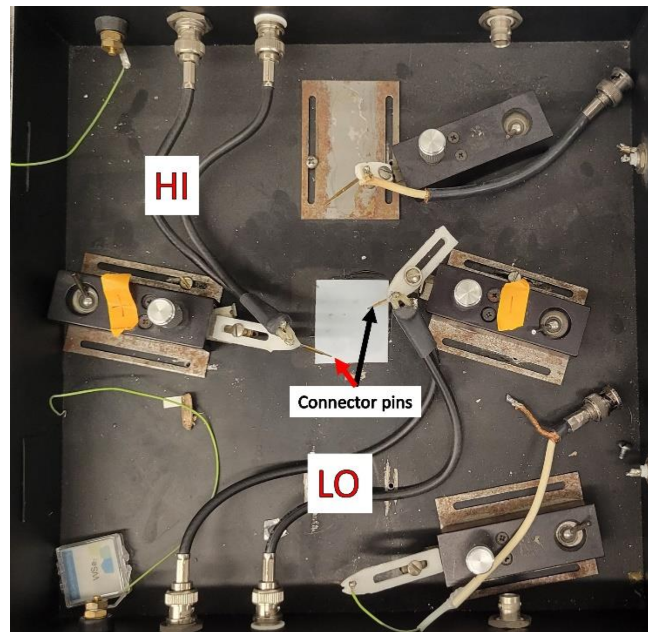

Figure 56 4-Wire measreument probe station

To collect the V-I characteristics of the devices, voltage sweeps and data collection is completed via a computer using the Keithley LabTracer software. The resulting V-I curves provide immediate insight into the behavior of the device.

A commercially available silicon diode was used to test the accuracy of the 4-Wire measurements, with its V-I characteristic shown in Figure 57. The silicon diode V-I curve results are as expected, with the exponential extrapolation R^2 value of 0.9975 and the turn-on voltage at 0.7V which is typical of a silicon diode, where the turn-on voltage refers to the required applied voltage across the diode for the current to be conducted in the forward direction. The turn-on voltage can be obtained from the V-I characteristic curve by linear extrapolation as seen in Figure 57. Additionally, by testing the diode, polarity of the probes was designated as shown in Figure 56, which is important to note when biasing p-n junction devices.

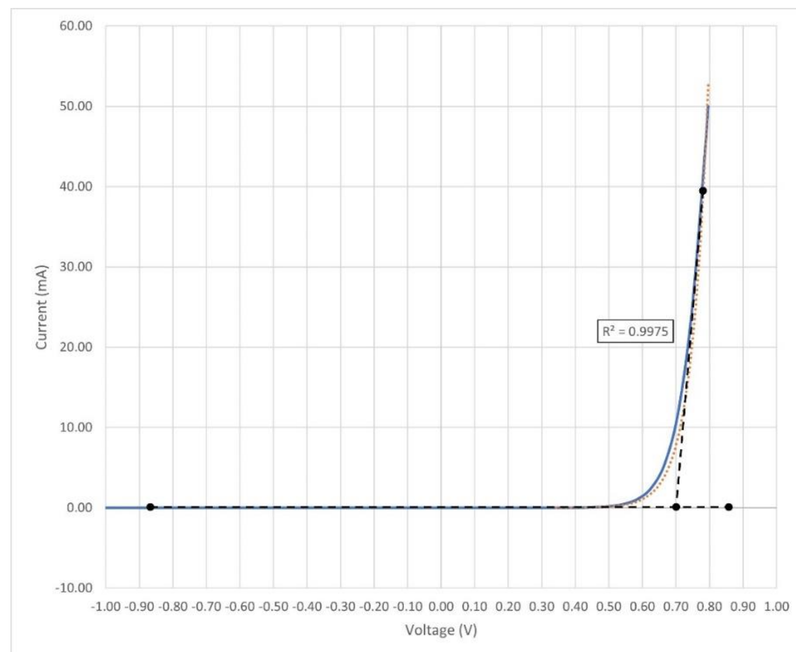

Figure 57 The V-I characteristic of a commercially available silicon diode

2.5.2 X-Ray Photoelectron Spectroscopy (XPS)

Characterization via X-Ray Photoelectron Spectroscopy (XPS) is crucial to understand a-BC:H film growth and device structure formation. As a spectroscopic characterization method, it utilizes the photoelectric effect for detection of all elements (except hydrogen and helium), and bonding state information with depths in the nanometer region [56]. In XPS, samples are irradiated by photons of characteristic energy that interact with core electrons of atoms in the sample. This results in ionized states that are created and a photoelectron that is emitted with the kinetic energy of the difference between the incident photon energy and the core electron binding energy (Equation 14) [56,57].

Equation 14: $E_e = \hbar\omega - E_B$

The measured spectrum of the released photoelectron is a direct measure of the binding energies at different atomic electron levels, and the higher the binding energy the lower the kinetic energy of the emitted photoelectron, generally expressed in electron-volts (eV) [56].

The XPS characterization is performed in an ultra-high vacuum system that is comprised of an X-Ray source, electron energy analyzer with a detector, an auxiliary ion gun, and an x-y-z sample rotation stage [56]. The ultra-high vacuum is considered in the range of $1x10^{-10}$ Torr and is achieved using a combination of mechanical and turbomolecular pumps previously discussed in section 2.1.2. The X-Ray sources commonly used have either Mg or Al anodes and produce energies of 1253.6eV and 1486.6eV respectively, because they possess high enough energies to excite core level electrons but sufficiently low line width below 1eV to produce XPS spectra with

desirable resolution [56]. As XPS is a surface characterization technique, the ion gun in the XPS systems has a crucial role for surface cleaning and depth profiling of samples. This is important in order to understand the bulk sample composition as surface contaminants will affect the XPS spectra. Additionally for layered structures and interface investigations, depth profiling is utilized to perform XPS measurements at vertical points in the film. The ion gun in the XPS generally has 500-3000eV source energy with high current densities on the order of 1mA/cm^2 and is rastered over a wide area of several centimeters [56]. A schematic of a typical XPS system is shown in Figure 58 [56].

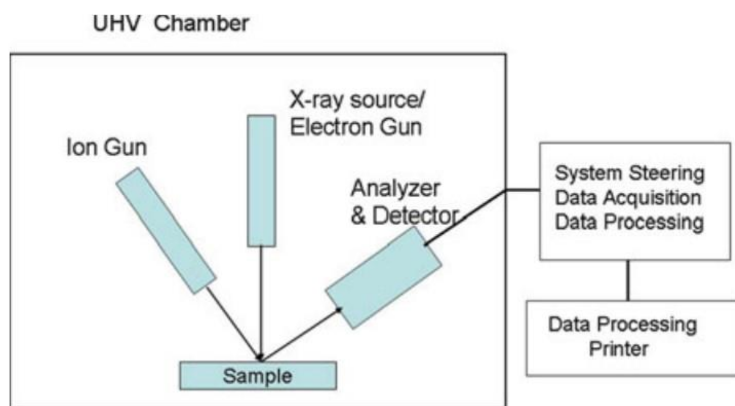

Figure 58 An XPS system schematic

For characterization of a-BC:H and the various devices fabricated from it, XPS is utilized at different stages of a-BC:H device development due to its versatility including:

1. Optimization of film growth – oxygen presence detection throughout the film by depth profiling; atomic percentage composition of B and C.
2. Interface investigation – oxygen presence at the interface of substrate/a-BC:H.
3. Valence band and conduction band offset calculation from XPS valence band and core level spectra.

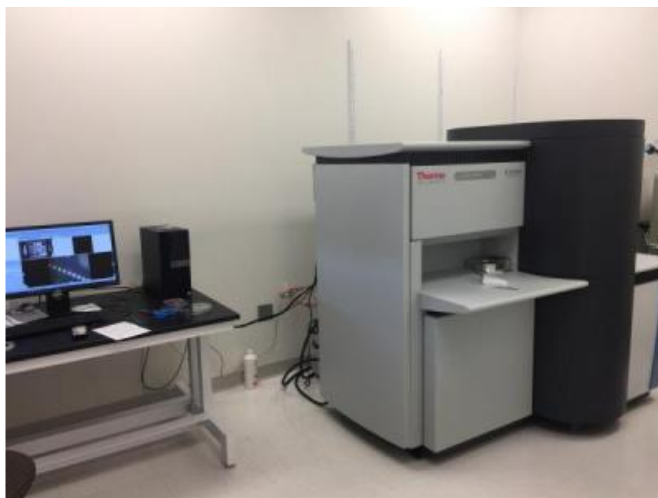

Figure 59 The Thermo-Scientific XPS/UPS system

The system used to characterize the a-BC:H films and devices is the Thermo-Scientific K-alpha+ XPS/UPS System shown in Figure 59. The characterization process is done by performing an XPS survey over an energy spectrum, as well as specifying which elements to individually scan for during the measurement process. For a-BC:H films scans are performed for oxygen, carbon, boron, and whichever material a-BC:H is deposited on (metal, silicon, etc). The parameters for the standard XPS survey scan are shown in Table 6 and example XPS scan spectra shown in Figure 60.

Table 6 XPS survey parameters

Source gun type	Al Kα (1486.6 eV)
Spot size	400 μm
Analyzer mode	CAE: Pass energy 200 eV
Energy step size	1 eV
Number of scans	5

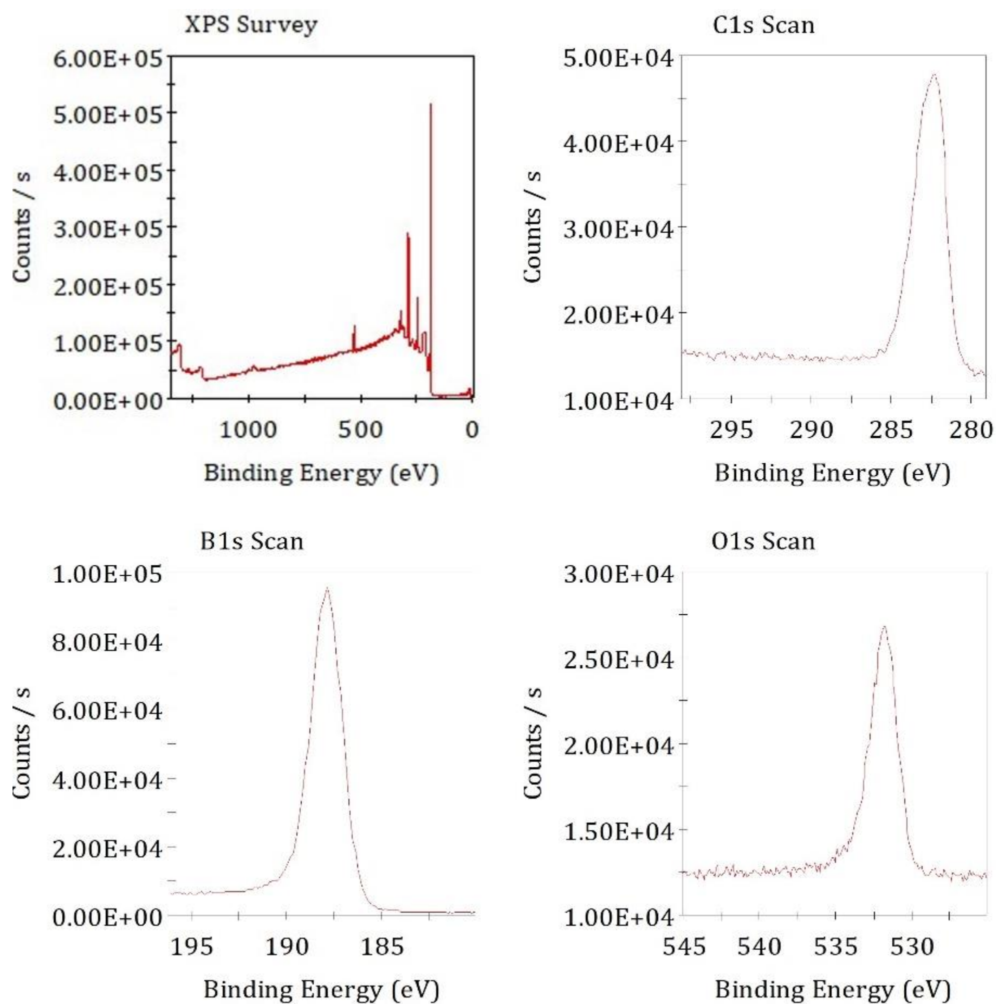

Figure 60 Example XPS survey, and boron, carbon and oxygen scan

As an extremely abrasive resistant and hard material, the depth profiling of a-BC:H requires longer etching time for each analyzed layer than some softer materials, and combined with analyzing each layer it can take hours to sputter through the a-BC:H film to investigate the interface. For an a-BC:H film with the energy of the ion gun at 3000eV and a 90s etch time per layer, the sputter rate averages to approximately 0.0926nm/s. An example XPS depth profile survey is shown in Figure 61.

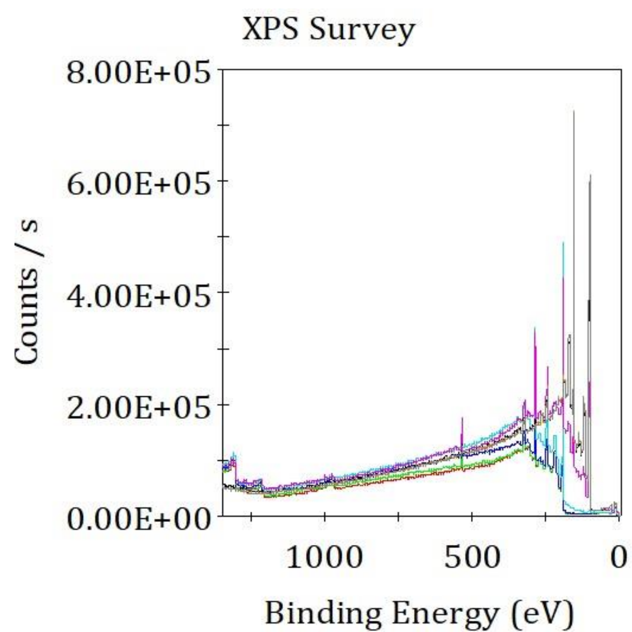

Figure 61 Example depth profile XPS survey

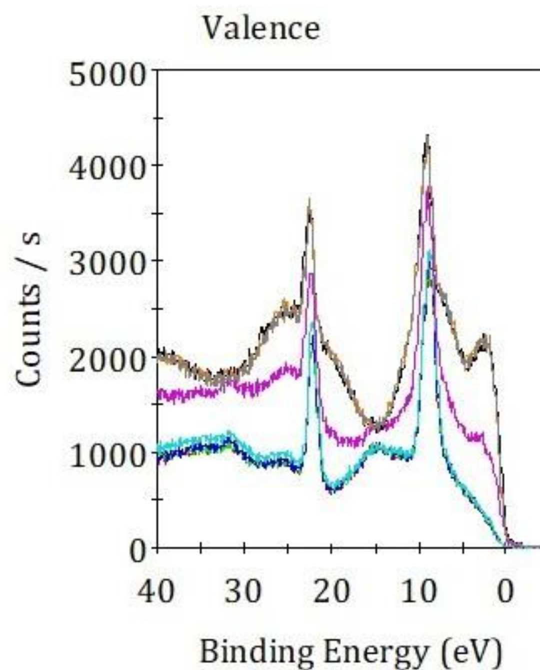

Figure 62 Example XPS valence band scan with depth profile

Additionally, XPS can be used to measure the valence energy spectra (Figure 62) by focusing its scans at the low binding energy range. The resolution for the valence

scans of a-BC:H is increased to 20 scans per layer and 0.05eV energy step, as the increased resolution is necessary to obtain valence band maximums of different bulk layers in the device structure. The valence band along with the core level data of each element can be used to calculate valence and conduction band offsets that will be discussed in the following chapter [58-60]. The versatility of the XPS data acquisition makes it a powerful and paramount tool for understanding metal/ a-BC:H contact structure as well as the devices that will be discussed in the following chapters.

2.5.3 Spectroscopic Ellipsometry

Spectroscopic ellipsometry is a characterization technique used for wide applications in thin-film growth and development process [63]. It was previously mentioned in section 2.1.3 that spectroscopic ellipsometry was used to monitor the growth of a-BC:H films and approximate the deposition rate via PECVD. Ellipsometry works on the principle of quantifying the change in polarized light upon reflection on a sample (or transmission through a sample) [63]. Ellipsometry is generally measured in the ultraviolet and visible light region, quantifying the amplitude ratio "ψ" and phase difference "Δ" between p-polarized and s-polarized light waves. The advantages of ellipsometry for thin-film characterization are that it is a fast, non-destructive technique with high precision of measurements ~0.01nm, and extremely useful for obtaining real-time film thicknesses and optical constants (i.e., bandgap) of a-BC:H films [63]. The disadvantages tend to be tied to the understanding of easily acquired data, as it is an indirect characterization technique that requires an optical model in data analysis that is often complicated [63].

The ellipsometric characterization of a-BC:H is completed using a J.A. Woollam M2000 fixed angle (75º) ellipsometer with the range of incident light of 380-1100nm shown in Figure 63.

Figure 63 M2000 ellipsometer

As it has only a single angle and limited wavelength range, the data of the M2000 ellipsometer is limited compared to a J.A. Woollam RC2 ellipsometer (Figure 64) that performs measurements in the extended wavelength range of 193-2500nm at various incident angles, improving the quality and accuracy of collected data [64]. The initial building of the a-BC:H optical model was done based on the data collected with the RC2 ellipsometer. Once the model is obtained, the M2000 ellipsometer can be used for fast thickness acquisition post deposition.

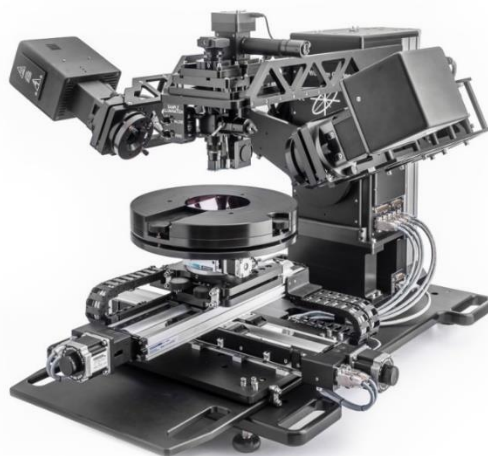

Figure 64 J.A. Woollam RC2 ellipsometer

The thickness is necessary for comparing V-I characteristics between devices of varying thickness; to calculate contact resistance via the spreading resistance model; and XPS depth profile measurements and approximating the sputtering rates and the position of the interface between two layers. The optical constants are necessary for obtaining the bandgap of the n-type and p-type a-BC:H as they are not well known in literature. Therefore, ellipsometry is extremely important to every characterization, measurement, and calculation discussed thus far.

2.6 Summary

The background and experimental procedures of amorphous hydrogenated boron carbide thin-film development, characterization, and device fabrication has been introduced in this chapter. The objective of the following chapters is to introduce a novel amorphous boron carbide-amorphous silicon heterojunction device used for neutron detection. The boron carbide devices made from the polymeric precursors ortho-carborane (p-type) and meta-carborane (n-type) using plasma enhanced chemical vapor deposition (PECVD) showed promising results, but some shortcomings exist. The p-type films made from ortho-carborane have limited doping capability, as p-type a-BC:H type converts to n-type when doped, so a-BC:H devices have reached a performance limit.

The devices made from single crystal p-type silicon and n-type a-BC:H produce devices with higher current density output than the purely boron based devices do. However, single crystal silicon degrades under radiation. Substituting single crystal silicon with a hydrogenated amorphous silicon layer that has comparable work function and is unaffected by neutron radiation can produce desirable device characteristics.

Understanding of metal-semiconductor contacts is important when fabricating p-n devices. Schottky and Ohmic contact in theory can be predicted based on first principles of work functions/band alignment, but in practice the interface states/defects make the first principle predictions inaccurate. As device performance can be affected by the metal/a-BC:H contacts, investigation into contact resistance in the direction of the device is performed with different metals.

2.7 References

[1] Sunwoo Lee, John Mazurowski, G. Ramseyer, P. A. Dowben; Characterization of boron carbide thin films fabricated by plasma enhanced chemical vapor deposition from boranes. *Journal of Applied Physics* 15 November 1992; 72 (10): 4925–4933. https://doi.org/10.1063/1.352060

[2] Ali O. Sezer, J.I. Brand, Chemical vapor deposition of boron carbide, Materials Science and Engineering: B, Volume 79, Issue 3, 2001, Pages 191-202, ISSN 0921-5107, https://doi.org/10.1016/S0921-5107(00)00538-9

[3] Mirzokarimov, Mirzojamshed. Boron carbide hetero-isomeric device fabrication by PECVD from isomeric precursor ortho-carborane and meta-carborane. MS Thesis. University of Nebraska, 2019

[4] Seong-Don Hwang, Dongjin Byun, N. J. Ianno, P. A. Dowben, H. R. Kim; Fabrication of boron-carbide/boron heterojunction devices. Appl. Phys. Lett. 11 March 1996; 68 (11): 1495–1497. https://doi.org/10.1063/1.116266

[5] Hong, Nina, "An Exploration of Neutron Detection in Semiconducting Boron Carbide" (2012). *ETD collection for University of Nebraska - Lincoln*. AAI3503993. https://digitalcommons.unl.edu/dissertations/AAI3503993

[6] Peterson, George Glen, "Electrical Characterization of Irradiated Semiconducting Amorphous Hydrogenated Boron Carbide" (2017). Mechanical (and Materials) Engineering -- Dissertations, Theses, and Student Research. 124. http://digitalcommons.unl.edu/mechengdiss/124

[7] Caruso, A. & Billa, Ravi & Balaz, Snjezana & Brand, J. I. & Dowben, Peter, The heteroisomeric diode. Journal of Physics Condensed Matter. 16. L139-L146. (2004), https://doi.org/10.1088/0953-8984/16/10/L04.

[8] A.N. Caruso, The physics of solid-state neutron detector materials and geometries, J. *Phys.: Condens. Matter* **22** 443201, 2010, https://doi.org/10.1088/0953-8984/22/44/443201

[9] Caruso, A. & Bernard, Laetitia & Xu, Bo & Dowben, Peter. (2003). Comparison of Adsorbed Orthocarborane and Metacarborane on Metal Surfaces. Journal of Physical Chemistry B. 107. 9620-9623. https://doi.org/10.1021/jp0354088

[10] Oliva, Josep & Serrano-Andrés, Luis & Klein, Douglas & Schleyer, Paul & Michl, Josef. (2009). Design of Carborane Molecular Architectures via Electronic Structure Computations. International Journal of Photoenergy. 2009. https://doi.org/10.1155/2009/292393.

[11] D.N. McIlroy, Jiandi Zhang, P.A. Dowben, P. Xu, D. Heskett, The coadsorption of metals and molecular icosahedra on Cu(100), Surface Science, Volume 328, Issues 1–2, 1995, Pages 47-57, ISSN 0039-6028, https://doi.org/10.1016/0039-6028(95)00040-2

[12] D. Tsifakis, C. Charles, R. Boswell, An Inductively-Coupled Plasma Electrothermal Radiofrequency Thruster, Frontiers in Physics vol. 8, 2020, https://doi.org/10.3389/fphy.2020.00034

[13] Lieberman MA, Lichtenberg AJ. Principles of Plasma Discharges and Materials Processing. 2nd ed. Hoboken, NJ: Wiley (2005), https://doi.org/10.1002/0471724254

[14] F.F. Chen, J.P. Chang, Lecture Notes on Principles of Plasma Processing, Plenum/Kluwer Publishers, 2002

[15] B. Chapman, Chapter 5 - Glow Discharge Processes: Sputtering and Plasma Etching, New York: Wiley, 1980, ISBN: 978-0-471-07828-9

[16] Appendix B – Bias Enhanced Nucleation, University of Bristol, School of Chemistry, https://www.chm.bris.ac.uk/pt/diamond/stuthesis/appendb.htm

[17] Milton Ohring, Chapter 6 - Vacuum Science and Technology, Editor(s): Milton Ohring, Materials Science of Thin Films (Second Edition), Academic Press, 2002, Pages 277-355, ISBN 9780125249751, https://doi.org/10.1016/B978-012524975-1/50009-4

[18] Milton Ohring, Chapter 2 - Vacuum Science and Technology, Editor(s): Milton Ohring, Materials Science of Thin Films (Second Edition), Academic Press, 2002, Pages 57-93, ISBN 9780125249751, https://doi.org/10.1016/B978-012524975-1/50005-7.

[19] B. Chapman, Chapter 1 - Glow Discharge Processes: Sputtering and Plasma Etching, New York: Wiley, 1980, ISBN: 978-0-471-07828-9

[20] Humaira Ghazal and Nadeem Sohail, Chapter 2 Sputtering Deposition – Thin Films, Editor(s): Dongfang Yang, Rijeka, 2022, https://doi.org/10.5772/intechopen.107353

[21] Matt Hughes, What is DC Sputtering, SEMICORE, 2016, https://www.semicore.com/news/94-what-is-dc-sputtering

[22] David Emin and T. L. Aselage, A proposed boron-carbide-based solid-state neutron detector, J. Appl. Phys. 97, 013529 (2005); https://doi.org/10.1063/1.1823579

[23] A.N. Caruso, P. Dowben, et al, The all-boron carbide diode neutron detector: Comparison with theory, Materials Science and Engineering: B. 135. 129-133, 2006, http://doi.org/10.1016/j.mseb.2006.08.049

[24] K. Osberg et al., A Handheld Neutron-Detection Sensor System Utilizing a New Class of Boron Carbide Diode, in IEEE Sensors Journal, vol. 6, no. 6, pp. 1531-1538, Dec. 2006, https://doi.org/10.1109/JSEN.2006.883905

[25] Seong-Don Hwang, N. B. Remmes, P. A. Dowben, D. N. McIlroy; Nickel doping of boron carbide grown by plasma enhanced chemical vapor deposition. Journal of Vacuum Science & Technology B: Microelectronics and Nanometer Structures Processing, Measurement, and Phenomena 1 July 1996; 14 (4): 2957–2960. https://doi.org/10.1116/1.588942

[26] P.A. Dowben, Orhan Kizilkaya, Jing Liu, B. Montag, K. Nelson, I. Sabirianov, J.I. Brand, 3d transition metal doping of semiconducting boron carbides, Materials Letters, Volume 63, Issue 1, 2009, Pages 72-74, ISSN 0167-577X, https://doi.org/10.1016/j.matlet.2008.09.004

[27] Carlson, L., LaGraffe, D., Balaz, S. et al. Doping of boron carbides with cobalt, using cobaltocene. Appl. Phys. A **89**, 195–201 (2007). https://doi.org/10.1007/s00339-007-4086-6

[28] McIlroy, D.N.; Hwang, S.-D.; Yang, K.; Remmes, N.; Dowben, Peter A.; Ahmad, A.A.; Ianno, N.J.; Li, J.Z.; and Jiang, H.X., The incorporation of Nickel

and Phosphorus dopants into Boron-Carbon alloy thin films, (1998). Peter Dowben Publications. 105. https://digitalcommons.unl.edu/physicsdowben/105

[29] Douglas S. McGregor, J. Kenneth Shultis, Spectral identification of thin-film-coated and solid-form semiconductor neutron detectors, Nuclear Instruments and Methods in Physics Research Section A: Accelerators, Spectrometers, Detectors and Associated Equipment, Volume 517, Issues 1–3, 2004, Pages 180-188, ISSN 0168-9002, https://doi.org/10.1016/j.nima.2003.09.037

[30] R. F. Pierret, Chapter 6 - Semiconductor Device Fundamentals, 2nd edition, Addison Wesley, 1996, ISBN-10: 0201543931

[31] A. Ruzin, G. Casse, M. Glaser, A. Zanet, F. Lemeilleur and S. Watts, Comparison of radiation damage in silicon induced by proton and neutron irradiation, in IEEE Transactions on Nuclear Science, vol. 46, no. 5, pp. 1310-1313, Oct. 1999, https://doi.org/10.1109/23.795808

[32] G. C. Messenger and J. P. Spratt, The Effects of Neutron Irradiation on Germanium and Silicon, in Proceedings of the IRE, vol. 46, no. 6, pp. 1038-1044, June 1958, https://doi.org/10.1109/JRPROC.1958.286841

[33] Cheng, L. J. and Lori, J., Characteristics of Neutron Damage in Silicon , Phys. Rev 171 3, p. 856-862, 1968, American Physical Society https://doi,org/10.1103/PhysRev.171.856

[34] Yannick Deshayes, Laurent Béchou, 1 - State-of-the-Art of Infrared Technology, Editor(s): Yannick Deshayes, Laurent Béchou, Reliability, Robustness and Failure Mechanisms of LED Devices, Elsevier, 2016, Pages 1-

44, ISBN 9781785481529, https://doi.org/10.1016/B978-1-78548-152-9.50001-8

[35] Brennan, K. (2005). Introduction to Semiconductor Devices: For Computing and Telecommunications Applications. Cambridge: Cambridge University Press. https://doi.org/10.1017/CBO9781139171373

[36] Seong-Don Hwang, Ken Yang, P. A. Dowben, Ahmad A. Ahmad, N. J. Ianno, J. Z. Li, J. Y. Lin, H. X. Jiang, D. N. McIlroy; Fabrication of n-type nickel doped B5C1+δB5C1+δ homojunction and heterojunction diodes. Appl. Phys. Lett. 24 February 1997; 70 (8): 1028–1030. https://doi.org/10.1063/1.118434

[37] F.Rana, "Chapter 2 Semiconductor Heterostructures", Semiconductor optoelectronics, Cornell University

[38] Sze, S. M. (2002). Semiconductor devices: physics and technology / S.M. Sze. (2nd ed.), Wiley, ISBN: 0471333727

[39] Brennan, K. F., & Brown, A. S. (2002). Theory of modern electronic semiconductor devices / Kevin F. Brennan, April S. Brown. John Wiley.

[40] Balaz, S., Dimov, D., Boag, N. *et al.* The electronic structure of 1,2-$PCB_{10}H_{11}$ molecular films: a precursor to a novel semiconductor. Appl. Phys. A **84**, 149–159 (2006). https://doi.org/10.1007/s00339-006-3578-0

[41] Adenwalla, S. & Welsch, P. & Harken, Andrew & Brand, J. I. & Sezer, Ali O. & Robertson, Brian. (2001). Boron carbide/n-silicon carbide heterojunction diodes. Applied Physics Letters – Appl. Phys. Lett. 79, https://doi.org/10.1063/1.1426257

[42] R. C. Chittick et al, The Preparation and Properties of Amorphous Silicon, 1969 J. Electrochem. Soc. 116 77, https://doi.org/10.1149/1.2411779

[43] H. Kang, Crystalline Silicon vs. Amorphous Silicon: the Significance of Structural Differences in Photovoltaic Applications, IOP Conference Series: Earth and Environmental Science, vol. 726, 2021, https://doi.org/10.1088/1755-1315/726/1/012001

[44] Mikolášek, Miroslav & Jakabovič, Ján & Rehacek, Vlastimil & Harmatha, Ladislav & Andok, Robert. (2014). Capacitance Analysis of the Structures with the a-Si:H(i)/c-Si(p) Heterojunction for Solar-Cell Applications. Journal of Electrical Engineering. 65. 254-258. https://doi.org/10.2478/jee-2014-0039.

[45] A. H. Mahan, J. Carapella, B. P. Nelson et al, Deposition of device quality, low H content amorphous silicon, Journal of Applied Physics 69, 6728 (1991); https://doi.org/10.1063/1.348897

[46] N Wyrsch, C Ballif, Review of amorphous silicon based particle detectors: the quest for single particle detection, Semicond. Sci. Technol. 31 (2016) 103005, https://doi.org/10.1088/0268-1242/31/10/103005

[47] M. Despeisse *et al*., Hydrogenated Amorphous Silicon Sensor Deposited on Integrated Circuit for Radiation Detection, in *IEEE Transactions on Nuclear Science*, vol. 55, no. 2, pp. 802-811, April 2008, https://doi/10.1109/TNS.2008.918519

[48] A. Mireshghi et al., Amorphous silicon position sensitive neutron detector, in IEEE Transactions on Nuclear Science, vol. 39, no. 4, pp. 635-640, Aug. 1992, https://doi.org/10.1109/23.159678.

[49] J. R. Srour et al., "Damage mechanisms in radiation-tolerant amorphous silicon solar cells," in IEEE Transactions on Nuclear Science, vol. 45, no. 6, pp. 2624-2631, Dec. 1998, https://doi.org/10.1109/23.736506.

[50] M. Menichelli, M. Bizzarri, M. Boscardin et. al, Neutron irradiation of Hydrogenated Amorphous Silicon p-i-n diodes and charge selective contacts detectors, Nuclear Instruments and Methods in Physics Research Section A: Accelerators, Spectrometers, Detectors and Associated Equipment, Volume 1052, 2023, 168308, ISSN 0168-9002, https://doi.org/10.1016/j.nima.2023.168308

[51] H. H. Berger, Contact resistance and contact resistivity, Journal of The Electrochemical Society, vol. 119, no. 4, p. 507, 1972, https://doi.org/10.1149/1.2404240

[52] D. K. Schroder and D. L. Meier, Solar cell contact resistance—A review, in IEEE Transactions on Electron Devices, vol. 31, no. 5, pp. 637-647, May 1984, https://doi.org/10.1109/T-ED.1984.21583.

[53] K. Matsuzawa, K. Uchida and A. Nishiyama, A unified simulation of Schottky and ohmic contacts, in IEEE Transactions on Electron Devices, vol. 47, no. 1, pp. 103-108, Jan. 2000, https://doi.org/10.1109/16.817574

[54] M.W. Denhoff, An accurate calculation of spreading resistance, 2006 J. Phys. D: Appl. Phys. 39 1761, https://doi.org/10.1088/0022-3727/39/9/009

[55] User Manual – Kethley Series 2400 SourceMeter, 2015, https://download.tek.com/manual/2400S-900-01_K-Sep2011_User.pdf

[56] S. Hofmann, Auger and X-Ray Photoelectron Spectroscopy in Material Science: A User-Oriented Guide, 2013, Volume 49, ISBN : 978-3-642-27380-3, https://doi.org/10.1007/978-3-642-27381-0

[57] T.L. Alford, L.C. Feldman, J.W. Mayer, Fundamentals of Nanoscale Film Analysis, 2007, ISBN : 978-0-387-29260-1, https://doi.org/10.1007/978-0-387-29261-8

[58] E. A. Kraut, R. W. Grant, J. R. Waldrop, and S. P. Kowalczyk, Precise Determination of the Valence-Band Edge in X-Ray Photoemission Spectra, Application to Measurement of Semiconductor Interface Potentials, Phys. Rev. Lett. 44, 1620, 1980, https://doi.org/10.1103/PhysRevLett.44.1620

[59] Sean W. King, Marc French, Guanghai Xu, Benjamin French, Milt Jaehnig, Jeff Bielefeld, Justin Brockman, Markus Kuhn, Valence band offset and Schottky barrier at amorphous boron and boron carbide interfaces with silicon and copper, Applied Surface Science, Volume 285, Part B, 2013, Pages 545-551, ISSN 0169-4332, https://doi.org/10.1016/j.apsusc.2013.08.090

[60] Nina Hong, M. A. Langell, Jing Liu, Orhan Kizilkaya, S. Adenwalla; Ni doping of semiconducting boron carbide. J. Appl. Phys. 15 January 2010; 107 (2): 024513, https://doi.org/10.1063/1.3284205

[61] K.C. Sanal, Rafael Ballinas Morales, Victoria E. Gonzàlez Flores, S. Shaji, P.K. Nair, M.T.S. Nair, Co-sputtered Zn1-xMgxO films and interfacial band offsets at heterojunctions with SnS-CUB, Journal of Alloys and Compounds, Volume 763, 2018, Pages 909-915, ISSN 0925-8388, https://doi.org/10.1016/j.jallcom.2018.05.276.

[62] Kumar, M., Rajpalke, M.K., Roul, B., Bhat, T.N., Kalghatgi, A.T. and Krupanidhi, S.B. (2012), Determination of MBE grown wurtzite GaN/Ge_3N_4/Ge heterojunctions band offset by X-ray photoelectron spectroscopy. Phys. Status Solidi B, 249: 58-61. https://doi.org/10.1002/pssb.201147318

[63] H. Fujiwara, Spectroscopic Ellipsometry: Principles and Applications, 2007, Wiley & Sons Ltd, ISBN:9780470060193, https://doi.org/10.1002/9780470060193

[64] J.A. Woollam, RC2 ellipsometer brochure, https://www.jawoollam.com/download/pdfs/rc2-brochure.pdf

Chapter 3 – Investigation of Metal/a-BC:H Contacts

Metal contacts are an important factor to consider when producing semiconductor devices. The fact that different metals can form either Schottky or Ohmic contacts (section 2.4.1) with a semiconductor has been previously discussed, and how to obtain contact resistance has been introduced through two different measurement methods (sections 2.4.2 and 2.4.3). For a device with highly resistive layers like a-BC:H, ohmic contacts should be identified and optimized to minimize losses at the contact junction to improve device performance.

There have been various metals reported in literature used as a contact on either p-type or n-type BC device layers shown in Table 7 [1-10], and a detailed investigation was done for the interface between metals and the p-type a-BC:H grown from ortho-carborane [11]. However, a detailed investigation of the metal contacts on the n-type a-BC:H grown from meta-carborane has not been performed.

Table 7 Metal contacts on a-BC:H reported in literature

Metal	Boron carbide type	Ref.
Al	p-type (ortho-carborane)	1,2,3,7
Au	p-type (ortho-carborane)	1,4,9,10
Cr	p-type (ortho-carborane), n-type (meta-carborane)	3,6
Ag	p-type (ortho-carborane), n-type (meta-carborane)	3,6
Ni	n-type (meta-carborane)	3
Cu	p-type (ortho-carborane)	5
Ti	n-type (meta-carborane)	
Hf	p-type (ortho-carborane)	

In fact, the characteristics of metal/a-BC:H contacts in previous work has not been discussed as a contributing factor in device performance. For example, Figure 65 from reference [3] shows the alternating combination of contacts for testing different 3d transition metal doping effects on device performance where the effects of the metal/a-BC:H junction was not accounted for [3].

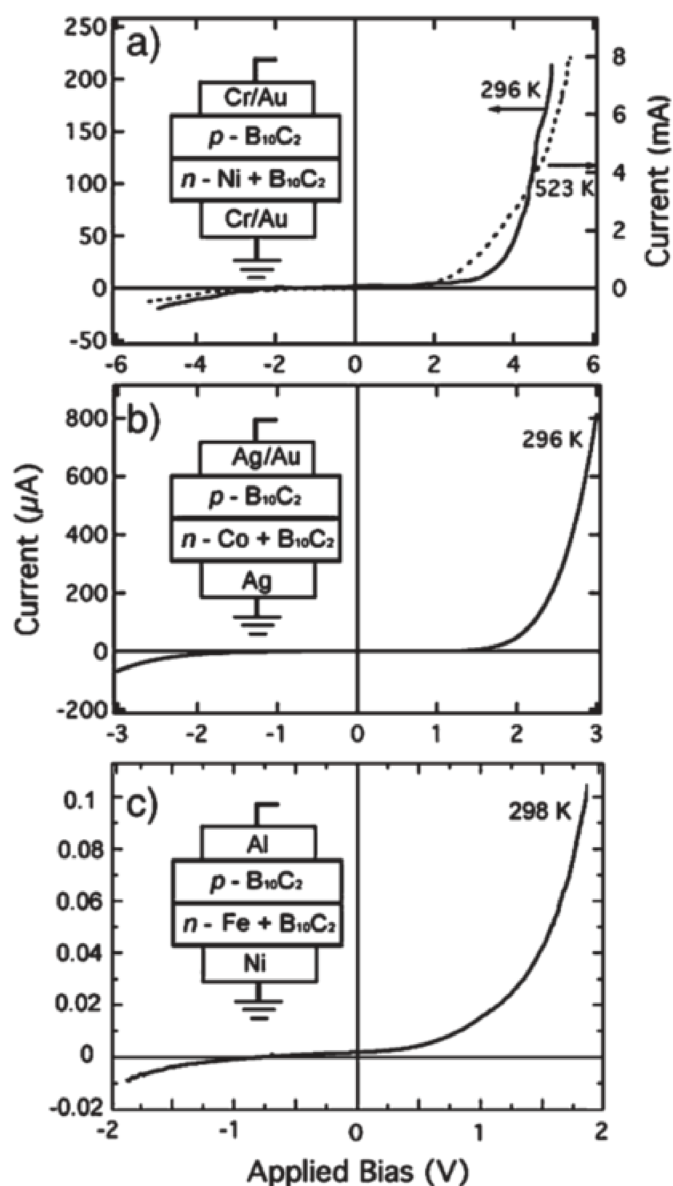

Figure 65 Reported doping investigation that used three different metal contact combinations in device fabrication

Additionally, there have been instances where device structures discussed in the literature do not state the metal used for contacts as shown in Figure 66 [8,9,10]. This makes it difficult to understand the fabrication process and characterization of reported devices for future research.

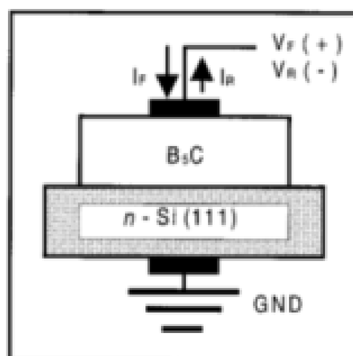

Figure 66 Fabricated device without specified contacts

The two metals that are often used for electrical contacts are gold [1,4,9,10] and silver [3,6] as they are easily sputtered metals with good electrical conductivity. However, when choosing a metal for neutron voltaic device contact, the effect of thermal neutron irradiation must be considered. When gold is irradiated by thermal neutrons, the Au^{198} decays with a half-life of 2.7 days to stable Hg^{198} by emission of beta particles of maximum energy 0.96MeV and gamma energies 0.412MeV, 0.68MeV and 1.09MeV [12]. The metal contacts in neutron voltaic devices should be unaffected by neutron radiation, gold, however good a metal contact it is for other devices, is not a viable long-term candidate for practical neutron detectors. Thermal radiation affects silver differently, when exposed to neutron radiation, it creates unstable Ag^{108} and Ag^{110} isotopes that beta decay [13]. The decay itself is instantaneous and would not be the deterring factor for using Ag as a metal contact, however the release of the high energy electron during beta

decay can cause localized heating and diffusion of Ag into the a-BC:H film which can cause device failure [5].

The metal contacts reported in literature as well contacts that have comparable work functions are presented in Table 8 [15-17]. A detailed investigation of metal/a-BC:H contacts is presented in this chapter. Additionally, contact resistance in the direction of the device current flow and a-BC:H resistivity is determined from contacts that produce an Ohmic junction as bottom and top contacts.

Table 8 Work functions of various metals

Element	**Work function ϕ (eV)**	**Electronegativity**
Al	4.2	1.61
Au	5.47	2.54
Cr	4.5	1.66
Ag	4.64	1.93
Ni	5.22	1.91
Cu	5.1	1.90
Ti	4.33	1.54
Hf	3.9	1.30

The 4-Wire measurements are used to initially characterize the spreading resistance structures discussed in section 2.4.4. There are four possible outcomes for a metal/a-BC:H/metal fabricated structure. The linear low resistance curve is a result of the shorted top and bottom metal contacts. This occurs when there is a fabrication flaw in the a-BC:H film during deposition causing a pinhole through which shorting can occur. Shorting can also occur if the applied voltage of the sweep exceeds the device tolerance. To avoid device shorting, the range of the voltage sweep is initially limited to -5V to 5V or lower. The linear (ohmic) curve of a spreading resistance structure is the V-I characteristic of a metal-semiconductor-metal structure with both junctions exhibiting

Ohmic behavior. If one or both junctions of the spreading resistance structure exhibit Schottky behavior the resulting V-I characteristics have a characteristic of one sided or symmetrical double-sided Schottky characteristic.

The ellipsometric optical model is used to determine the thickness of the a-BC:H in the spreading resistance structure. The optical model for the a-BC:H is developed from the data acquired by the RC2 ellipsometer (section 2.5.3) on the single crystal/a-BC:H structure. The a-BC:H layer is modeled by the Cody-Lorentz oscillator with MSE of 33.226 for the wavelength range of 350-1690nm and is shown in Figure 67.

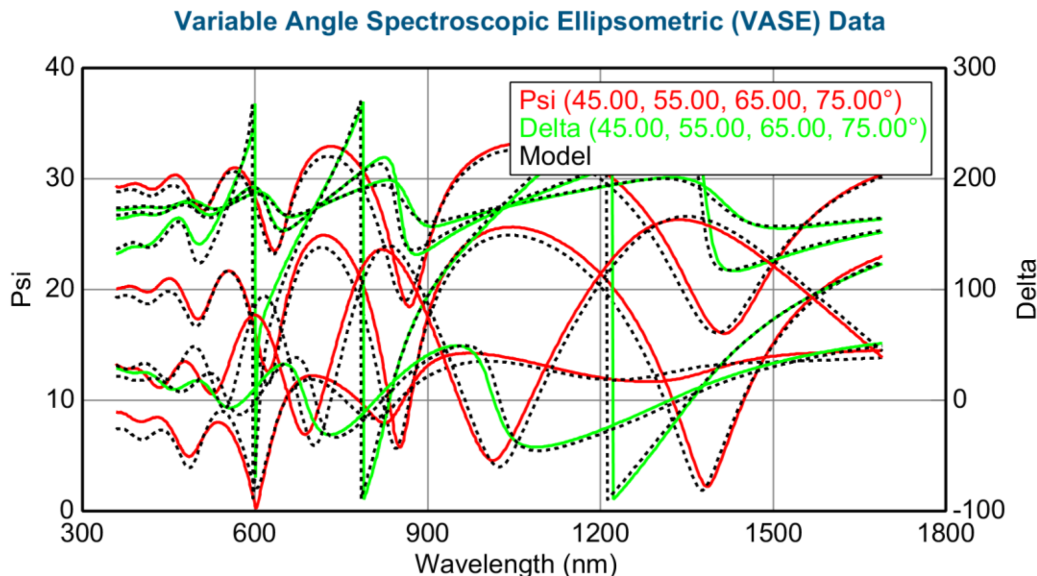

Figure 67 c-Si/a-BC:H optical model fit of the RC2 data

The optical model of the a-BC:H constructed on the data obtained by the RC2 can be used to model the data obtained using a fixed angle M2000 ellipsometer. The a-BC:H layer of the model can be saved and used to model different structures. The graph of the optical constants is shown in Figure 68.

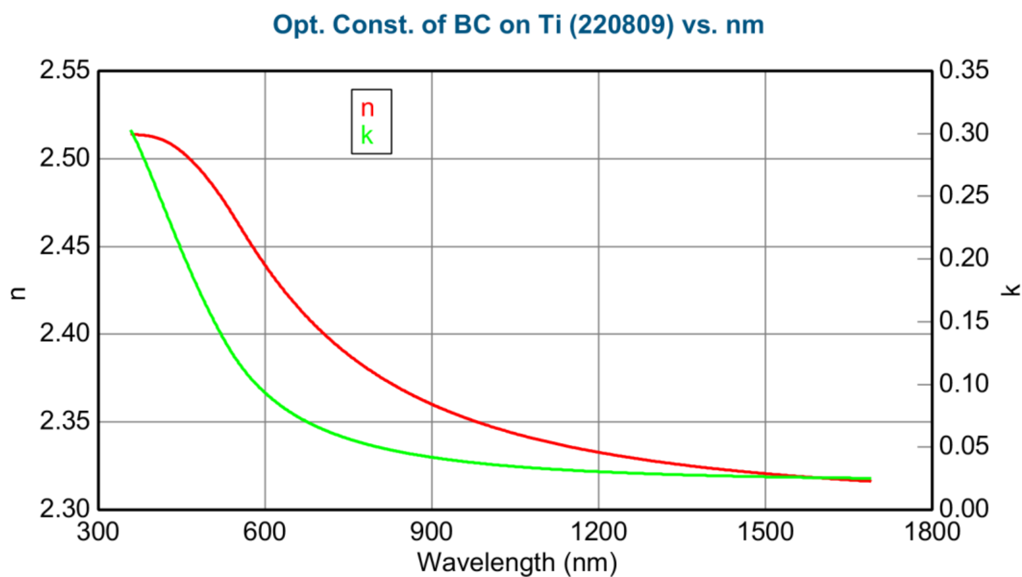

Figure 68 Optical constants for a-BC:H film

Collecting the V-I characteristics of the spreading resistance structures with the 4-Wire measurements and thickness with the ellipsometer, contact resistance investigation can be carried out. The following sections present results collected for different metal/a-BC:H structures.

3.1 Titanium as the metal contact

The p-type a-BC:H made from ortho-carborane has shown limitations when doped with 3d transition metals [3,6,9,10], specifically a-BC:H films grown from ortho-carborane type-convert when doped. However, the n-type a-BC:H films grown from meta-carborane do not type-convert but become more n-type, having a higher potential for producing quality p-n heterojunction devices with a-Si:H. Therefore, finding a metal that forms an Ohmic contact with n-type a-BC:H is important. Even though titanium has not been reported in literature to be used as a contact on n-type a-BC:H deposited from meta-carborane, it was investigated as a substitute for silver whose limitations were previously discussed, because of its comparable work function and electronegativity to various metals reported in literature (Table 8). Four different structures as shown in Figure 69 were fabricated with varying a-BC:H film thicknesses.

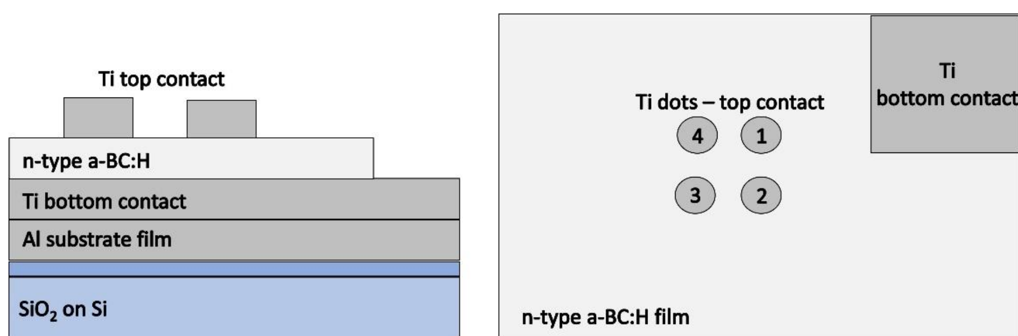

Figure 69 Ti contact spreading resistance structure

It can be noted from Figure 69 that an Al film was used as a substrate layer for the Ti bottom contact. The resistivity of Ti ($4.2\text{x}10^{-7}$ Ωcm) is larger than most metals in Table 8 (e.g., Al has $2.82\text{x}10^{-8}$ Ωcm), a Ti thin film over multiple centimeters has noticeable resistance that would affect contact resistance measurements. To avoid this, an Al film is deposited as a substrate layer before the Ti film is deposited that serves as a

bottom contact for a-BC:H. This structure configuration produces an effective short over the substrate area.

The V-I characteristics of the four different structures exhibited Ohmic behavior and are shown in Figure 70. The total resistance of each structure was calculated from the Ohm's Law at each data point and averaged over the entire dataset producing the averaged total resistance values shown in Figure 70 and in Table 9.

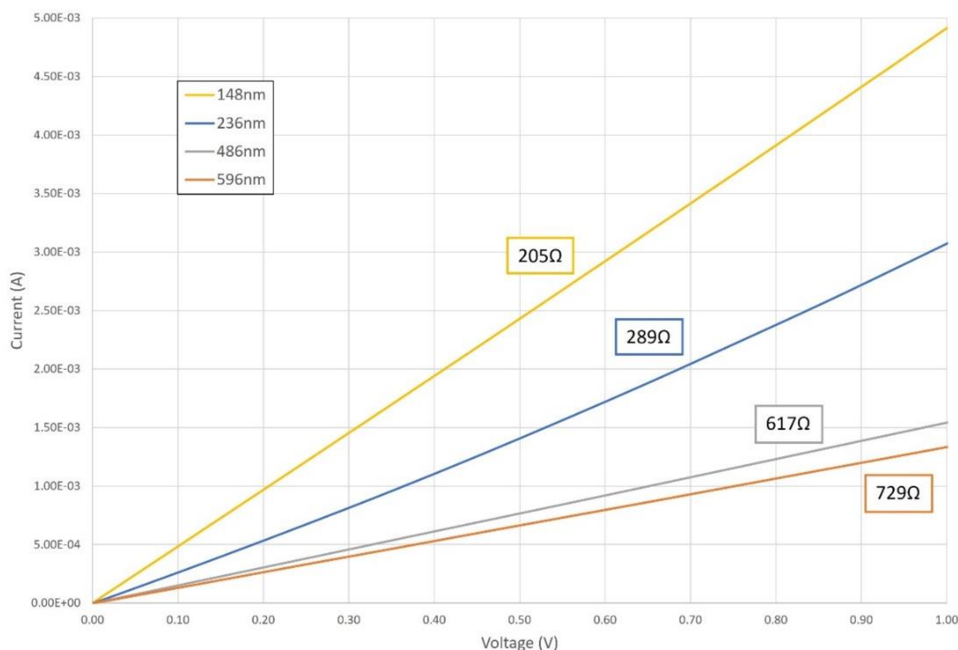

Figure 70 V-I characteristics of Ti/a-BC:H/Ti structures with varying thicknesses

Table 9 Total resistance vs thickness, for Ti spreading resistance structures

a-BC:H film Thickness (nm)	148	236	486	596
R_T (Ω)	205	289	617	729

The Ti and a-BC:H produce an Ohmic junction at the boundary, so the spreading resistance model can be used to calculate the contact resistance of Ti at the boundary. The top metal contacts are deposited with a radius of 1mm, which is orders of magnitude

larger than the thicknesses of the a-BC:H films shown in Table 9. This simplifies the spreading resistance (section 2.4.3) of the film to a linear dependence on film thickness. (Equation 15, Figure 71).

Equation 15: $R_T = R_S + \frac{2R_c}{A} = \rho_S \frac{b}{\pi a^2} + \frac{2R_c}{A}$

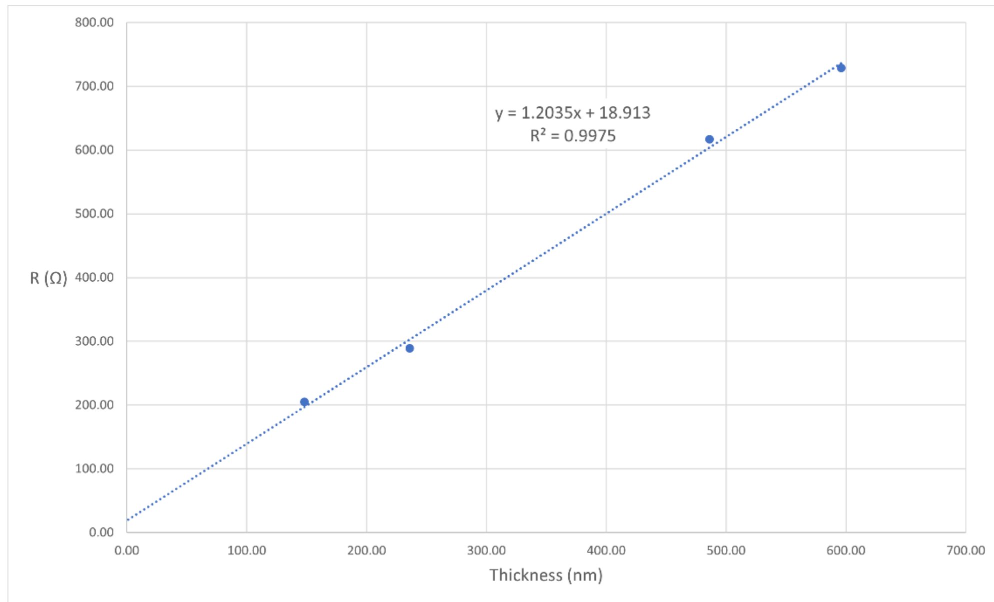

Figure 71 Total resistance vs a-BC:H thickness for Ti contact spreading resistance structure

The plotted total resistance as a function of film thickness is shown in Figure 71. Extrapolating the film thickness to zero eliminates the spreading resistance term from Equation 15 and produces a total resistance intercept, the value of twice the contact resistance divided by the contact area. For Ti contact this term is obtained from the linear extrapolation equation shown in Figure 71 and is **18.913Ω**.

The contact resistance R_c is then calculated to be approximately **0.297Ω-cm²** from Equation 16, as the area of the round top contact is the area of the circle with the radius of 1mm.

Equation 16: $R_c = \frac{18.913\Omega \cdot \pi (0.1cm)^2}{2} = 0.297\Omega cm^2$

Once the contact resistance is obtained, the resistivity of the n-type a-BC:H can be calculated from Equation 17. Total resistance R_T and film thickness b can be used from each set of measurements from Table 9 to calculate resistivity.

Equation 17: $\rho_s = \left(R_T - \frac{2R_C}{A}\right) \cdot \frac{\pi a^2}{b}$

Table 10 Resistivity of n-type a-BC:H from each set of spreading resistance structures

a-BC:H film Thickness (nm)	148	236	486	596
R_T (Ω)	205	289	617	729
ρ_s (x10^5 Ωcm)	3.95	3.6	3.87	3.74

The resistivity of n-type a-BC:H from each set of spreading resistance structures in Table 10 is averaged to **3.79x10^5Ωcm**. There have been wide ranges of resistivities reported for p-type a-BC:H from 10^8 to 10^{15} Ωcm [11,23]. Those resistivities were measured from the Ohmic regime from the V-I curve characteristics of metal-insulator-semiconductor a-B_xC:H_y/Si heterostructures, but it is unclear for which B-C-H compositional structures resistivities were reported and contact resistance has not been taken into account [23].

Identifying Ti as forming an Ohmic contact with n-type a-BC:H is important for fabricating the a-Si:H/a-BC:H devices. It is particularly beneficial that the contact resistance and resistivity measurements were performed in the direction of the device current flow, as that can provide insight into the device structure performance.

3.2 Chromium as the metal contact

The interface between Cr and p-type a-BC:H (from ortho-carborane) has been investigated in [11]. The V-I characteristics of the 250nm thick p-type a-BC:H film in the Cr/a-BC:H(p)/Cr structure fabricated in house are shown in Figure 72. The three V-I curves correspond to three out of the four dot contacts deposited on the p-type a-BC:H film (section 2.4.4). The V-I curve characteristics for this structure can be interpreted as the Schottky contact that is formed at both top and bottom Cr/a-BC:H contact boundary. As the ideal Schottky contact produces a diode-like behavior (Figure 44), the V-I characteristic in Figure 72 exhibits a symmetric curve. This is interpreted as two facing Schottky junction diodes in series that are formed at the Cr/a-BC:H junctions. When the voltage sweep is in the forward region, the current flows through one junction but is rectified at the other until breakdown, and vice versa for the reverse region, producing the V-I characteristics shown in Figure 72.

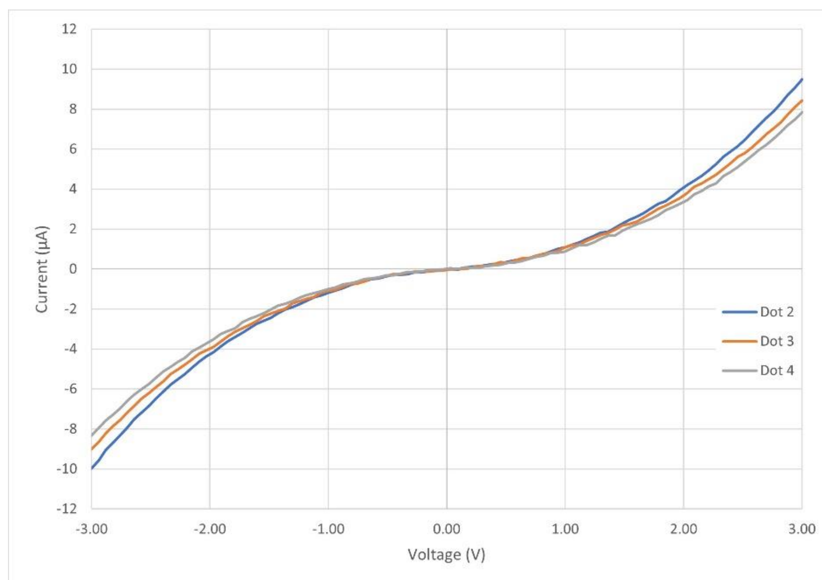

Figure 72 V-I characteristics of Cr/a-BC:H(p)/Cr structure

To investigate the interface of the a-BC:H/Cr structure, the presence of oxygen at the interface was profiled by XPS. The oxygen profile at the interface shown in Figure 73 was collected from a 170nm p-type a-BC:H film grown from ortho-carborane on a Cr substrate (deposition procedure described in section 2.4.4). To illustrate at which level in the film the oxygen spectra was collected the boron and chromium XPS spectra are shown at the same depth profile layers that are color coded.

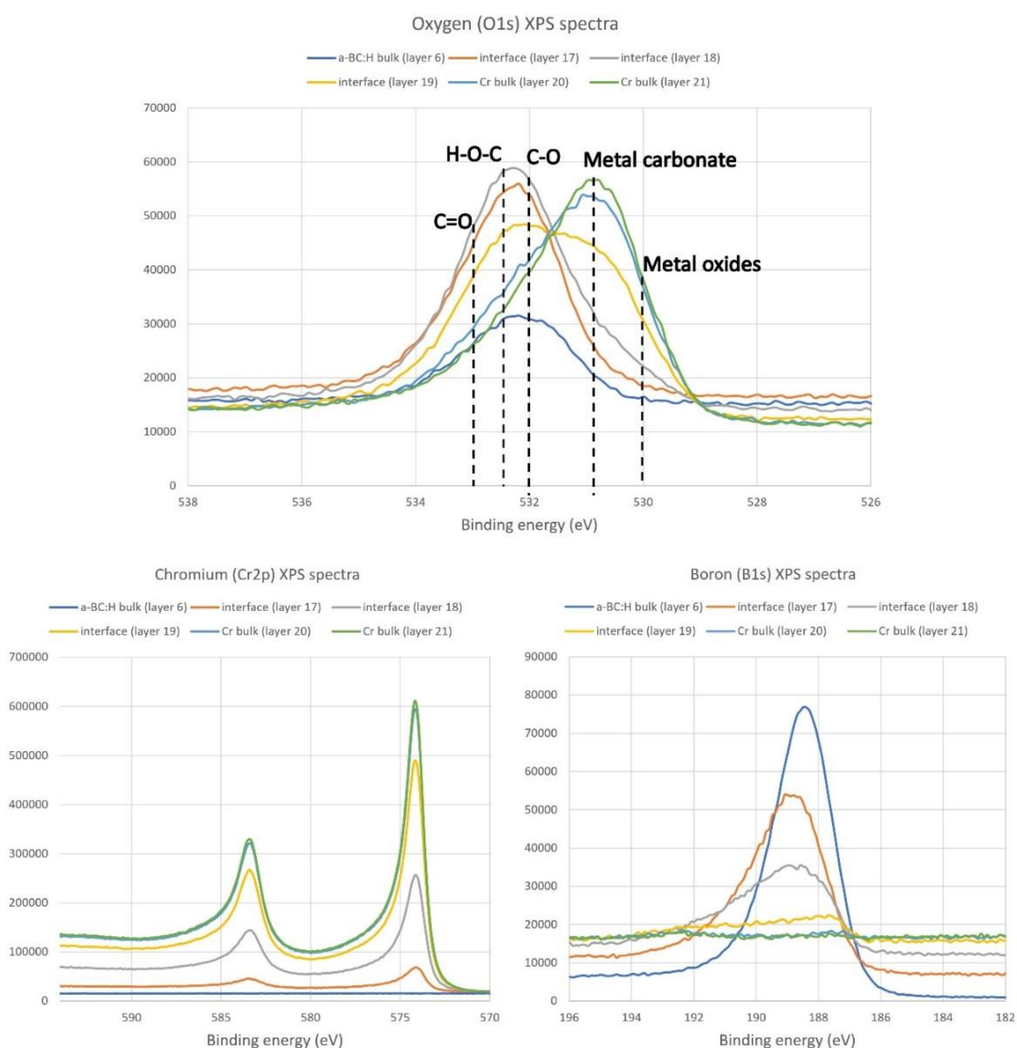

Figure 73 XPS spectra of oxygen, boron, and chromium in the p-type a-BC:H/Cr structure

From Figure 73, it can be seen that there is an increase in the oxygen when approaching the a-BC:H/Cr interface compared to the oxygen in the a-BC:H bulk. Additionally, a peak shift is noticeable when transitioning from the bulk a-BC:H through the interface to the bulk Cr due to the hydrogen and carbon bonding to oxygen H-O-C (~533eV) in the a-BC:H, organic carbon bonding of C-O (531.5-532eV) and C=O(~533eV), which transitions into metal carbonate (531.5-532eV) and metal oxide (529-530eV) peak shift at the bulk Cr surface.

To investigate the contact at the boundary of n-type a-BC:H/Cr, the structure is fabricated using the same process as the p-type a-BC:H/Cr structure (section 2.4.4). The V-I characteristics of approximately 480nm thick n-type a-BC:H grown from meta-carborane in the Cr/a-BC:H/Cr structure is shown in Figure 73. The V-I curve for the Cr contact on n-type a-BCH:H shows that the Schottky junction is formed at the barrier, in the same manner as the previously discussed Cr on p-type a-BC:H (Figure 72).

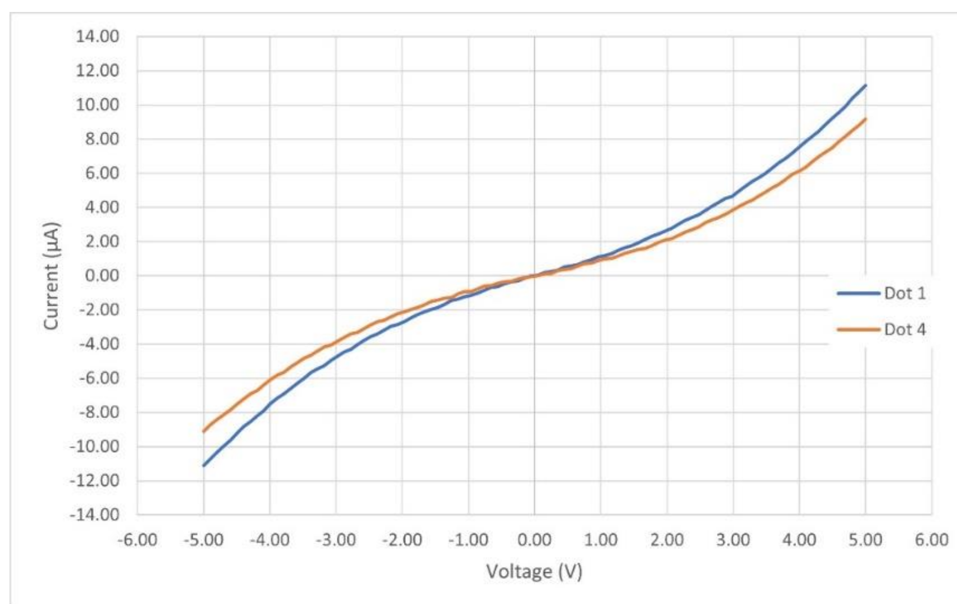

Figure 74 V-I characteristics of Cr/a-BC:H(n)/Cr structure

The established fabrication process for the n-type a-BC:H/Cr structure was identical to the p-type a-BC:H/Cr previously discussed, so the presence of the oxygen at the interface can be assumed for the n-type structure (Figure 73). To minimize oxygen presence in the device, the entire device fabrication process would be done in-situ. That type of process was not established in literature when discussing a-BC:H device fabrication. The difficulty with producing a device in-situ is the necessity for shadow masking device layers to produce contacts. The sputter yield of a-BC:H makes it difficult to sputter etch a-BC:H, so growing a metal substrate and the a-BC:H layer structure in-situ followed by opening a contact hole in the a-BC:H is not practical. Because of that, removing the back metal contact structure from vacuum and masking it before a-BC:H deposition is necessary in device fabrication. However, depositing a thin layer of metal on top of the masked metal substrate in-vacuo before a-BC:H deposition could provide a solution for reduction/minimization of oxygen at the metal/a-BC:H boundary (fabrication process illustrated in Figure 75).

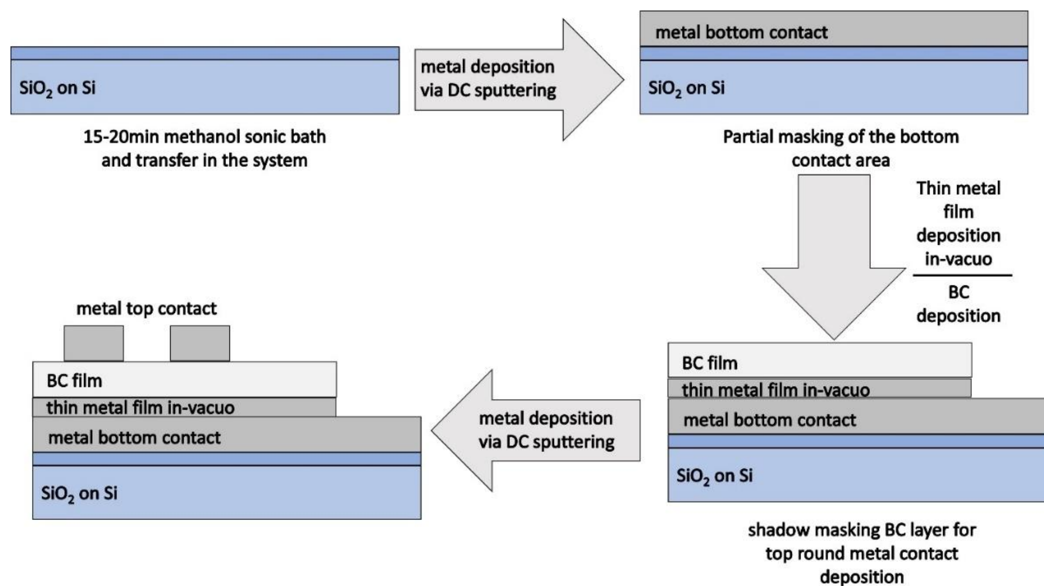

Figure 75 Procedure for metal/thin metal film in-vacuo/BC/metal structure fabrication

The 150nm n-type (meta-carborane) a-BC:H on Cr structure was fabricated by the procedure in Figure 75. The comparison of oxygen XPS spectra of the standard procedure sample (Figure 73) and the oxygen XPS spectra of the sample with thin Cr film deposited in-vacuo before the a-BC:H deposition (Figure 75) is shown in Figure 76.

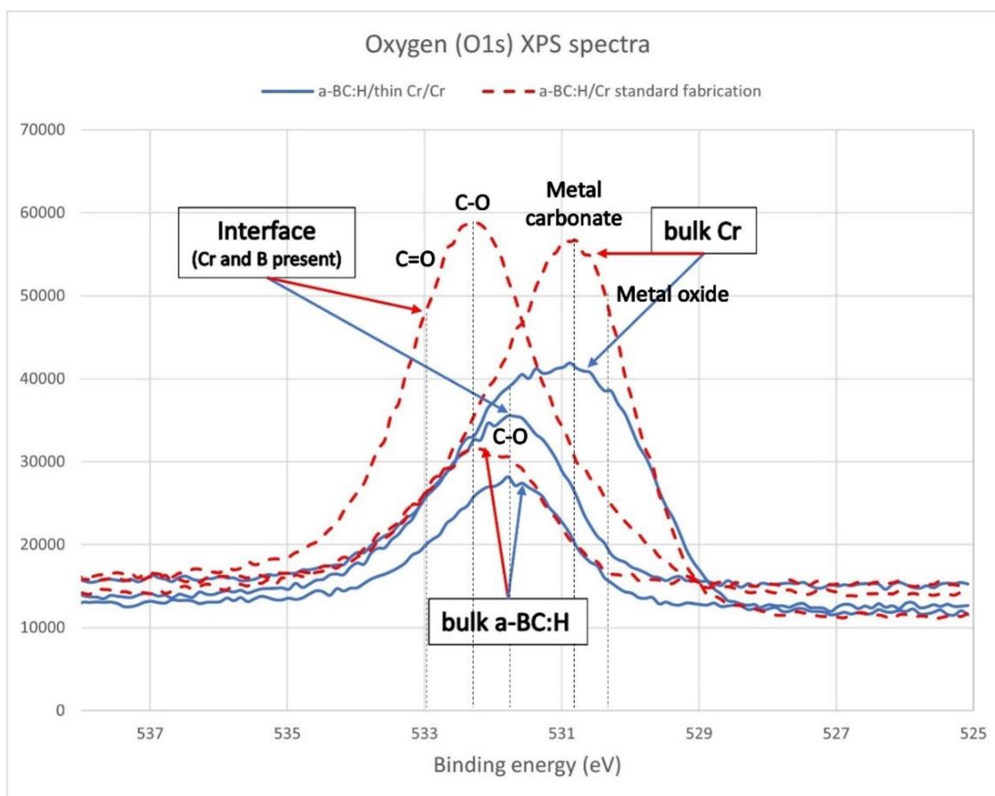

Figure 76 XPS oxygen spectra comparison of the a-BC:H/thin Cr/Cr structure and the a-BC:H/Cr structure fabricated by previously established procedure

The oxygen spectra were collected for each film at approximately the same depth layers to produce as accurate as possible comparison. From the XPS spectra in Figure 76 it can be noted that there is higher presence of oxygen when approaching the interface of a-BC:H/Cr structure deposited by the standard procedure (red dashed lines) than at the interface of the a-BC:H/thin Cr/Cr structure (solid blue lines). As there was no pre-deposition surface processing of the Cr substrate in the standard deposition procedure, the peak shift in oxygen previously discussed is expected as there is carbon and oxygen

contamination at the surface before a-BC:H deposition occurs. The surface contamination could additionally produce contamination throughout the a-BC:H as plasma induced reactions at the surface of the contaminated Cr can result in additional carbon and oxygen bonding to the a-BC:H resulting in the noticeable peak shifts and intensities. However, for the Cr thin-film in-vacuo procedure, both the bulk a-BC:H and the interface oxygen peaks are reduced and correspond to the C-O bonding at 531.5-532eV.

For structures deposited in-situ, it is expected that the oxygen at the interface would be minimized. To compare how the thin Cr film in-vacuo deposition fabrication procedure compares to complete in-situ fabrication, a 150nm n-type (meta-carborane) a-BC:H on Cr structure was fabricated in-situ.

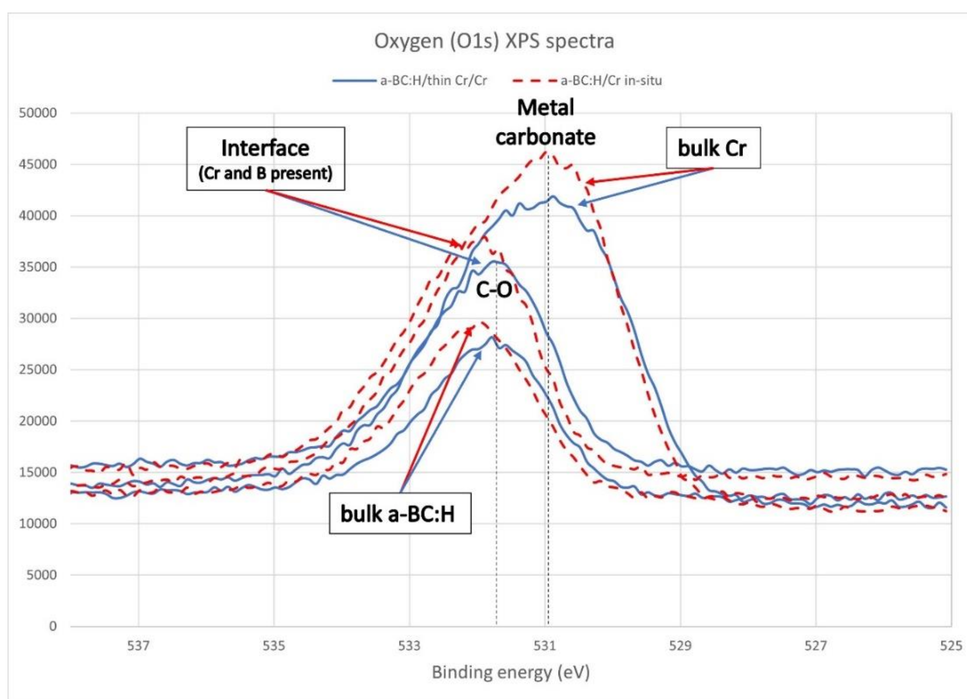

Figure 77 XPS oxygen spectra comparison of the a-BC:H/thin Cr/Cr structure and the a-BC:H/Cr structure fabricated in-situ

The oxygen spectra were collected at approximately the same depth near the interface to produce an accurate comparison. From the XPS spectra in Figure 77 it can be

noted that for both samples oxygen peak intensities and binding energies are comparable throughout the film. From this it can concluded that the process of depositing a thin Cr film in-vacuo before a-BC:H deposition produces an adequate approximation to the in-situ fabrication process.

The V-I characteristics of the Cr/thin Cr/a-BC:H/Cr structure (fabricated by the process illustrated in Figure 75) are shown in Figure 78. The thickness of the n-type a-BC:H grown from meta-carborane is approximately 150nm and it is the same structure that was shown to have reduced oxygen at the interface of Cr and a-BC:H. However, even with the reduction of oxygen at the a-BC:H(n)/Cr interface, the V-I characteristic of the structure shows that the Schottky junction is formed at the barrier of a-BC:H deposited on thin Cr film in-vacuo.

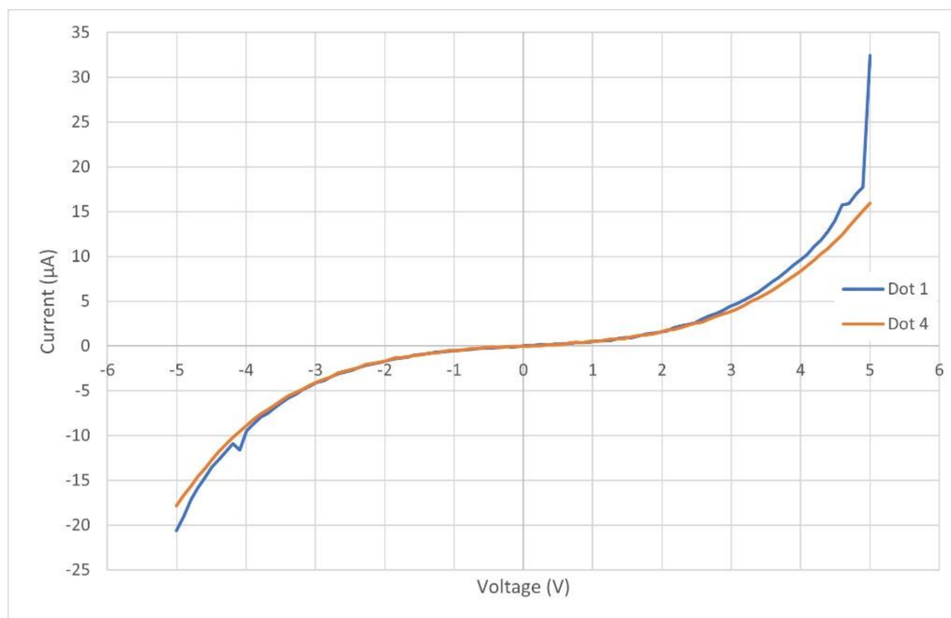

Figure 78 V-I characteristics of Cr/thin Cr/a-BC:H(n)/Cr structure

Chromium is one of the most commonly used bottom contact metals when fabricating structures with p-type a-BC:H grown from ortho-carborane. It was reportedly used for developing heteroisomeric devices as well as investigating 3d transition metal

doping of p-type a-BC:H [3,6]. As it was shown in this section, Cr forms a Schottky junction at the barrier with both n-type and p-type a-BC:H as both bottom and top contact. This makes it difficult to completely understand a heteroisomeric device behavior and the formation of the junction between an n-type and p-type a-BC:H layers, because of the existence of multiple junctions in series. This is illustrated by comparing the V-I characteristics in Figure 70 to those seen in Figure 78. The current output at the Ohmic junction of Ti/a-BC:H is three orders of magnitude larger than the current output at the Schottky junction of Cr/a-BC:H for similar contact areas. Clearly, accounting for metal/BC junction when fabricating devices is necessary.

3.3 Summary of metal contacts

In addition to titanium and chromium that have been discussed in detail in the previous sections, various metals from Table 7 have been used as contacts in the p-type and n-type a-BC:H structures. How those metals behave based on their corresponding V-I characteristics is presented in Table 11.

Table 11 Various metal contact formation with a-BC:H(n,p)

Metal	p-type a-BC:H (ortho-carborane)	n-type a-BC:H (meta-carborane)
Ag		Schottky
Al	Schottky	Schottky
Cr	Schottky	Schottky
Ti	Schottky	Ohmic
Hf	Schottky	
Ni	Schottky	Schottky
Cu		Schottky

The V-I characteristics of various fabricated metal/a-BC:H/metal structures are shown in Figure 79-85. It is important to note that a metal that forms an Ohmic junction at the contact with p-type a-BC:H grown from ortho-carborane using the established fabrication procedure, has not been identified. It is due to this and the doping limitations of a-BC:H grown from ortho-carborane (p-type) that the focus of the a-Si:H/a-BC:H heterojunction devices is based on a-Si:H(p-type)/a-BC:H(n-type) devices.

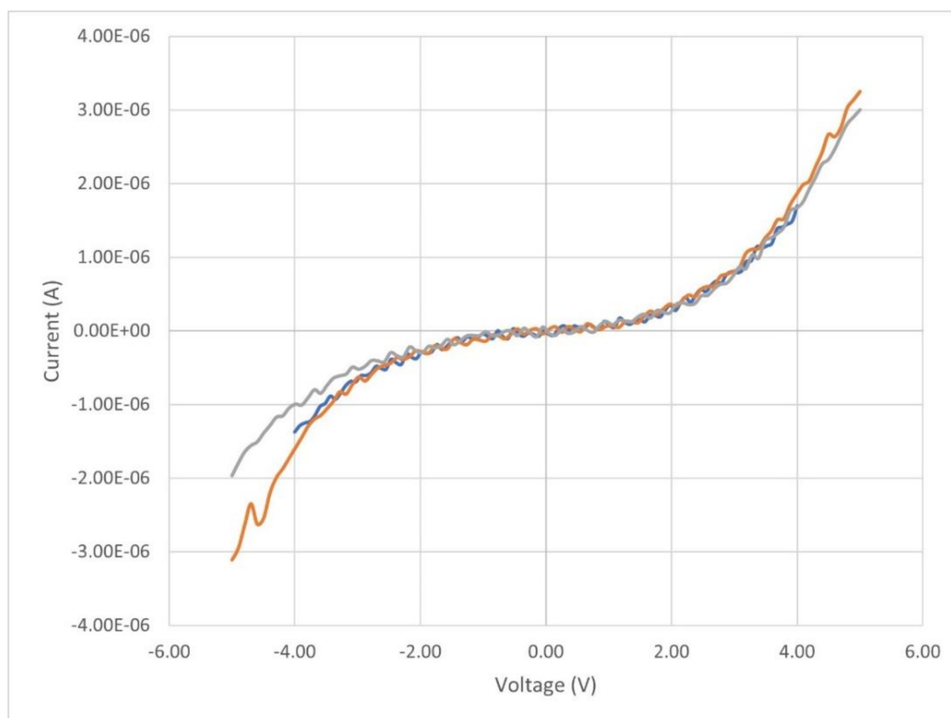

Figure 79 V-I characteristics of Ni/a-BC:H(p)/Ni structure

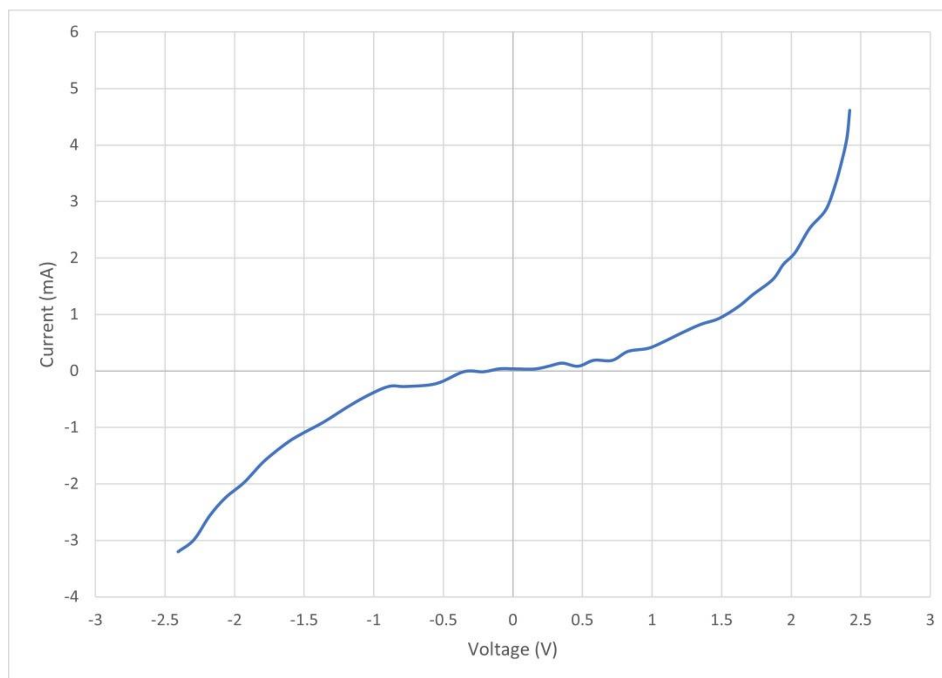

Figure 80 V-I characteristics of Ni/a-BC:H(n)/Ni structure

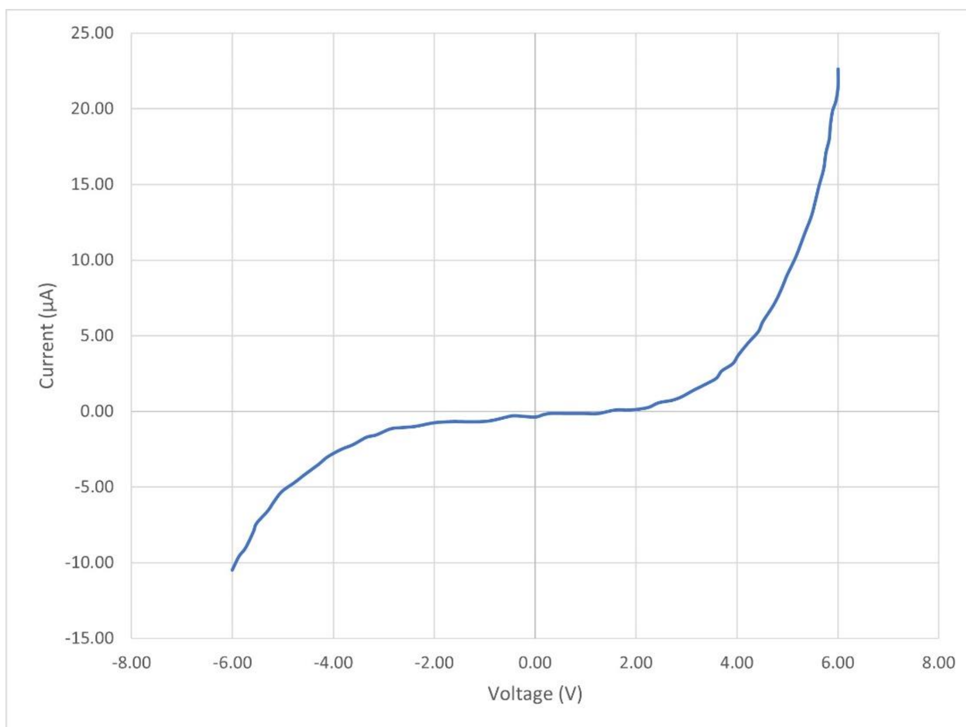

Figure 81 V-I characteristics of Cr/a-BC:H(p)/Ni structure

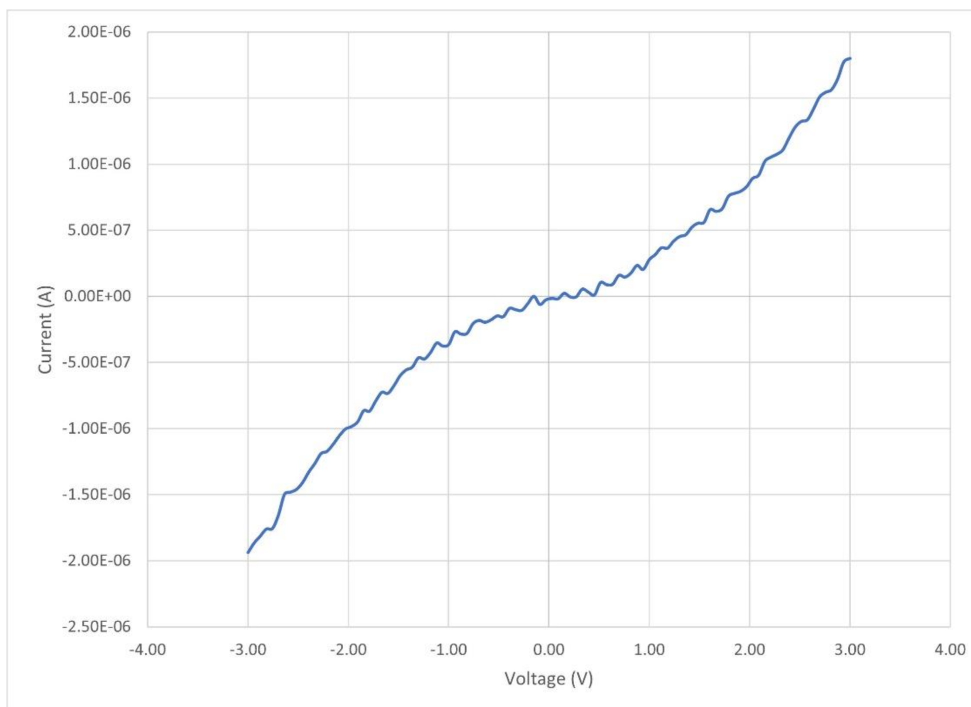

Figure 82 V-I characteristics of Al/a-BC:H(n)/Al structure

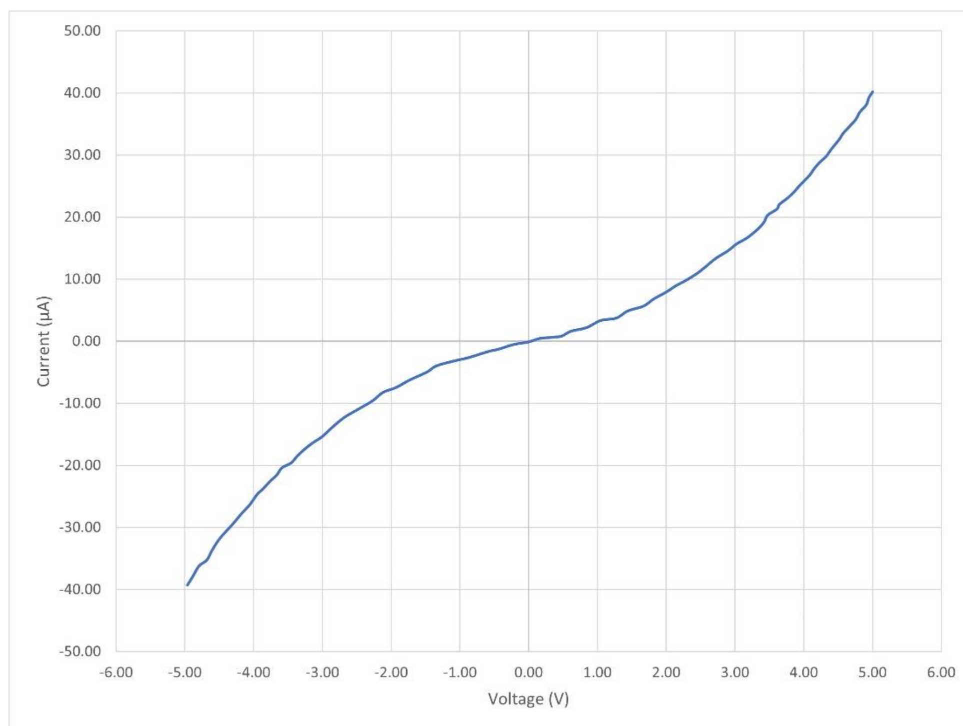

Figure 83 V-I characteristics of Cu/a-BC:H(n)/Al structure

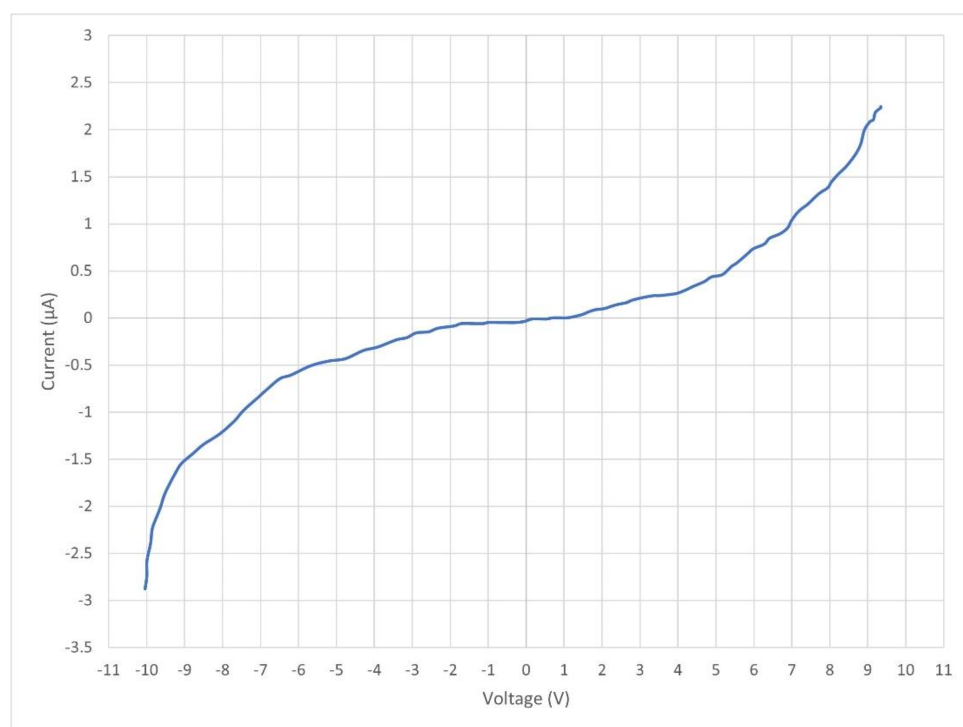

Figure 84 V-I characteristics of Al/a-BC:H(p)/Al structure

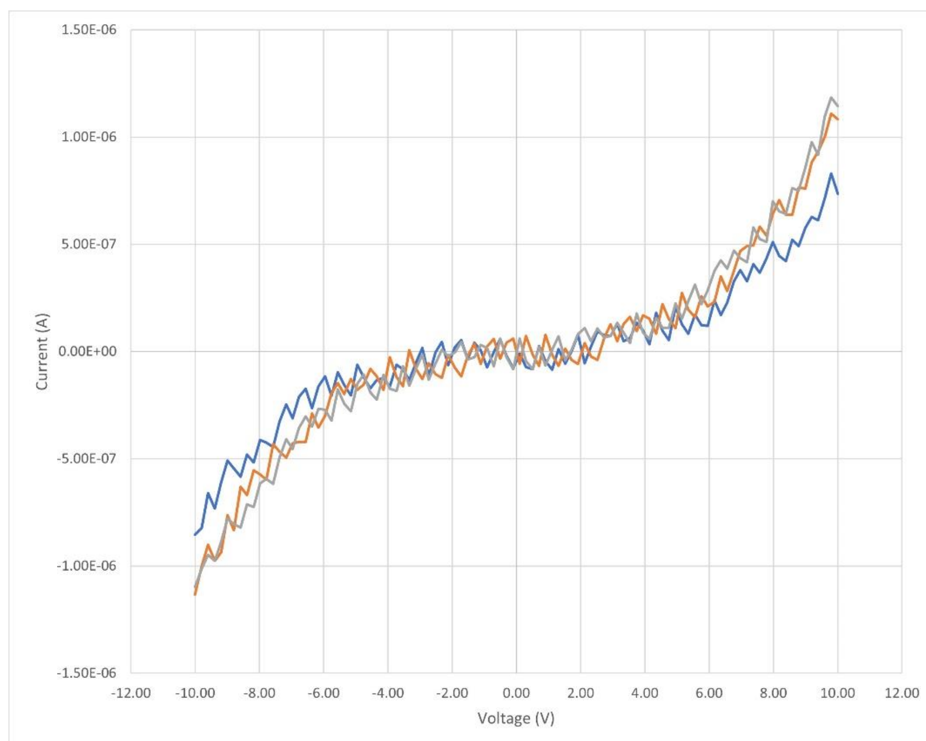

Figure 85 V-I characteristics of Hf/a-BC:H(p)/Hf structure

3.4 References

[1] A.N. Caruso, P. Dowben, et al, The all-boron carbide diode neutron detector: Comparison with theory, Materials Science and Engineering: B. 135. 129-133, 2006, http://doi.org/10.1016/j.mseb.2006.08.049

[2] Caruso, A. & Billa, Ravi & Balaz, Snjezana & Brand, J. I. & Dowben, Peter, The heteroisomeric diode. Journal of Physics Condensed Matter. 16. L139-L146. (2004), https://doi.org/10.1088/0953-8984/16/10/L04.

[3] P.A. Dowben, Orhan Kizilkaya, Jing Liu, B. Montag, K. Nelson, I. Sabirianov, J.I. Brand, 3d transition metal doping of semiconducting boron carbides, Materials Letters, Volume 63, Issue 1, 2009, Pages 72-74, ISSN 0167-577X, https://doi.org/10.1016/j.matlet.2008.09.004

[4] Elena Echeverría, Bin Dong, Aiyun Liu, Ethiyal R. Wilson, George Peterson, Michael Nastasi, Peter A. Dowben, Jeffry A. Kelber, Strong binding at the gold (Au) boron carbide interface, Surface and Coatings Technology, Volume 314, 2017, Pages 51-54, ISSN 0257-8972, https://doi.org/10.1016/j.surfcoat.2016.08.081

[5] D.N. McIlroy, Jiandi Zhang, P.A. Dowben, P. Xu, D. Heskett, The coadsorption of metals and molecular icosahedra on Cu(100), Surface Science, Volume 328, Issues 1–2, 1995, Pages 47-57, ISSN 0039-6028, https://doi.org/10.1016/0039-6028(95)00040-2

[6] Carlson, L., LaGraffe, D., Balaz, S. et al. Doping of boron carbides with cobalt, using cobaltocene. Appl. Phys. A **89**, 195–201 (2007). https://doi.org/10.1007/s00339-007-4086-6

[7] K. Osberg et al., A Handheld Neutron-Detection Sensor System Utilizing a New Class of Boron Carbide Diode, in IEEE Sensors Journal, vol. 6, no. 6, pp. 1531-1538, Dec. 2006, https://doi.org/10.1109/JSEN.2006.883905

[8] Seong-Don Hwang, N. B. Remmes, P. A. Dowben, D. N. McIlroy; Nickel doping of boron carbide grown by plasma enhanced chemical vapor deposition. Journal of Vacuum Science & Technology B: Microelectronics and Nanometer Structures Processing, Measurement, and Phenomena 1 July 1996; 14 (4): 2957–2960. https://doi.org/10.1116/1.588942

[9] McIlroy, D.N.; Hwang, S.-D.; Yang, K.; Remmes, N.; Dowben, Peter A.; Ahmad, A.A.; Ianno, N.J.; Li, J.Z.; and Jiang, H.X., The incorporation of Nickel and Phosphorus dopants into Boron-Carbon alloy thin films, (1998). Peter Dowben Publications. 105. https://digitalcommons.unl.edu/physicsdowben/105

[10] Seong-Don Hwang, Ken Yang, P. A. Dowben, Ahmad A. Ahmad, N. J. Ianno, J. Z. Li, J. Y. Lin, H. X. Jiang, D. N. McIlroy; Fabrication of n-type nickel doped B5C1+δB5C1+δ homojunction and heterojunction diodes. Appl. Phys. Lett. 24 February 1997; 70 (8): 1028–1030. https://doi.org/10.1063/1.118434

[11] Michelle M. Paquette et al, Understanding the Electronic Structure of the a-B5C:Hx-to-Metal Interface, University of Missouri-Kansas City, 2016, https://apps.dtic.mil/sti/tr/pdf/AD1011068.pdf

[12] H. Kato, Production of Gold-198 Grains, Japan Atomic Energy Research Institute, Iharaki-ken, Japan, https://link.springer.com/content/pdf/10.1007/BF03215093.pdf

[13] G.S.Zahn and F.A.Genezini, Half-life determination for ^{108}Ag and ^{110}Ag, AIP Conference Proceedings 1625, 166 (2014); https://doi.org/10.1063/1.4901785

[14] Mirzokarimov, Mirzojamshed. Boron carbide hetero-isomeric device fabrication by PECVD from isomeric precursor ortho-carborane and meta-carborane. MS Thesis. University of Nebraska, 2019

[15] J. Holzl, F.K. Schulte, Work Functions of Metals, in Solid State Surface, Editor: G. Hohler, Springer-Verlag, Berlin, 1979.

[16] J.C. Riviere, Work Function: Measurement and Results, in Solid State Surface Science, vol. 1, Editor: M.Green, Decker, New York, 1969,

[17] Michaelson, H.B. (1977) The Work Function of the Elements and Its Periodicity. Journal of Applied Physics, 48, 4729-4733. https://doi.org/10.1063/1.323539

[18] E. A. Kraut, R. W. Grant, J. R. Waldrop, and S. P. Kowalczyk, Precise Determination of the Valence-Band Edge in X-Ray Photoemission Spectra, Application to Measurement of Semiconductor Interface Potentials, Phys. Rev. Lett. 44, 1620, 1980, https://doi.org/10.1103/PhysRevLett.44.1620

[19] K.C. Sanal, Rafael Ballinas Morales, Victoria E. Gonzàlez Flores, S. Shaji, P.K. Nair, M.T.S. Nair, Co-sputtered Zn1-xMgxO films and interfacial band offsets at heterojunctions with SnS-CUB, Journal of Alloys and Compounds, Volume 763, 2018, Pages 909-915, ISSN 0925-8388, https://doi.org/10.1016/j.jallcom.2018.05.276.

[20] Kumar, M., Rajpalke, M.K., Roul, B., Bhat, T.N., Kalghatgi, A.T. and Krupanidhi, S.B. (2012), Determination of MBE grown wurtzite GaN/Ge_3N_4/Ge

heterojunctions band offset by X-ray photoelectron spectroscopy. Phys. Status Solidi B, 249: 58-61. https://doi.org/10.1002/pssb.201147318

[21] Sean W. King, Marc French, Guanghai Xu, Benjamin French, Milt Jaehnig, Jeff Bielefeld, Justin Brockman, Markus Kuhn, Valence band offset and Schottky barrier at amorphous boron and boron carbide interfaces with silicon and copper, Applied Surface Science, Volume 285, Part B, 2013, Pages 545-551, ISSN 0169-4332, https://doi.org/10.1016/j.apsusc.2013.08.090

[22] Nina Hong, M. A. Langell, Jing Liu, Orhan Kizilkaya, S. Adenwalla; Ni doping of semiconducting boron carbide. J. Appl. Phys. 15 January 2010; 107 (2): 024513, https://doi.org/10.1063/1.3284205

[23] Bradley J. Nordell, Christopher L. Keck, Thuong D. Nguyen, A.N. Caruso, Sudhaunshu S. Purohit, William A. Lanford, Dhanadeep Dutta, David Gidley, Patrick Henry, Sean W. King, Michelle M. Paquette, Tuning the properties of a complex disordered material: Full factorial investigation of PECVD-grown amorphous hydrogenated boron carbide, Materials Chemistry and Physics, Volume 173, 2016, Pages 268-284, ISSN 0254-0584, https://doi.org/10.1016/j.matchemphys.2016.02.013.

Chapter 4 – Investigation of Boron Carbide (a-BC:H) Devices

There have been different types of devices fabricated, investigated, and reported in literature (as discussed in section 2.3), with the primary focus on heteroisomeric devices developed from p-type and n-type a-BC:H [1-7]. However, since as the effects of the contacts have not been accounted for previously, the understanding of the devices has not been complete. With qualitatively understanding the formation of the metal/a-BC:H contacts, various devices can be fabricated and investigated to further understand a-BC:H behavior in a p-n junction structure.

The XPS measurements are used for characterization of the interface between the c-Si, a-Si and the a-BC:H, primarily to determine the presence of oxygen that can negatively affect junction formation at the boundary. Additionally, XPS is used for obtaining the valence band offset (VBO), from which the band structure diagram at the interface can be constructed.

The valence band offset at the boundary of two semiconductors is calculated via the Kraut method given by Equation 18 [8].

Equation 18: $VBO = \Delta E_v = (CL - VBM)_{Si} - (CL - VBM)_{BC} + (CL_{BC} - CL_{Si})_{int}$

The core level (CL) binding energies of the bulk layers and the core level (CL_{int}) binding energies of the layers at the interface (where both element layer peaks are present) are obtained from the XPS elemental core level measurements. This is a general calculation that can be utilized for various materials [8]. For a-BC:H structures, core level binding energy of B is monitored, where the presence of C bonding with B is accounted for by the shifts in the core level B energies compared to the pure elemental B. The valence band

maximum (VBM) of bulk materials is obtained by linear extrapolation of the valence band leading edge emission from the valence measurements [8-12].

The optical model of the ellipsometric data provides insight into the bandgap of a-BC:H, as the extinction coefficient (k) from the model of the material can be used to form a Tauc plot. In the Tauc plot, the term in Equation 19 is plotted as a function of the incident photon energy (hν). The absorption coefficient (α) is calculated from the extinction coefficient and the wavelength (λ) of the incident photons.

Equation 19: $y = \sqrt{h\nu\alpha} = \sqrt{h\nu \frac{4\pi k}{\lambda}}$

The Tauc plot example for an n-type a-BC:H is shown in Figure 86, where the bandgap energy is a linearly extrapolated intercept with the horizontal axis. The bandgap energy of p-type a-BC:H has previously been reported to be in the 1-2.5eV range [11,12].

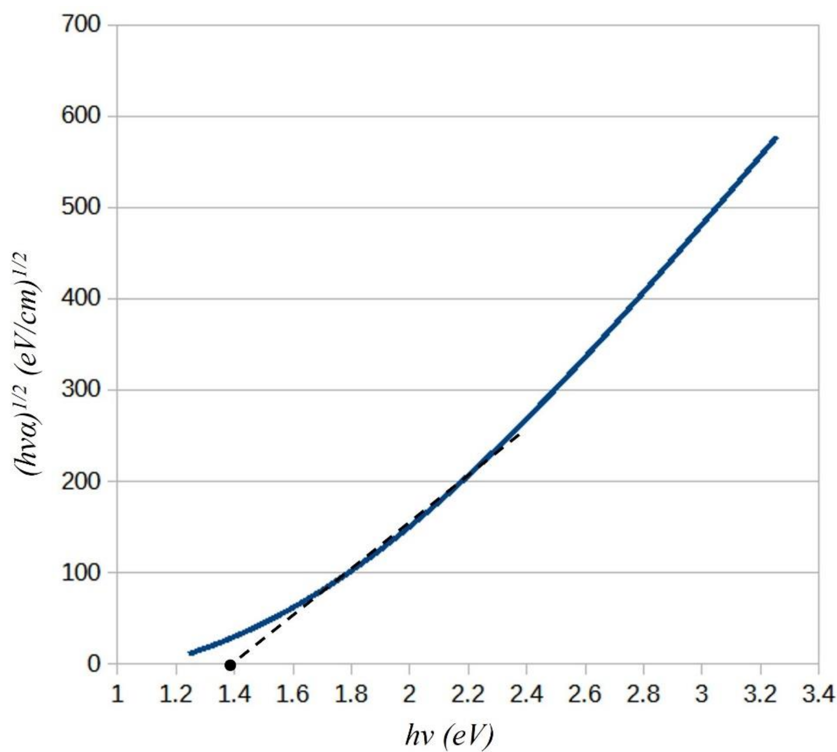

Figure 86 The a-BC:H Tauc plot for obtaining the bandgap

Additionally, the bandgap of the material is one of the variables in the Cody-Lorentz oscillator optical model. From the Tauc plot and the Cody-Lorentz model, the range of bandgap energy of the n-type a-BC:H film is between 1.1eV and 1.5eV. The thickness of the a-BC:H layer in the device structure is obtained as discussed in chapter 3, where the ellipsometric data is modeled via the Cody-Lorentz optical model which produces the value of thickness as one of the variables modeled. Generally, the thickness range of a-BC:H for device fabrication is in the 150-500nm range.

In this chapter the focus of the investigation is the a-Si:H/a-BC:H heterojunction device, and the direct comparisons with c-Si/a-BC:H heterojunction devices. All the devices have been fabricated by the process established in sections 2.3.4 and 2.3.6.

4.1 Single crystal silicon-boron carbide device

Different types of heterojunction devices were discussed in section 2.3.3, but single crystal silicon and a-BC:H are interesting when discussing heterojunction devices because single crystal silicon as a semiconductor is well understood (mobility, low resistivity, bandgap, etc). This provides the ability to investigate the band structure of the device as well as the V-I characteristics of the device depending on the thickness of the a-BC:H film.

The V-I characteristics of a reported c-Si(n)/a-BC:H(p) heterojunction device is shown in Figure 87 [8]. However, as n-type a-BC:H is the focus of developing a novel heterojunction device, c-Si(p)/a-BC:H(n) structures were fabricated in the laboratory and investigated. Additionally, as both thickness of the a-BC:H layer and the metal contacts have not been specified in literature, it is difficult to discuss the specific device characteristics aside from the general exponential behavior comparable to the commercially available silicon diode (Figure 57).

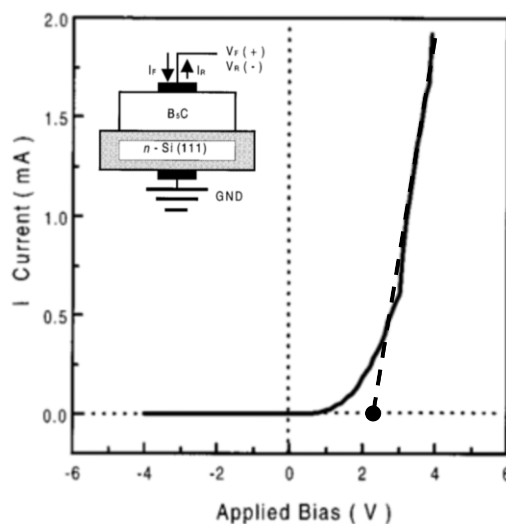

Figure 87 V-I characteristics of n-type single crystal Si and p-type BC heterojunction device

The V-I characteristics of devices fabricated in laboratory by growing an approximately 500nm and 350nm a-BC:H film from meta-carborane on p-type single crystal silicon at the substrate temperature of 350ºC (procedure in section 2.3.4) are shown in Figure 88 and 89.

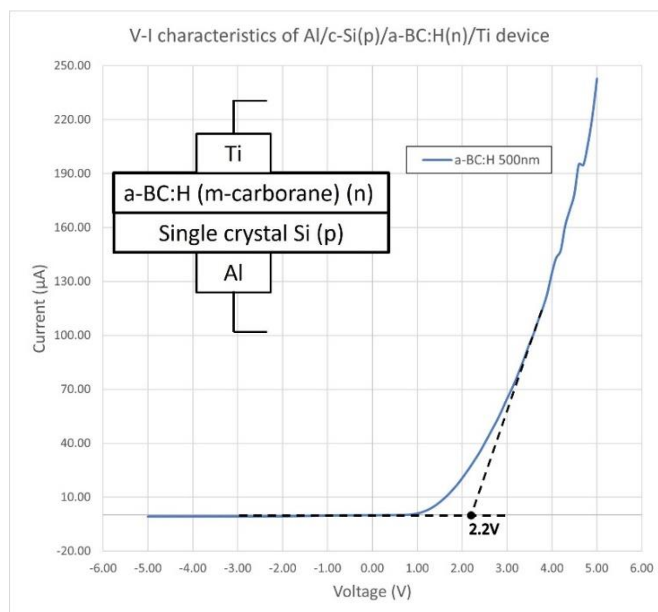

Figure 88 V-I characteristics of a 500nm n-type a-BC:H on single crystal silicon device

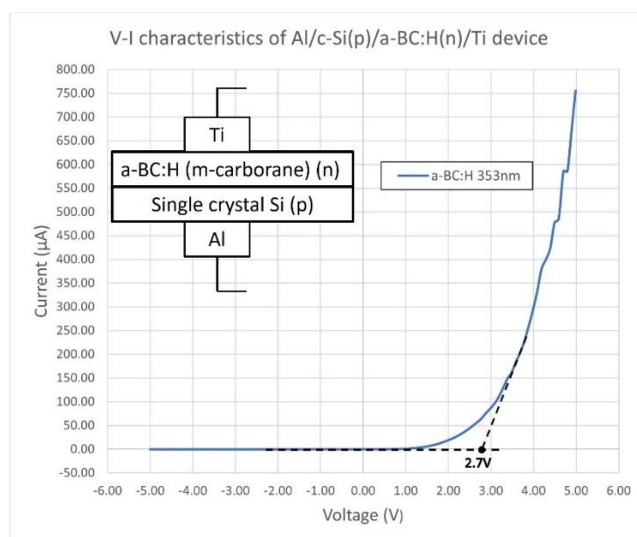

Figure 89 V-I characteristics of a 350nm n-type a-BC:H on single crystal silicon device

Both devices, 500nm a-BC:H and 350nm a-BC:H, exhibit comparable exponential device behavior to the reported device in literature as well as the commercially available silicon diode. The device with the 350nm layer of a-BC:H has the turn-on voltage of ~2.7V and produces higher current output (~750µ at 5V), while the 500nm a-BC:H device with ~2.2V turn on voltage produces current output of ~250µA at 5V. The direct comparison of the two devices V-I characteristics is shown in Figure 90.

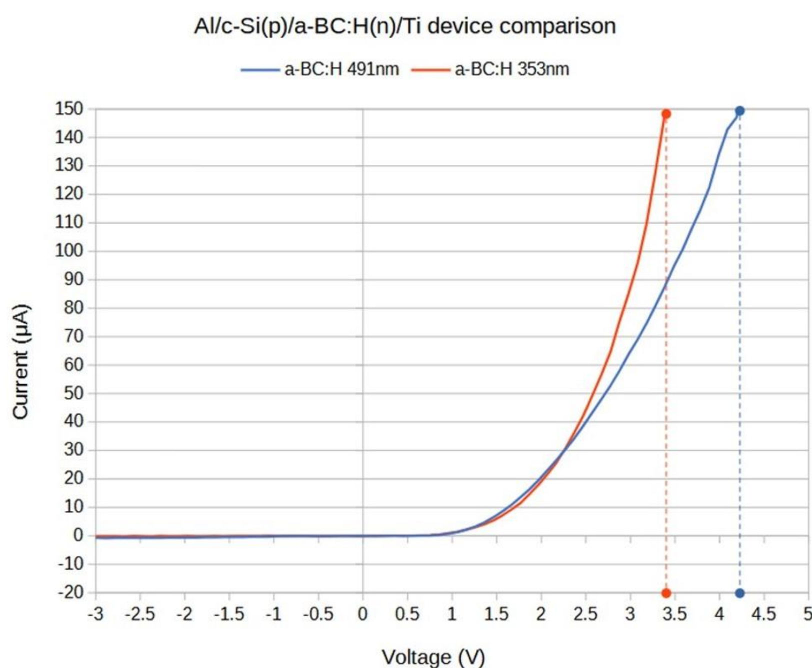

Figure 90 Comparison between two c-Si/a-BC:H devices with different a-BC:H thicknesses

It can be noticed that the turn-on voltage for 353nm and 500nm c-Si/a-BC:H devices is comparable at approximately 2.7V and 2.2V respectively. As the voltage bias is increased the device with the 350nm a-BC:H layer reaches the 150µA current output at lower bias (~3.4V) than the device with 500nm a-BC:H layer (~4.2V). The differences in device behavior can be attributed to the formation of the junction at the interface, the size of the intimate metal contact or the combination of both. It is also important to note that

the breakdown for both devices does not occur at bias voltage of up to 5V. If the c-Si/a-BC:H device was a homojunction device this would indicate that the depletion region is almost entirely in the lightly doped a-BC:H layer and that the device properties would be dictated by a-BC:H. However, for a heterojunction device this might not be the case as the device behavior is also dependent on the heterojunction band alignment at the interface.

To construct the band diagram for c-Si(p)/a-BC:H(n), XPS measurements were used to calculate the valence band offset via the Kraut method (Equation 20) [8].

Equation 20: $VBO = \Delta E_v = (CL - VBM)_{Si} - (CL - VBM)_{BC} + (CL_{BC} - CL_{Si})_{int}$

The core level peaks (CL) in the bulk, and core level peaks at the interface (CL_{int}) are shown in Figure 91 and Figure 92 and were obtained from the depth profile XPS spectra of core level Si^{2p} and B^{1s} in the bulk and at the interface.

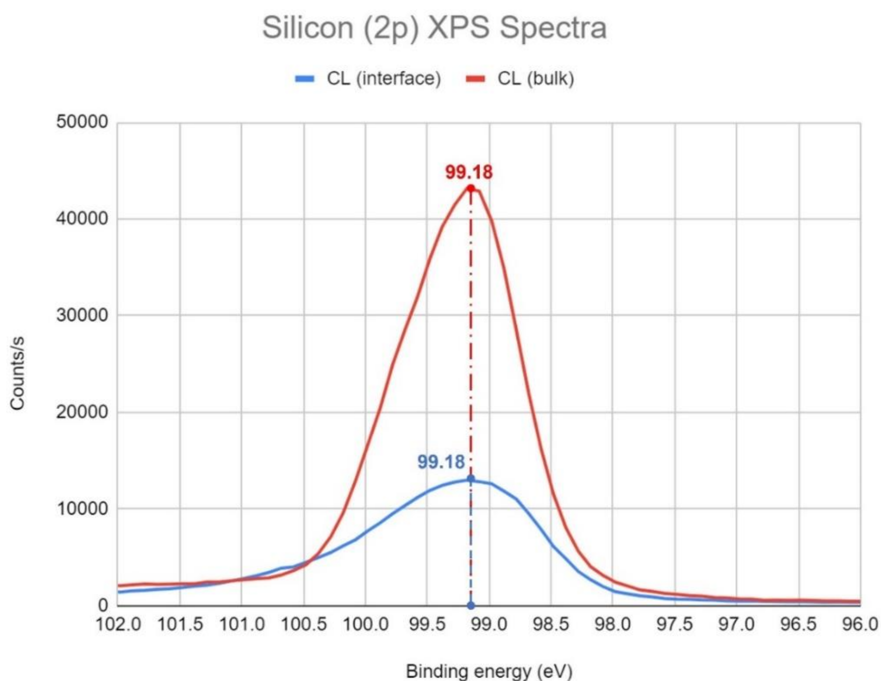

Figure 91 XPS spectra of Si in the bulk and at the interface with a-BC:H

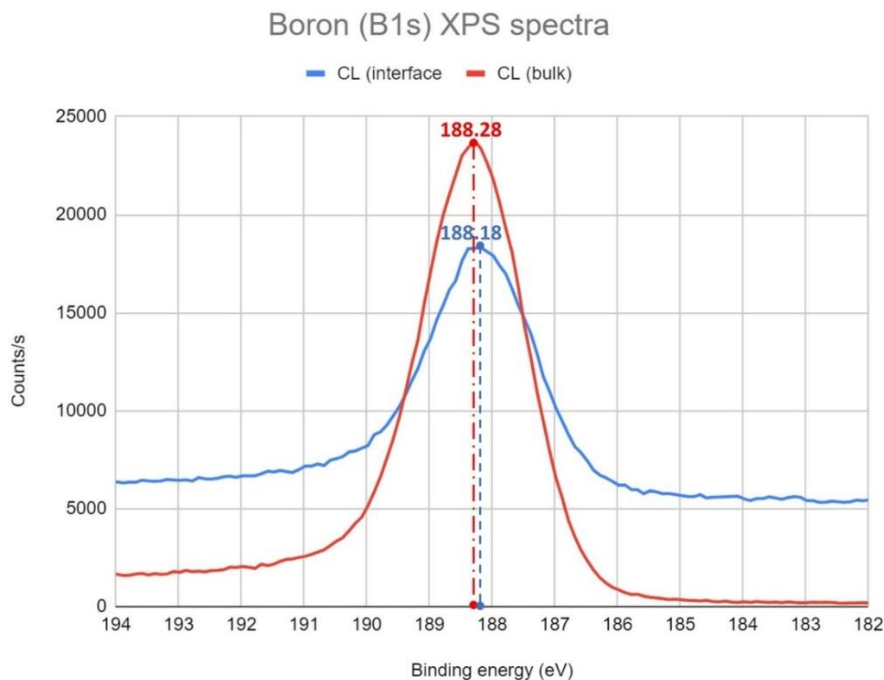

Figure 92 XPS spectra of B (a-BC:H) in the bulk and at the interface with c-Si

The core level peaks and valence band maxima (VBM) of a-BC:H and c-Si that are used to calculate valence band offset of the a-BC:H/c-Si are shown in Table 12.

Table 12 Core level peaks and valence band maxima for a-BC:H and c-Si

Layer	**CL (eV)**	**CL_{int} (eV)**	**VBM (eV)**
a-BC:H (n-type)	188.28±0.1	188.18±0.1	0.63±0.05
c-Si (p-type)	99.18±0.1	99.18±0.1	0.2±0.05

The valence band maxima of the a-BC:H and c-Si in the bulk were obtained from the leading edge of the valence band XPS spectra [9-13] shown in Figure 93 and Figure 94.

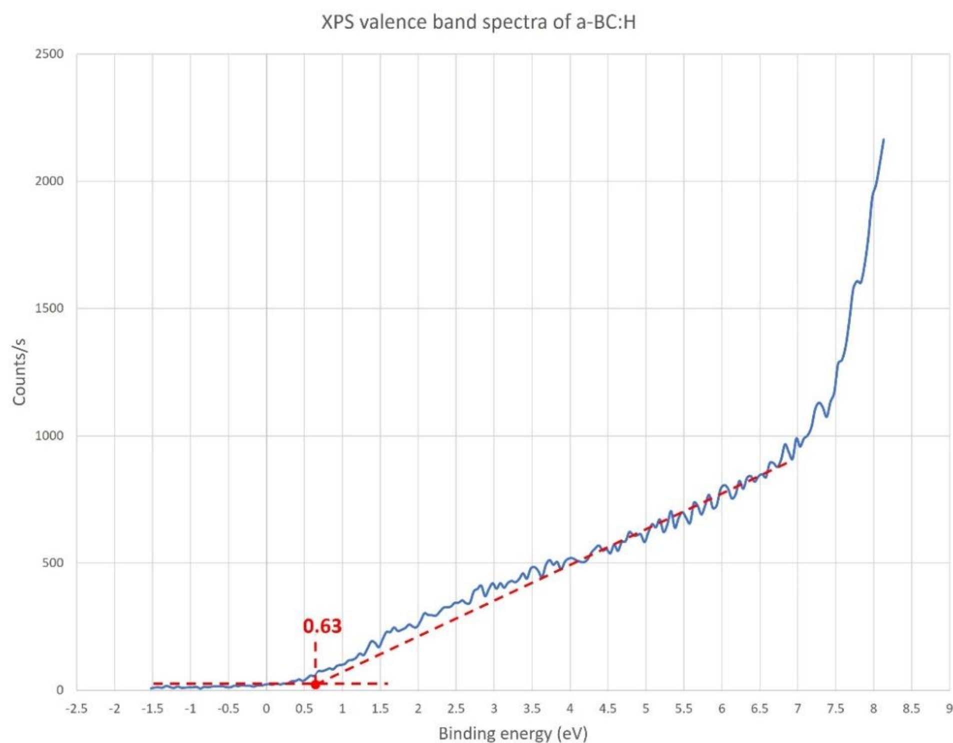

Figure 93 Valence band maximum of a-BC:H from XPS spectra from the bulk

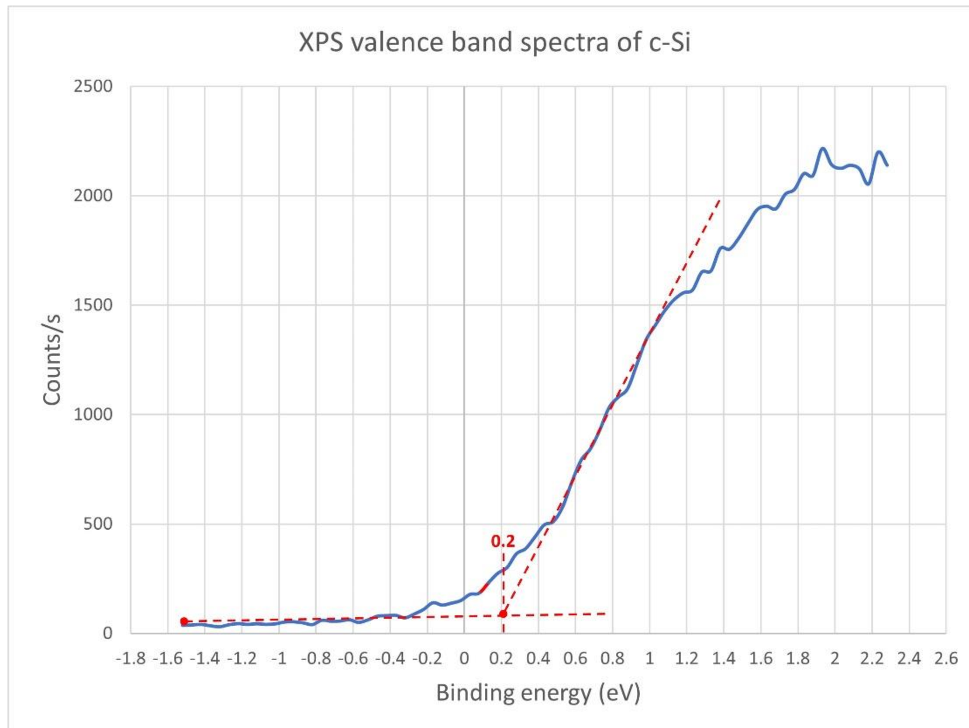

Figure 94 Valence band maximum of c-Si from XPS spectra from the bulk

Using the core level peak and valence band maxima binding energies from Table 12 with Equation 20, the valence band offset of a-BC:H(n)/c-Si(p) structure is calculated to be **0.33eV** as seen in Equation 21.

Equation 21: $VBO = \Delta E_v = 98.98 - 187.65 + 89 = 0.33eV$

Kraut's method is used to calculate the valence and conduction band offsets at the interface of two semiconductors, a-BC:H and c-Si in this case [8]. At the interface, the Fermi levels of a-BC:H and c-Si must align, so the core level energies used to calculate VBO and CBO are referenced with respect to the Fermi level. Additionally, from the core level (bulk) XPS measurements in Table 12 and the bandgap energies of a-BC:H (1.2eV) and c-Si (1.1eV), the conduction band minimum and valence band maximum at the interface for both a-BC:H and c-Si can be calculated using Equations 22 and 23 respectively.

Equation 22 $E_C(i) = (CL - VBM) + E_G - CL_{int}$

Equation 23 $E_V(i) = CL_{int} - (CL - VBM)$

$E_C(i)_{BC} = (CL - VBM)_{BC} + \mathrm{E}_G^{BC} - CL_{int}^{BC} = 0.67eV$

$E_V(i)_{BC} = CL_{int}^{BC} - (CL - VBM)_{BC} = 0.53eV$

$E_C(i)_{c-Si} = (CL - VBM)_{c-Si} + \mathrm{E}_G^{c-Si} - CL_{int}^{c-Si} = 0.90eV$

$E_V(i)_{c-Si} = CL_{int}^{c-Si} - (CL - VBM)_{c-Si} = 0.2eV$

Using the valence band offset, band gap energies and conduction and valence band positions with respect to the Fermi level, the band diagram at the interface of the a-BC:H and c-Si heterojunction is illustrated and shown in Figure 95.

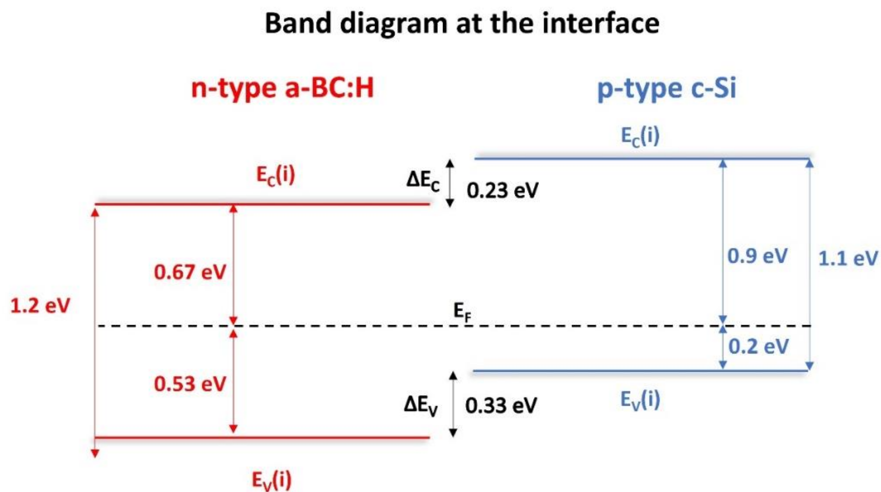

Figure 95 The a-BC:H(n)/c-Si(p) heterojunction band diagram at the interface

As valence band maxima of c-Si and a-BC:H obtained from the XPS measurements are the positions of the valence band maxima with respect to the Fermi level in the a-BC:H and c-Si bulk, the band diagram of the entire heterojunction can be illustrated as shown in Figure 96.

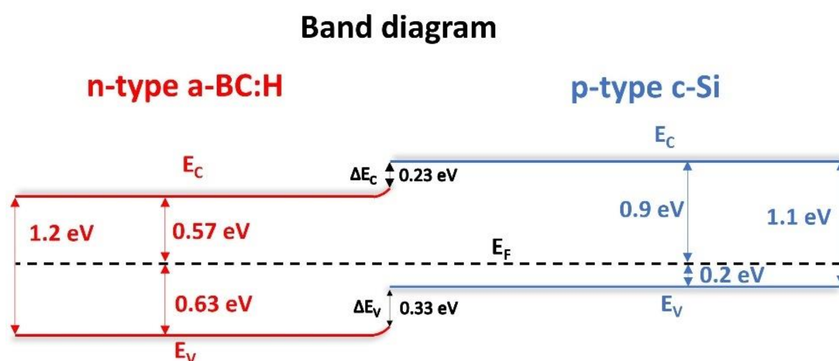

Figure 96 The a-BC:H(n)/c-Si(p) heterojunction band diagram

The Fermi levels at the junction must be aligned and as the Fermi levels of a-BC:H and c-Si align, bending of the conduction and valence band occurs at the interface. Figure 95 illustrates the band structure at the interface, where the position of the

conduction and valence band energies with respect to Fermi level are not the same as the conduction and valence band energy in the bulk of a-BC:H and c-Si as shown in Figure 96. As the density of states of a-BC:H is unknown, the exact Fermi level position in the bulk of a-BC:H cannot be calculated. However, as the c-Si is a well-known semiconductor, the Fermi level position with respect to the valence band of c-Si in the bulk can be calculated using Equation 24, where the doping of the p-type c-Si wafer used is approximately $1.5x10^{15}cm^{-3}$ and p-type density of states $1.04x10^{19}cm^{-3}$.

Equation 24: $E_F - E_V = kT \cdot ln\left(\frac{N_V}{p}\right) = 0.026eV \cdot ln\left(\frac{1.04 \cdot 10^{19}}{1.5 \cdot 10^{15}}\right) = 0.2299eV$

N_V – p-type density of states of single crystal silicon (N_V)

p – hole concentration of the used p-type c-Si wafer

The valence band maximum binding energy with respect to the Fermi level in the bulk of c-Si obtained by the XPS measurements is shown to be approximately 0.2eV (Figure 94). Both calculated and experimentally obtained values are comparable within the 0.05eV step resolution of the XPS valence band measurements. This confirms the approach of the Kraut's method using the XPS measurements to investigate the band structure at the interface. The band diagram of the a-BC:H/c-Si interface will be further discussed in the following sections.

And even though single crystal silicon is not a viable long-term solution as it degrades over time due to radiation damage, it is a very powerful device layer with a-BC:H as it has well known properties that can be utilized to provide insight into the accuracy of the XPS measured results and the formation of the interface with a-BC:H. In the following section, hydrogenated amorphous silicon is discussed as a substitute for single crystal silicon.

4.2 Amorphous silicon-boron carbide device

As the single crystal silicon degrades over time due to radiation damage (section 2.3.1), the hydrogenated amorphous silicon has potential to produce neutron voltaic devices by forming heterojunction structures with the a-BC:H, addressing the degradation due to radiation damage of single crystal silicon by its amorphous structure and presence of hydrogen (section 2.3.6). The heavily p-type doped hydrogenated amorphous silicon approximately 50nm thick has been grown at NREL facilities and used to fabricate a-Si:H/a-BC:H devices by the process described in section 2.3.6 at the substrate temperature of 250ºC. The V-I characteristics of the a-Si:H/a-BC:H structure with no pre-deposition processing of the a-Si:H are shown in Figure 97.

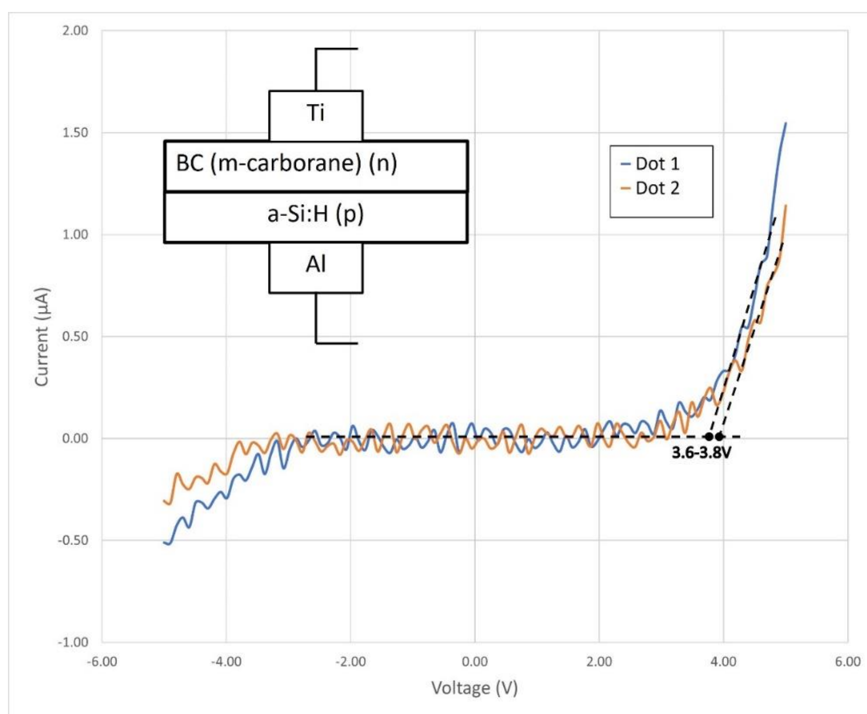

Figure 97 V-I characteristic of a-Si:H(p)/a-BC:H(n) device

As the a-BC:H layer deposited is approximately 100nm thick, predicting from the c-Si devices in the previous section, the current output is expected to be higher than the 1.5μA at 5V that is produced. Since the only change in the device structures is the substitution of c-Si with a-Si:H, and there is a significant difference in the current output at comparable voltages, the interface formation at the junction of a-BC:H and a-Si:H is studied further.

As it was stated for the device in Figure 97 there was no pre-deposition surface processing of a-Si:H. The V-I characteristics of the device with 170nm a-BC:H deposited on HF acid processed of a-Si:H, is shown in Figure 98 from two separate metal contacts. The direct comparison of V-I curves between the two devices is shown in Figure 99.

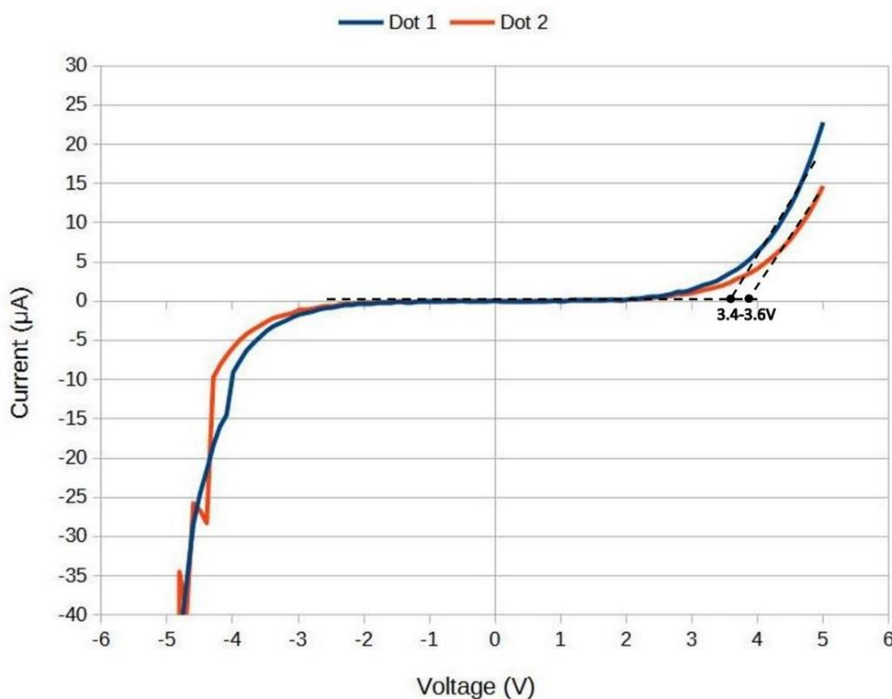

Figure 98 V-I characteristic of a-Si:H(p)/a-BC:H(n) device with HF pre-deposition process

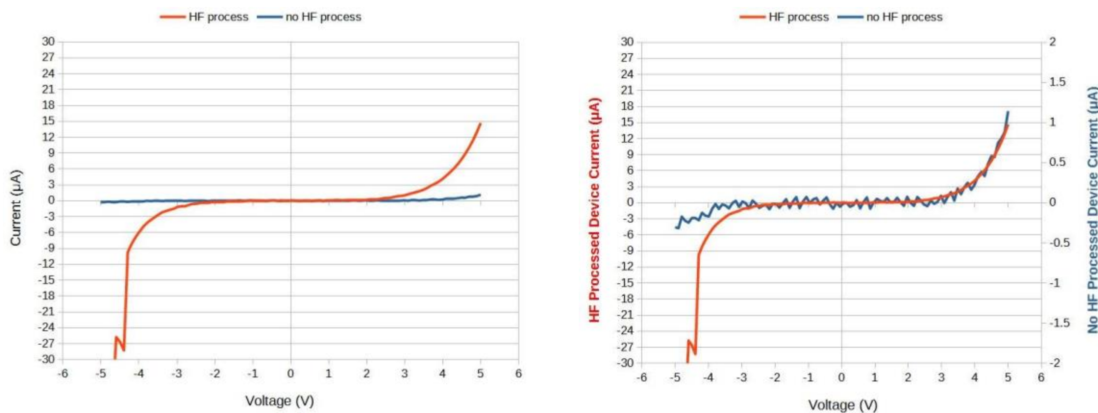

Figure 99 V-I characteristics of a-Si:H/a-BC:H devices with HF processed a-Si:H layer and unprocessed a-Si:H layer on the same scale (left) and unprocessed device on a secondary vertical axis (right)

The V-I curves exhibit similar behavior with the comparable turn-on voltage of 3.4-3.8V between two devices which can be seen in Figures 97, 98, 99 (right) with a secondary vertical axis introduced for the unprocessed pre-deposition device structure. However, the pre-deposition processed device exhibits a significantly higher current output of 15µA compared to 1.14µA at 5V which can be seen in Figure 99 (left) where both V-I curves are on the same scale. This indicates the improvement in the junction formation at the interface between a-Si:H and a-BC:H as a-BC:H was grown by the same process for both devices. In the reverse bias region, the breakdown voltage occurs at approximately 5V for the HF processed device. This breakdown could occur as the HF processing reduced thickness of a-Si:H film to approximately 35nm from the approximately 55nm of the unprocessed a-Si:H film determined by the ellipsometric optical model of the a-BC:H/a-Si:H structure.

The HF process of the a-Si:H layer before device fabrication increased the current output of the device compared to the unprocessed a-Si:H/a-BC:H device. However,

compared to the c-Si/a-BC:H device the current output is still smaller. The comparison between the c-Si/a-BC:H and the a-Si:H/a-BC:H device is shown in Figure 100, where the left vertical axis scales the a-Si:H/a-BC:H device and the right vertical axis the c-Si/a-BC:H device.

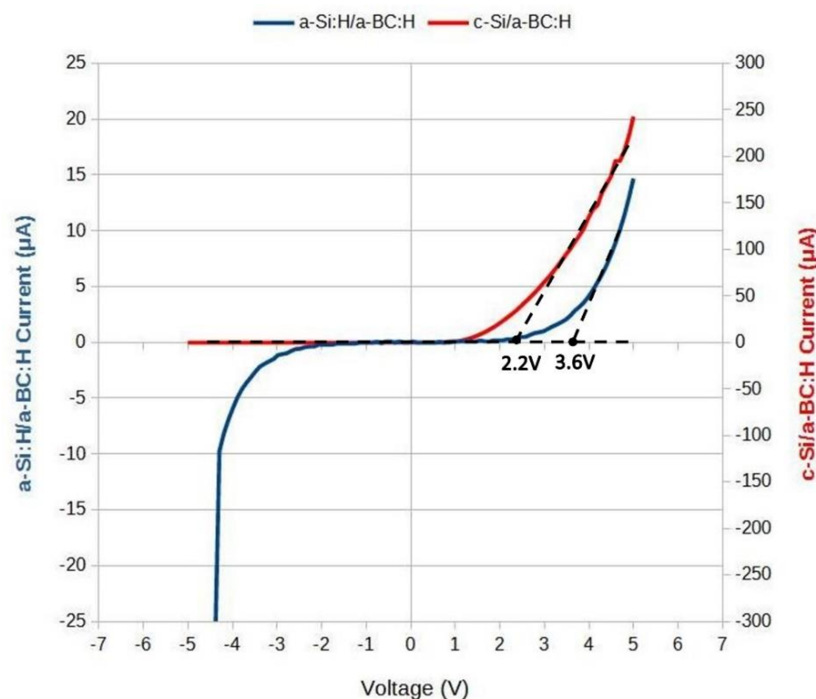

Figure 100 V-I characterstics of a-Si;H(p)/a-BC:H(n) (left vertical axis) and c-Si(p)/a-BC:H(n) (right vertical axis) devices

It can be noted that the turn-on voltage is lower for the c-Si/a-BC:H device by ~1.4V, increasing the current output by ~16 times more than the a-Si:H/a-BC:H device at 5V. However, as previously discussed, the turn-on voltage is a contributing factor but not the sole factor in the current output differences. Additionally, the c-Si/a-BC:H does not exhibit breakdown in this voltage range, while HF processed a-Si:H/a-BC:H does. This could be attributed to the thickness of the highly p-type a-Si:H layer of 50nm, compared to the 300µm thick c-Si layer. The thin a-Si:H fully depletes in the reverse bias region,

causing the electric field to be applied across the entire a-Si:H layer. As the electric field sweeps carriers across the depleted layer at a certain voltage bias, breakdown occurs.

Noticeable differences between unprocessed a-Si:H/a-BC:H, HF processed a-Si:H/a-BC:H and c-Si:H/a-BC:H could be attributed to the formation of the junction at the interface between two layers. The XPS oxygen spectra is observed for both HF processes and unprocessed a-Si:H layer in the a-Si:H/a-BC:H devices and shown in Figure 101.

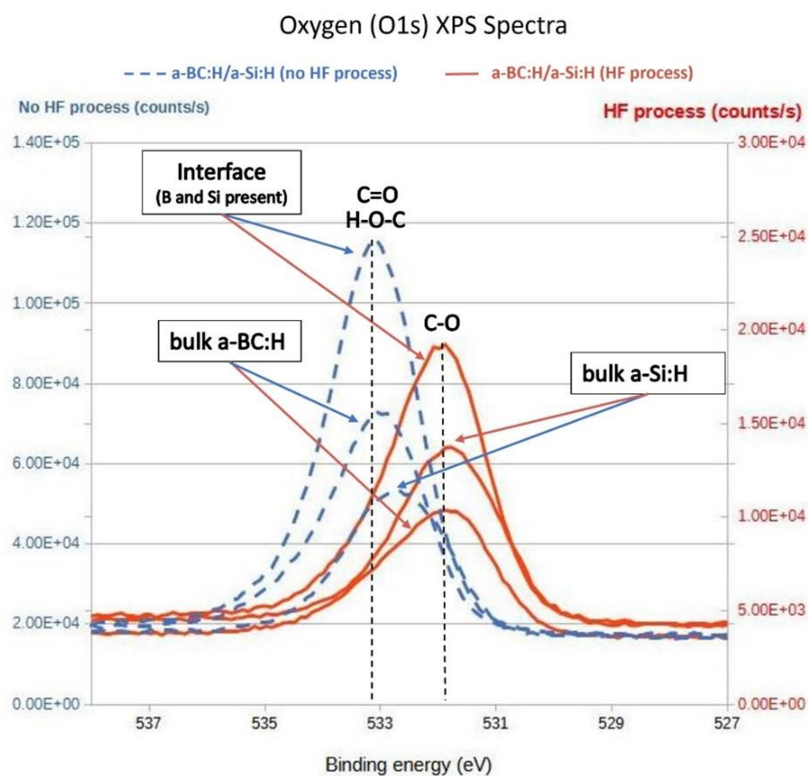

Figure 101 XPS oxygen spectra comparison of the a-BC:H/a-Si:H device with no HF (left vertical axis) and HF acid pre-deposition processing of a-Si:H (right vertical axis)

The XPS oxygen spectra in Figure 101 is collected at approximately the same depth within each device structure to produce comparable results. The bulk oxygen spectra are collected in the layer of the structure where either only boron or only silicon is present. The interface spectra are collected in the layer of the structure where both boron

and silicon peaks are present. The unprocessed surface of a-Si:H is contaminated by carbon and oxygen, which could additionally produce contamination throughout the a-BC:H film. As plasma-induced reactions occur at the surface of the contaminated a-Si:H, additional bonding of H, C, O can occur resulting in noticeable peak shifts and intensities seen in Figure 101.

The oxygen spectra of the HF pre-deposition-processed structure is scaled on the secondary axis (right axis) as shown by the color labeling, for simpler visualization as the oxygen content of the HF processed structure is at least a factor of 5 lower than in the device without any processing. This at least partially explains the V-I characteristic behavior between two devices shown in Figure 99 and previously discussed.

However, both c-Si and a-BC:H were HF processed pre-device fabrication, and still exhibit different V-I characteristic behavior (Figure 100). The difference in the V-I characteristic could be attributed to the formation of the heterojunction interface as a-Si:H and c-Si have certain different electronic properties and structural differences (amorphous and crystalline).

The valence band offset between a-BC:H and a-Si:H is obtained by collecting XPS core level data in the bulk and at the interface of the device structure, as discussed in detail in the previous section. The bulk CL peak and the VBM of a-BC:H in the bulk was collected at the depth profile of the layer where only the B peak is present, and the CL peak and VBM of a-Si:H in the bulk was collected at the layer where only the Si peak is present. Interface CL peaks were collected at the depth profile where both boron and silicon peaks were present. The XPS core level peaks in the bulk and in the interface, and the valence band maxima of a-BC:H and a-Si:H are shown in Figures 102-105

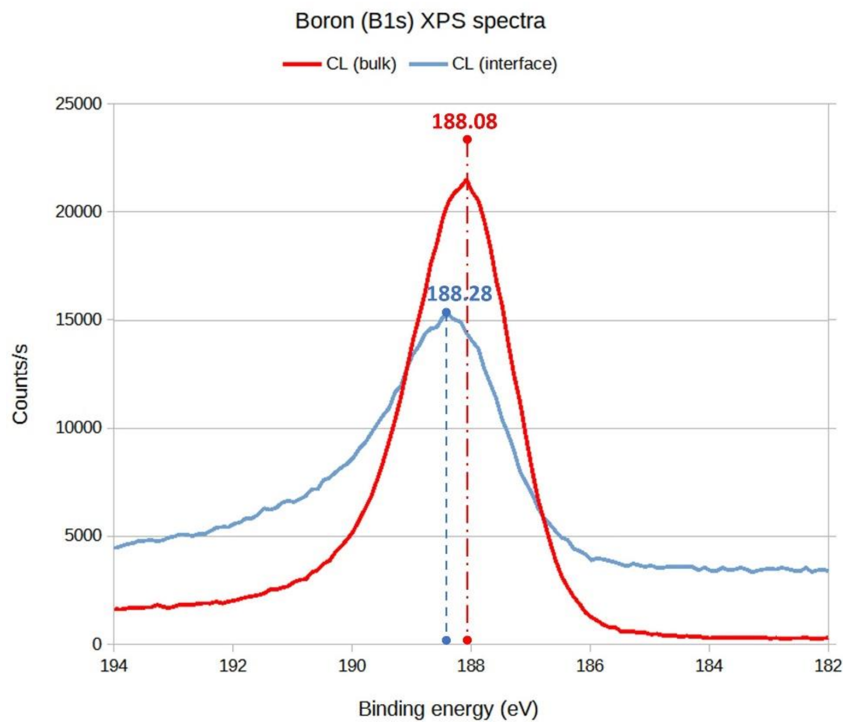

Figure 102 XPS spectra of B (a-BC:H) in the bulk and at the interface with a-Si:H

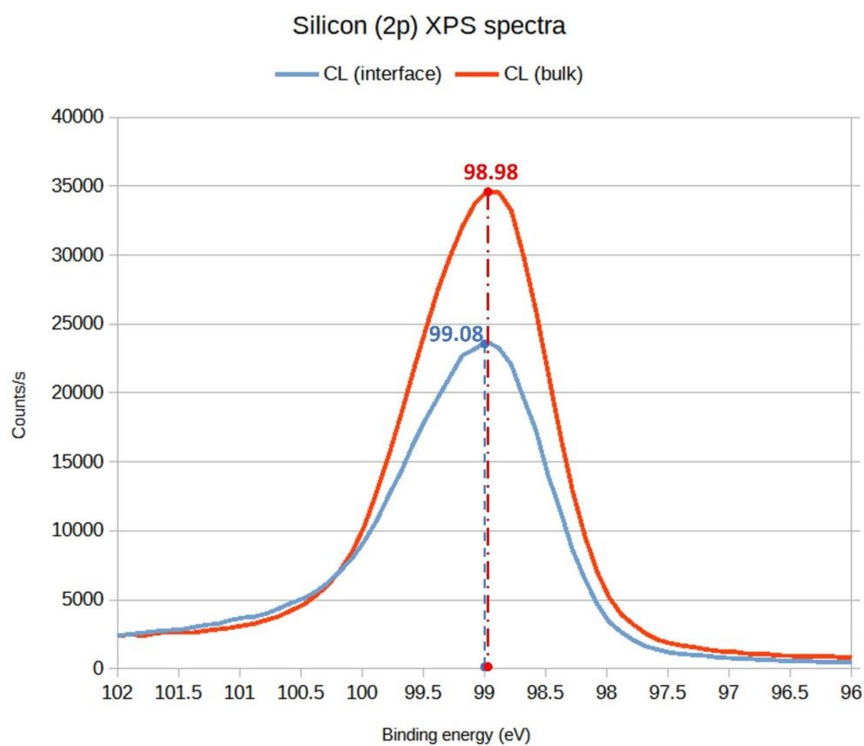

Figure 103 XPS spectra of Si (a-Si:H) in the bulk and at the interface with a-BC:H

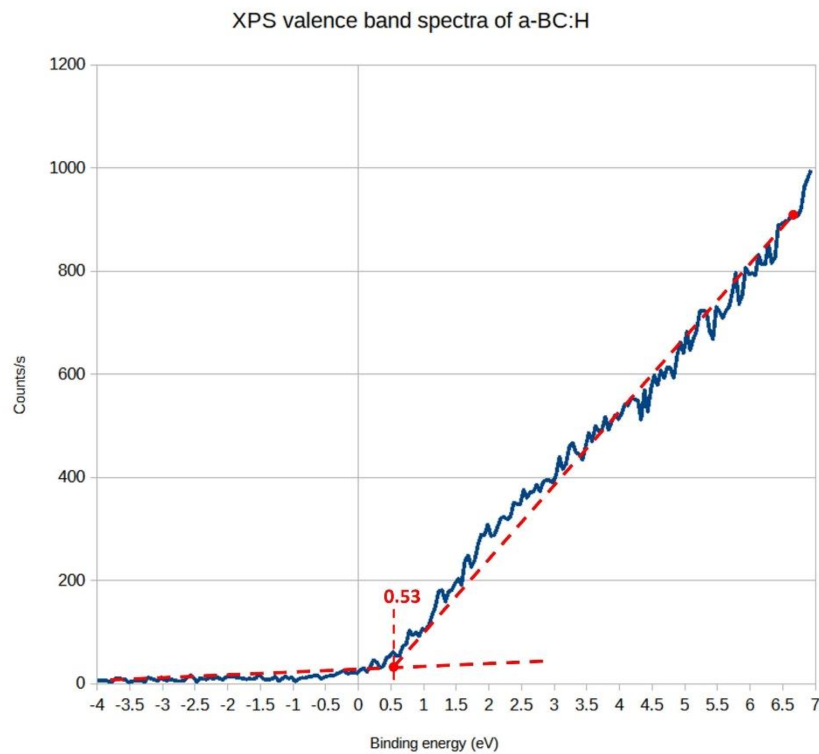

Figure 104 Valence band maximum of a-BC:H from XPS spectra from the bulk

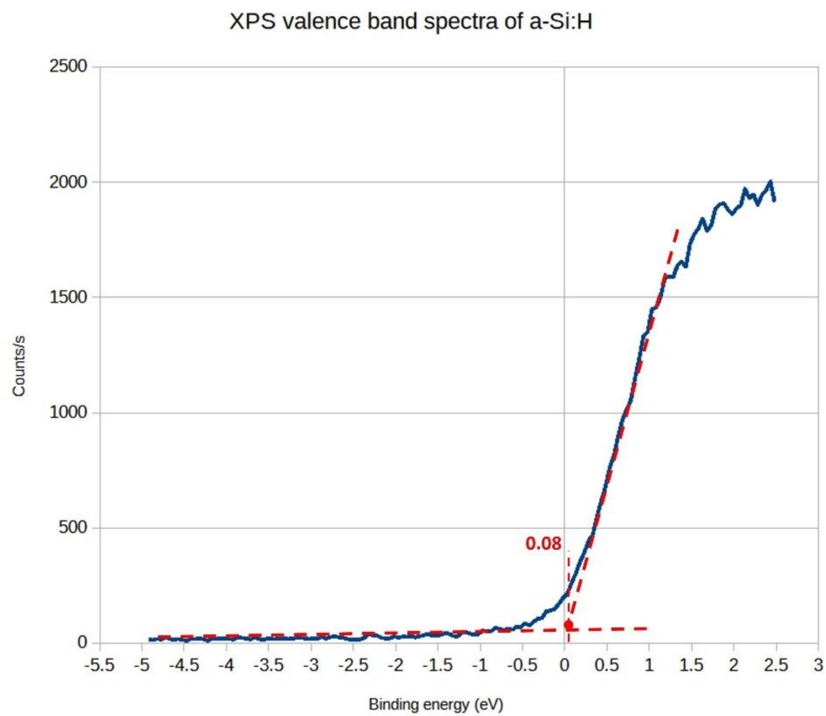

Figure 105 Valence band maximum of a-Si:H from XPS spectra from the bulk

Equation 20 was used to calculate VBO of the a-BC:H/a-Si:H structure from the data points shown in Table 13. The VBO calculations are shown in Equation 25.

Table 13 Core level peaks and valence band maxima for a-BC:H and a-Si:H

Layer	CL (eV)	CL_{int} (eV)	VBM (eV)
a-BC:H (n-type)	188.08±0.1	188.28±0.1	0.53±0.05
c-Si (p-type)	98.98±0.1	99.08±0.1	0.08±0.05

Equation 25: $VBO = \Delta E_v = 98.9 - 187.35 + 89.2 = 0.55eV$

The valence band maxima and conduction band minima of a-BC:H and a-Si:H at the interface are calculated by Equation 22 and 23 (discussed in the previous section). The band diagram at the interface is illustrated and shown in Figure 106, including the valence and conduction band offsets and the bandgap of a-BC:H (1.2eV) and a-Si:H (3.92eV).

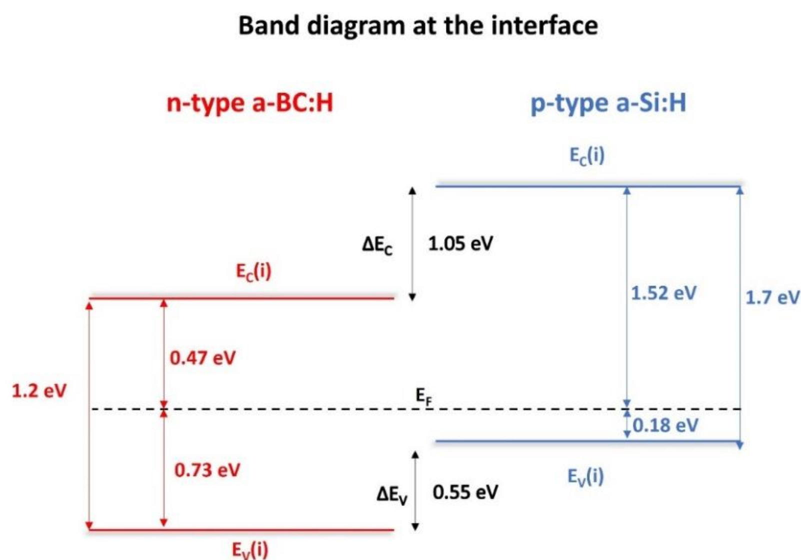

Figure 106 The a-BC:H(n)/a-Si:H(p) heterojunction band diagram at the interface

As valence band maxima of a-Si:H and a-BC:H obtained from the XPS measurements are at the positions of the valence band maxima with respect to the Fermi

level in the a-BC:H and a-Si:H bulk, the band diagram of the entire heterojunction can be illustrated as shown in Figure 107.

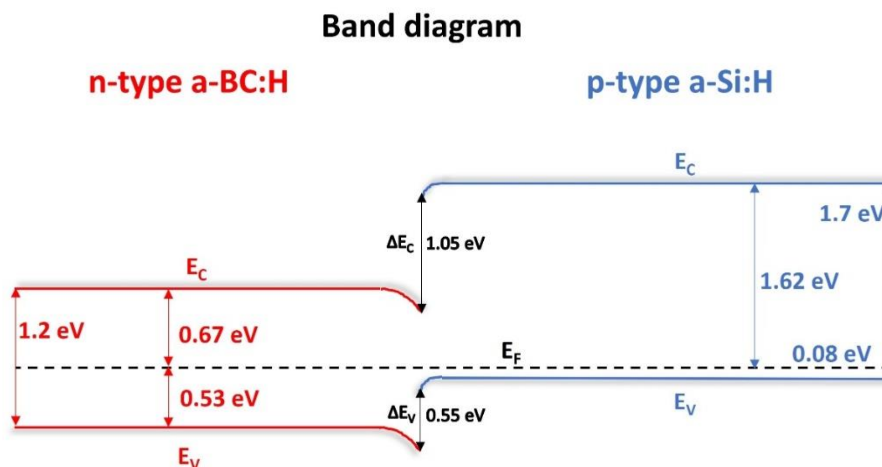

Figure 107 The a-BC:H(n)/a-Si:H(p) heterojunction band diagram

As the Fermi levels need to align there is band bending at the interface, as discussed in the previous section. The Fermi level position with respect to the valence band of a-Si:H in the bulk can be calculated using Equation 26, where the doping of the p^+-type a-Si:H is approximately $1x10^{19}cm^{-3}$ and p-type density of states $2x10^{20}cm^{-3}$.

Equation 26: $E_F - E_V = kT \cdot ln\left(\frac{N_V}{p}\right) = 0.026eV \cdot ln\left(\frac{2\cdot10^{20}}{1\cdot10^{19}}\right) = 0.078eV$

N_V – p-type density of states of single crystal silicon (N_V)
p – hole concentration of the used p-type c-Si wafer

The calculated Fermi level position is close to the valence band as expected for a heavily doped semiconductor. The valence band maximum binding energy with respect to the Fermi level in the bulk of a-Si:H obtained by the XPS measurements is shown to be approximately 0.08eV (Figure 105). Both calculated and experimentally obtained values are comparable, confirming the approach of the Kraut's method using the XPS measurements to investigate the band structure at the interface.

4.3 Discussion of the a-BC:H/a-Si:H (c-Si) band diagrams

The objective of forming the band structures of the a-BC:H/a-BC:H and a-BC:H/c-Si interface is to attempt to understand the V-I characteristic differences between the two devices investigated in this chapter. As discussed, Kraut's method utilizes XPS binding energy measurements with respect to the Fermi level [8]. Because the Fermi levels at the interface need to align between two semiconductors, the band diagrams obtained from the Kraut's method relate to the interface of the two semiconductors forming a heterojunction. The bulk properties of the semiconductors forming the heterojunction cannot be obtained from the Kraut's method because bulk material properties do not necessarily dictate the behavior of the materials at the interface [14]. However, from the bulk valence band maxima obtained via XPS measurements, the complete band diagram of the heterojunction can be illustrated with respect to the Fermi level as shown in Figure 96 and 107.

The band diagrams of the a-BC:H/a-Si:H and the a-BC:H/c-Si have been previously discussed but are shown in Figure 108 side by side for reference.

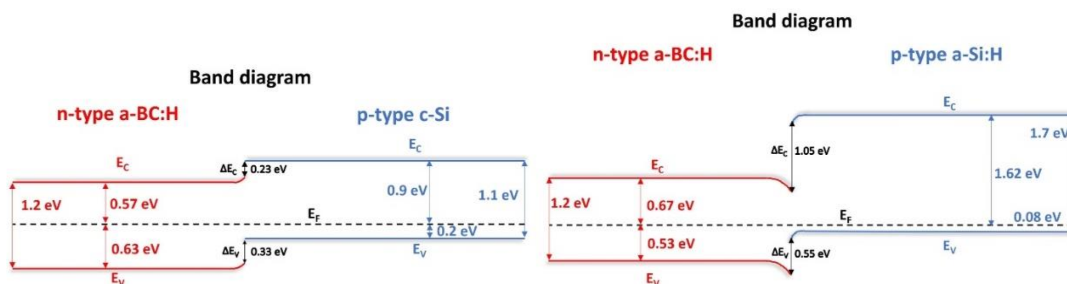

Figure 108 Band diagrams of a-BC:H/c-Si (left) and a-BC:H/a-Si:H (right) heterojunctions

From Figure 108 it can be noted that the a-BC:H/a-Si:H heterojunction has larger valence and conduction band offsets than the a-BC:H/c-Si heterojunction. There are also differences in the position of the valence and conduction bands with respect to the Fermi

level for the two cases. Additionally, it can be noted that the heterojunction formed at the interface of a-BC:H with c-Si and a-Si:H produces different band bending between the two structures.

The a-Si:H and c-Si have comparable electron affinities of 3.92eV and 4eV respectively. The electron affinity is the energy an electron needs to completely leave the conduction band and reach vacuum just outside the semiconductor. The electron affinity rule for band alignment states that the heterojunction band alignment is dictated by the electron affinities of different semiconductors, so the electron affinity rule states that the conduction band offset is equal to the difference in the electron affinities of two semiconductors (Equation 27) [14].

Equation 27: $\Delta E_c = q\chi_{Si} - q\chi_{BC}$

If the electron affinity rule is followed, the electron affinity of a-BC:H is calculated using Equation 27 to be 4.23eV by knowing the conduction band offset (0.23eV) at the a-BC:H/c-Si interface shown in Figure 108 (right) and the electron affinity of c-Si (4eV). However, if the electron affinity rule is applied to the a-BC:H/a-Si:H interface, knowing the electron affinity of a-Si:H (3.92eV) and conduction band offset (1.05eV) at the interface shown in Figure 108 (left), the electron affinity of a-BC:H is calculated to be 4.97eV. There is a difference of 0.74eV between the two electron affinities calculated for the a-BC:H layer between two devices.

There are two apparent differences between the two devices that could contribute to the differing formation of the heterojunction interfaces:

1. Deposition temperature of a-BC:H grown on a-Si:H (250ºC) and on c-Si (350ºC)
2. The amorphous structure of a-Si:H compared to the crystalline structure of c-Si.

Through internal communication with the National Renewable Energy Laboratory where the a-Si:H films were grown, it was stated that the temperature of a-Si:H should not exceed the deposition temperature of 250ºC due to surface crystallization that occurs at higher temperatures. The a-BC:H/c-Si devices were grown with the established procedure in the literature where optimal deposition of a-BC:H was achieved at 350ºC. Optical characterization via spectroscopic ellipsometry did not yield any differences in the optical constants between a-BC:H deposited at different temperatures. Observing the XPS measurements of boron in Table 12 and 13, there are 0.2eV and 0.1eV differences between core level and interface core level binding energies of a-BC:H deposited at 350ºC and 250ºC. However, as the XPS measurements have been collected at the 0.1eV step resolution, and the calculated electron affinities of a-BC:H from two band diagrams are different by 0.74eV, the subtle difference in the core level binding energies should not produce a large electron affinity difference within the same material.

The more fundamental explanation of the electron affinity difference within a-BC:H between the a-BC:H/a-Si:H and a-BC:H/c-Si device structures is the fact that electron affinity rule does not always work. The electron affinities reflect potential shifts arising from the surface electronic structure, and not the shifts that are due to the charge distribution at the actual interface [14]. Meaning that the electron affinity rule attempts to define the behavior at the interface by using bulk semiconductor properties. This is why the band offsets are generally experimentally determined [14], and why Kraut's method in literature has not been utilized to obtain electron affinities of the various semiconductors forming heterojunctions [9-13].

Additionally, the built-in potential is defined as the potential difference across the junction defined by the difference in the Fermi level in the bulk of two semiconductors forming a junction. As previously discussed, the Fermi levels need to be aligned when the junction is formed, resulting in bending of the conduction and valence bands. Therefore, the built-in potential is the amount bands need to bend to align the Fermi levels. To calculate the position of the Fermi level from the material properties, it is necessary to know the doping concentration and the density of states of the valence or conduction band. As those quantities are unknown for n-type a-BC:H, the position of the Fermi level in the bulk is also unknown. Because the bulk Fermi level position is unknown for a-BC:H the built-in potential cannot be calculated.

Even though the electron affinity of a-BC:H and the built-in potential at the heterojunction cannot be calculated, the difference in the band offsets between a-BC:H/a-Si:H and a-BC:H/c-Si could be attributed to the formation of the interface with two structurally different films, amorphous and crystalline silicon films. As the band offsets are not dictated by the electron affinities that are comparable between the two (3.92eV and 4eV), the mechanism that cause different interface formation at the junction with a-BC:H are unknown. However, the energy differences between band offsets are enough to cause differing device performance noticeable on the respective V-I curves of a-BC:H/a-Si:H and a-BC:H/c-Si devices.

4.4 Summary

In this chapter, the results of the investigation of a-BC:H devices have been shown through fabrication and characterization of c-Si/a-BC:H and a-Si:H/a-BC:H heterojunction devices. As single crystal silicon degrades over time due to radiation damage, the a-Si:H is used as a p-type layer substitute to introduce a novel neutron detection heterojunction device fabricated with n-type a-BC:H grown from meta-carborane.

There are noticeable differences in V-I characteristics between devices that utilize c-Si and a-Si:H, as well as devices that utilize surface processed a-Si:H and the ones that do not. As c-Si/a-BC:H devices exhibit higher current output and lower turn-on voltage than the a-Si:H/a-BC:H, the interface of a-Si:H/a-BC:H devices was examined by XPS to attempt to understand the reduction of current flow through the a-Si:H/a-BC:H devices. It was concluded that the HF acid pre-deposition processing improves the interface by reducing the oxygen content and the surface contaminants of a-Si:H that seem to contribute to more pronounced H-O-C and C=O bonding in the bulk of a-BC:H and at the interface. However, HF acid processing of a-Si:H does not improve the current output to the comparable values of the c-Si/a-BC:H devices. The differences in the V-I characteristics can be partially attributed to the differences in the band structures. The XPS measurements are used to construct the heterojunction band diagram of both devices by calculating the valence band offsets of c-Si/a-BC:H and a-Si:H/a-BC:H structures from the core level XPS peaks and valence band spectra using Kraut's method.

The heterojunction formed between a-BC:H/c-Si and a-BC:H/a-Si:H are type II heterojunctions, with larger band offsets at the interface of a-BC:H/a-Si:H. As the Fermi

level in the bulk of a-BC:H is unknown the built-in voltage of the two devices cannot be calculated. However, the noticeable differences in the band offsets could be a contributing factor to the V-I characteristic differences between devices. Additionally, as there are fundamental structural differences between single crystal and amorphous silicon, the full effects of the interfaces formed with a-BC:H are not completely understood. However, the differences between the two devices are partially defined throughout the chapter by V-I characteristics and XPS measurements, providing clear indication that a novel a-Si:H/a-BC:H heterojunction device with potential for neutron detection was developed.

.

4.5 References

[1] Ali O. Sezer, J.I. Brand, Chemical vapor deposition of boron carbide, Materials Science and Engineering: B, Volume 79, Issue 3, 2001, Pages 191-202, ISSN 0921-5107, https://doi.org/10.1016/S0921-5107(00)00538-9

[2] Mirzokarimov, Mirzojamshed. Boron carbide hetero-isomeric device fabrication by PECVD from isomeric precursor ortho-carborane and meta-carborane. MS Thesis. University of Nebraska, 2019

[3] Seong-Don Hwang, Dongjin Byun, N. J. Ianno, P. A. Dowben, H. R. Kim; Fabrication of boron-carbide/boron heterojunction devices. Appl. Phys. Lett. 11 March 1996; 68 (11): 1495–1497. https://doi.org/10.1063/1.116266

[4] Hong, Nina, "An Exploration of Neutron Detection in Semiconducting Boron Carbide" (2012). *ETD collection for University of Nebraska - Lincoln*. AAI3503993. https://digitalcommons.unl.edu/dissertations/AAI3503993

[5] Peterson, George Glen, Electrical Characterization of Irradiated Semiconducting Amorphous Hydrogenated Boron Carbide, (2017). Mechanical (and Materials) Engineering -- Dissertations, Theses, and Student Research. 124. http://digitalcommons.unl.edu/mechengdiss/124

[6] Caruso, A. & Billa, Ravi & Balaz, Snjezana & Brand, J. I. & Dowben, Peter, The heteroisomeric diode. Journal of Physics Condensed Matter. 16. L139-L146. (2004), https://doi.org/10.1088/0953-8984/16/10/L04

[7] David Emin and T. L. Aselage, A proposed boron-carbide-based solid-state neutron detector, J. Appl. Phys. 97, 013529 (2005); https://doi.org/10.1063/1.1823579

[8] E. A. Kraut, R. W. Grant, J. R. Waldrop, and S. P. Kowalczyk, Precise Determination of the Valence-Band Edge in X-Ray Photoemission Spectra, Application to Measurement of Semiconductor Interface Potentials, Phys. Rev. Lett. 44, 1620, 1980, https://doi.org/10.1103/PhysRevLett.44.1620

[9] K.C. Sanal, Rafael Ballinas Morales, Victoria E. Gonzàlez Flores, S. Shaji, P.K. Nair, M.T.S. Nair, Co-sputtered Zn1-xMgxO films and interfacial band offsets at heterojunctions with SnS-CUB, Journal of Alloys and Compounds, Volume 763, 2018, Pages 909-915, ISSN 0925-8388, https://doi.org/10.1016/j.jallcom.2018.05.276.

[10] Kumar, M., Rajpalke, M.K., Roul, B., Bhat, T.N., Kalghatgi, A.T. and Krupanidhi, S.B. (2012), Determination of MBE grown wurtzite GaN/Ge_3N_4/Ge heterojunctions band offset by X-ray photoelectron spectroscopy. Phys. Status Solidi B, 249: 58-61. https://doi.org/10.1002/pssb.201147318

[11] Sean W. King, Marc French, Guanghai Xu, Benjamin French, Milt Jaehnig, Jeff Bielefeld, Justin Brockman, Markus Kuhn, Valence band offset and Schottky barrier at amorphous boron and boron carbide interfaces with silicon and copper, Applied Surface Science, Volume 285, Part B, 2013, Pages 545-551, ISSN 0169-4332, https://doi.org/10.1016/j.apsusc.2013.08.090

[12] Nina Hong, M. A. Langell, Jing Liu, Orhan Kizilkaya, S. Adenwalla; Ni doping of semiconducting boron carbide. J. Appl. Phys. 15 January 2010; 107 (2): 024513, https://doi.org/10.1063/1.3284205

[13] Seong-Don Hwang, N. B. Remmes, P. A. Dowben, D. N. McIlroy; Nickel doping of boron carbide grown by plasma enhanced chemical vapor deposition. Journal of Vacuum Science & Technology B: Microelectronics and Nanometer Structures Processing, Measurement, and Phenomena 1 July 1996; 14 (4): 2957–2960. https://doi.org/10.1116/1.588942

[14] E.T. Yu, J.O. McCaldin, T.C. McGill, Band Offsets in Semiconductor Heterojunctions, Editor(s): Henry Ehrenreich, David Turnbull, Solid State Physics, vol. 46, 1992, p. 1-146, ISBN 9780126077469, https://doi.org/10.1016/S0081-1947(08)60397-5

Chapter 5 – Summary and Conclusion

The main objective of this dissertation was to present a novel device fabricated from n-type hydrogenated amorphous boron carbide and p-type hydrogenated amorphous silicon. Through device V-I characterization, ellipsometry and XPS measurements it was shown that a-Si:H has potential to be used as a device layer in a low-cost, durable, and efficient neutron detector device.

The potential for a quality neutron detector is based on the neutron absorption efficiency of boron carbide as a compound of boron, specifically from its naturally abundant B^{10} isotope that has a large absorption cross-section (3840 barns) at low energies (0.025eV). With the combination of attractive material properties such as abrasion resistance, high melting point, chemical inertness, and radiation resistance in part due to its icosahedra molecular structure, boron carbide has been widely researched for next generation solid-state neutron detectors. There have been all-BC devices fabricated from polymeric precursors closo-1,2-dicarbadodecaborane (ortho-carborane, $C_2B_{10}H_{12}$) and closo-1,7-dicarbadodecaborane (meta-carborane, $C_2B_{10}H_{10}$) via plasma enhanced chemical vapor deposition. These devices have demonstrated the detection of thermal neutrons, and a neutron voltaic effect but have shown limitations.

Devices fabricated from a-BC:H and single crystal silicon have shown improved device performance: lower turn-on voltage, higher current output, and no breakdown at high voltages. However, as single crystal silicon degrades under radiation over time, hydrogenated amorphous silicon was presented as a substitute for neutron detector device fabrication, as its amorphous structure and presence of hydrogen reduces degradation due to radiation damage.

Developing an a-Si:H/a-BC:H device was initially defined by optimization of a-BC:H film deposition process. The a-BC:H film growth via plasma enhanced chemical vapor deposition is a complex process dependent on various deposition parameters, it was shown how those parameters affect film growth and how a-BC:H deposition was optimized to produce as identical as possible thin-film device layers.

The next objective was to understand metal contacts as integral parts of device fabrication, as the type of contact formation and the effect of metal contact resistance on n-type a-BC:H has not been previously investigated. When the metal contact effects are not defined, understanding of the device behavior is unclear as different contacts can affect device current flow by either forming an Ohmic or a Schottky contact with a device layer. It was shown how various metals interact with both p-type and n-type a-BC:H, identifying titanium as forming an Ohmic contact with n-type a-BC:H. Using the spreading resistance model, it was shown how contact resistance and resistivity of a-BC:H can be measured in the direction of the device current flow. It was important to note that various investigated metals form a Schottky contact with p-type a-BC:H. The current flow through the Schottky contact was shown to produce orders of magnitude lower currents through the metal/a-BC:H structure than the Ohmic contact, introducing another limitation of utilizing p-type a-BC:H in the device fabrication process.

The 4-Wire V-I measurements of a-Si:H/a-BC:H and c-Si/a-BC:H devices showed differences in the device behavior: different turn-on voltages, breakdown, and current flow. Additional characterization of device interfaces via XPS indicated a noticeable difference of device performance dependent on pre-deposition surface processing of a-Si:H. The oxygen reduction at the interface by HF acid processing improved current flow

of the a-Si:H/a-BC:H but has not improved device performance to the level of c-Si/a-BC:H devices. A contributing factor to dissimilar V-I characteristics was defined from the differences in the band structure alignment by measuring the valence and conduction band offsets of the device layers via XPS using Kraut's method. Even though the Fermi level of a-BC:H is unknown so the exact built-in voltage of the devices cannot be calculated it was quantitatively shown the c-Si/a-BC:H device has lower discontinuities in the band structure that can contribute to the device performance. Additionally, as a-BC:H is deposited on single crystal and amorphous silicon, coupled with surface chemistry and band alignment, it can be concluded that the interface formation at the heterojunction structure significantly affects the a-Si:H/a-BC:H device performance.

This dissertation successfully presented the development and characterization of a novel heterojunction a-BC:H(n)/a-Si:H(p) with neutron detector/voltaic potential. This was done by identifying titanium as an ohmic metal contact with n-type a-BC:H, determining the band structure at the interface and successfully demonstrating device operation under voltage compared to the already established a-BC:H/c-Si device.

The potential for future research of the novel a-BC:H/a-Si:H devices is rooted in the ability to dope both a-BC:H grown from meta-carborane and a-Si:H device layers. The spreading resistance measurement technique performed as a function of film thickness allows for calculation of the film resistivity and contact resistance. With this method there is potential to quantify how doping affects a-BC:H independently, while also showing how it affects device performance. Finally, with the ability to dope both a-Si:H and a-BC:H from meta-carborane, there is potential in creating an a-Si-BC-BC p-i-n junction neutron detector device.